TECHNISCHE
UNIVERSITÄT
DRESDEN

**Faculty of Mechanical Science and Engineering** Institute for Materials Science
Chair of Materials Science and Nanotechnology

# On-surface synthesis of acenes – organic nanoelectronic materials explored at a single-molecule level

M.Sc. Justus Krüger
Born on: 31st July 1988 in Dresden

## Dissertation

accepted by the Faculty of Mechanical Science and Engineering

at the Technische Universität Dresden

to achieve the academic degree

## Doktoringenieur (Dr.-Ing.)

First referee
**Prof. Dr. Gianaurelio Cuniberti**
Second referee
**Prof. Dr. Lukas Eng**

Submitted on: 4th July 2017
Defended on: 5th December 2017

# Abstract

Acenes are a class of polycyclic aromatic hydrocarbons (PAH) with linearly fused benzene rings. They are widely considered as promising materials for organic and molecular electronics. However, larger molecules of this class possessing more than five rings are chemically extremely reactive and show a very low solubility. Hence, large acenes are difficult to handle, and the experimental data available to date is limited. The aim of this work is to show a very promising protocol of how acenes with different lengths can be stabilized and investigated on metallic surfaces. The experimental approach of on-surface synthesis is explored to generate the respective acenes directly on the metallic substrate via the reduction of suitable precursor molecules. High-resolution scanning probe microscopy (SPM) is employed at a temperature of 5 K to verify the chemical conversion at a single-molecule level.

In the first part of this work, the on-surface synthesis of acenes is introduced via the example of tetracene (4-acene) formation on Cu(111). Precursors with 1,4-epoxy moieties preferably adsorb with their oxygen-rich site facing the substrate. Subsequently, they can be deoxygenated via annealing of the substrate or by single-molecule manipulation with the tip of the scanning probe microscope. In both cases, atomic force microscopy (AFM) measurements resolve the planar adsorption geometry of tetracene on the surface with atomic resolution. Based on these findings, scanning tunneling microscopy (STM) is employed to investigate the self-assembly patterns of on-surface generated anthracene (3-acene) and tetracene molecules after synthesis on Au(111). These measurements show intriguing organic nanostructures and supramolecular networks that can form at the metallic interface upon thermally-induced surface reactions.

The second part of this thesis focuses on the electronic structure of acenes adsorbed on a metallic substrate. By applying the novel method of on-surface reduction, single and isolated hexacene (6-acene) molecules are investigated on Au(111). Scanning tunneling spectroscopy (STS) measurements indicate a weak interaction with the substrate and reveal five accessible molecular resonances at the organic-metal interface. The differential conductance maps with high spatial resolution at the respective resonant bias values compare well to elastic scattering quantum chemistry-based calculations. Finally, the experimental investigations of Br-substituted precursors show the stabilization of genuine unsubstituted heptacene (7-acene), as confirmed by imaging of the molecular structure via atomic-resolution STM. Accordingly, the precise characterization of this molecule via STS allows more insight into the electronic structure of adsorbed acenes with respect to their length.

# Zusammenfassung

Acene sind eine Klasse von polyzyklischen aromatischen Kohlenwasserstoffen mit linear kondensierten Benzolringen. Sie gelten weithin als vielversprechende Materialien für die organische und molekulare Elektronik. Jedoch sind die größeren Moleküle dieser Klasse mit mehr als fünf Ringen chemisch extrem reaktiv und zeigen eine sehr geringe Löslichkeit, daher gibt es bisher nur wenige experimentelle Untersuchungen ihrer Eigenschaften. Das Ziel dieser Arbeit ist es, Acene mit unterschiedlichen Längen auf einer metallischen Oberfläche stabilisieren und untersuchen zu können. Dabei wird der experimentelle Ansatz der Oberflächensynthese verfolgt und die jeweiligen Acene durch Reduktion von geeigneten Präkursoren direkt an einer metallischen Grenzfläche hergestellt. Hochauflösende Rastersondenmikroskopie an einzelnen Molekülen bei einer Temperatur von 5 K nimmt dabei eine Schlüsselrolle im Nachweis der chemischen Umwandlung auf der Oberfläche ein.

Im ersten Teil dieser Arbeit wird die Oberflächensynthese von Acenen am Beispiel von Tetracen (4-Acen) auf Cu(111) eingeführt. Die Ausgangsmoleküle mit funktionellen Gruppen adsorbieren bevorzugt mit ihrer sauerstoffreichen Seite auf dem Substrat und können dort sowohl thermisch als auch mithilfe der Spitze des Rastersondenmikroskops umgewandelt werden. In beiden Fällen wird die planare Adsorptionsgeometrie von Tetracen auf der Oberfläche mittels Rasterkraftmikroskopie mit atomarer Auflösung abgebildet. Darauf aufbauend wird Rastertunnelmikroskopie genutzt, um die Selbstassemblierung von Anthracen (3-Acen) und Tetracen nach der jeweiligen Synthese auf Au(111) zu untersuchen. Die Messungen zeigen unerwartete organische Nanostrukturen und supramolekulare Netzwerke, welche sich an der metallischen Grenzfläche durch die induzierte Oberflächenreduktion bilden können.

Der zweite Teil dieser Arbeit beschäftigt sich mit den elektronischen Eigenschaften von adsorbierten Acenen. Durch die neuartige Methode der Oberflächenreduktion können einzelne Hexacene (6-Acen) auf Au(111) untersucht werden. Messungen basierend auf Rastertunnelspektroskopie geben Hinweise auf die schwache Wechselwirkung mit dem Substrat und zeigen fünf molekulare Eigenzustände, die im Experiment zugänglich sind. Die entsprechenden Abbildungen der differentiellen Leitfähigkeiten mit hoher Ortsauflösung sind in guter Übereinstimmung mit einer quantenmechanischen Modellierung. Schließlich wird die Stabilisierung von Heptacen (7-Acen) von Br-substituierten Präkursoren mittels Rastertunnelmikroskopie mit atomarer Auflösung gezeigt. Dadurch kann die elektronische Struktur von adsorbierten Acenen anhand ihrer Länge verglichen werden.

# Table of contents

1 Introduction 1

2 Fundamentals of scanning probe microscopy 7
    2.1 Scanning tunneling microscopy . . . 7
        2.1.1 The working principle . . . 7
        2.1.2 Scanning tunneling spectroscopy . . . 11
        2.1.3 Single-molecule investigations . . . 13
    2.2 Atomic force microscopy . . . 18
    2.3 High-resolution imaging . . . 20

3 Experimental setup, materials, and methods 23
    3.1 Low-temperature scanning probe microscope . . . 23
    3.2 Sensors and tip preparation . . . 27
    3.3 Substrates . . . 29
        3.3.1 Au(111) . . . 29
        3.3.2 Cu(111) . . . 32
    3.4 Imaging . . . 32
    3.5 Molecular materials . . . 32
        3.5.1 Precursors . . . 32
        3.5.2 Perimeter free electron model . . . 34
    3.6 Modeling . . . 35
        3.6.1 Density functional theory . . . 35
        3.6.2 Elastic scattering quantum chemistry . . . 36

4 Tetracene formation on Cu(111) 39
    4.1 Imaging of the precursors . . . 40
    4.2 On-surface conversion . . . 42
        4.2.1 Single-molecule chemistry . . . 42
        4.2.2 Thermally induced reaction . . . 45
    4.3 Discussion . . . 47

5 Molecular self-assembly on Au(111) 49
5.1 Formation of anthracene trimers . . . 50
5.1.1 Self-assembly of precursors . . . 50
5.1.2 Chemical conversion . . . 51
5.2 Supramolecular networks of tetracene . . . 53
5.2.1 Self-assembly of the precursors . . . 53
5.2.2 Chemical conversion . . . 54
5.3 Discussion . . . 58

6 Electronic structure of hexacene stabilized on Au(111) 59
6.1 On-surface generation . . . 60
6.1.1 Thermally induced synthesis . . . 60
6.1.2 Self-assembly . . . 64
6.1.3 Higher annealing temperature . . . 64
6.2 Molecular orbital resonances . . . 65
6.3 Discussion . . . 69

7 Br-substituted precursors of heptacene on Au(111) 71
7.1 On-surface chemistry . . . 72
7.2 Heptacene stabilized on Au(111) . . . 75
7.2.1 Bias-dependent topography . . . 75
7.2.2 Differential conductance measurements . . . 77
7.3 Discussion . . . 79

8 Summary and outlook 81
8.1 On-surface synthesis . . . 81
8.2 Electronic properties . . . 82

A Appendix 87
A.1 Designed LabView program . . . 87
A.2 Additional AFM data of the tetracene precursors . . . 89
A.3 Control experiment with genuine tetracene . . . 89
A.3.1 As-prepared on Au(111) . . . 89
A.3.2 Annealing experiment . . . 90
A.4 Additional data for the electronic structure of adsorbed hexacene . . . 91
A.5 Additional STM data for Br-substituted precursors . . . 92
A.6 Additional STS data for adsorbed heptacene . . . 93

Bibliography 95

Scientific contributions 105

Acknowledgment 107

# List of abbreviations

| | |
|---|---|
| AFM | atomic force microscopy |
| An | anthracene |
| CDH | cyclodehydrogenation |
| DFT | density functional theory |
| DOS | density of states |
| EA | electron affinity |
| ESQC | elastic scattering quantum chemistry |
| fcc | face centered cubic |
| Hn | hexacene |
| Hp | heptacene |
| hcp | hexagonal closed packed |
| HOMO | highest occupied molecular orbital |
| HOMO-1 | second highest occupied molecular orbital |
| HOMO-2 | third highest occupied molecular orbital |
| IETS | inelastic tunneling spectroscopy |
| IP | ionization potential |
| LDOS | local density of states |
| LUMO | lowest unoccupied molecular orbital |
| LUMO+1 | second lowest unoccupied molecular orbital |
| LUMO+2 | third lowest unoccupied molecular orbital |
| MO | molecular orbital |
| ML | monolayer |
| PAH | polycyclic aromatic hydrocarbon |
| Pn | pentacene |

| | |
|---|---|
| SPM | scanning probe microscope |
| STM | scanning tunneling microscopy |
| STS | scanning tunneling spectroscopy |
| Tn | tetracene |
| UHV | ultrahigh vacuum |

# List of figures

1.1 Chemical structure of acenes . . . . . . . . . . . . . . . . . . . . . . . . 1
1.2 Energy levels and optical excitation of acenes . . . . . . . . . . . . . . . . 3
1.3 Resonant Clar structures of acenes . . . . . . . . . . . . . . . . . . . . . 4
1.4 Graphical outline of the experimental results . . . . . . . . . . . . . . . . 5

2.1 Basics of scanning tunneling microscopy . . . . . . . . . . . . . . . . . . 8
2.2 Tunneling geometry of the Tersoff-Hamann model . . . . . . . . . . . . . 11
2.3 Simple energy level diagram of a molecule . . . . . . . . . . . . . . . . . 14
2.4 Organic-metal interface as probed by STS . . . . . . . . . . . . . . . . . 16
2.5 Basics of atomic force microscopy . . . . . . . . . . . . . . . . . . . . . 18
2.6 Single-molecule imaging with AFM and STM . . . . . . . . . . . . . . . . 20

3.1 UHV system used for the experiments . . . . . . . . . . . . . . . . . . . 24
3.2 Picture of the disassembled SPM scanner unit . . . . . . . . . . . . . . . 25
3.3 Picture of the assembled SPM scanner unit . . . . . . . . . . . . . . . . 26
3.4 Employed STM and STM/AFM sensors . . . . . . . . . . . . . . . . . . 28
3.5 Crystal structure of the used samples . . . . . . . . . . . . . . . . . . . 30
3.6 Long- and short-range periodicity of the Au(111) surface . . . . . . . . . . 31
3.7 STM overview scan of the Cu(111) surface . . . . . . . . . . . . . . . . . 31
3.8 Molecular materials used in the experiments . . . . . . . . . . . . . . . . 33
3.9 Simple gas-phase model of the hexacene precursors Hn3O . . . . . . . . 34

4.1 Surface-assisted reduction . . . . . . . . . . . . . . . . . . . . . . . . . 40
4.2 STM overview image after molecule deposition . . . . . . . . . . . . . . . 40
4.3 Tetracene precursors on Cu(111) and NaCl(2ML) . . . . . . . . . . . . . . 42
4.4 Set of constant-current STM images on Cu(111) . . . . . . . . . . . . . . 43
4.5 Intermediate and final product of the STM tip-induced reaction . . . . . . 44
4.6 Product of the on-surface reduction on Cu(111) . . . . . . . . . . . . . . 46

5.1 Adsorption geometry of the investigated molecules on Au(111) . . . . . . 50
5.2 STM image of anthracene precursors on Au(111) . . . . . . . . . . . . . . 51
5.3 STM image of precursors and anthracene on Au(111) . . . . . . . . . . . 52
5.4 STS measurements of trimer structures . . . . . . . . . . . . . . . . . . 53
5.5 STM image of tetracene precursors on Au(111) . . . . . . . . . . . . . . . 54

5.6 STM image of tetracene on Au(111) . . . . . . . . . . . . . . . . . . . . . . 55
5.7 Supramolecular assemblies described by Kagome lattices . . . . . . . . . . 57

6.1 On-surface route towards hexacene . . . . . . . . . . . . . . . . . . . . . . 60
6.2 Surface-assisted deoxygenation on Au(111) . . . . . . . . . . . . . . . . . . 61
6.3 Topography and electronic resonances of intermediates Hn2O . . . . . . 63
6.4 Intermediate Hn1Oa on Au(111) . . . . . . . . . . . . . . . . . . . . . . . . 63
6.5 Self-assembly of Hn2O molecules . . . . . . . . . . . . . . . . . . . . . . . 64
6.6 Sample after annealing at a higher temperature . . . . . . . . . . . . . . . 65
6.7 STM and STS measurements of single hexacene . . . . . . . . . . . . . . 66
6.8 Imaging of molecular orbital resonances of hexacene . . . . . . . . . . . 67

7.1 On-surface chemistry of Br-substituted epoxyacenes . . . . . . . . . . . . 72
7.2 Imaging of the chemical structure of heptacene . . . . . . . . . . . . . . . 73
7.3 Imaging of an intermediate and tip-induced reaction to form heptacene . 74
7.4 Bias-dependent topography of heptacene . . . . . . . . . . . . . . . . . . 76
7.5 Molecular orbital resonances of heptacene . . . . . . . . . . . . . . . . . 78
7.6 HOMO resonance of heptacene mapped with two different tips . . . . . 79

8.1 Electronic resonances of adsorbed pent-, hex- and heptacene. . . . . . . 83

# List of supplementary figures

1 Graphical user interface of the tTp recorder. . . . . . . . . . . . . . . . . . . 88
2 Raw AFM frequency shift data . . . . . . . . . . . . . . . . . . . . . . . . . 89
3 STM images of genuine tetracene on Au(111) . . . . . . . . . . . . . . . . . 90
4 STM images of genuine tetracene on Au(111) after annealing . . . . . . . 90
5 Computed transmission function of hexacene adsorbed on Au(111) . . . 91
6 Large-scale scans of two different Hp4Br3O preparations on Au(111) . . . 92
7 Two heptacene molecules fused by a single carbon-carbon bond . . . . . 92
8 Extended tunneling spectra of a single heptacene . . . . . . . . . . . . . 93
9 Higher order resonances of heptacene . . . . . . . . . . . . . . . . . . . . 93

# List of tables

3.1 Employed samples and their preparation parameters . . . . . . . . . . . . 29
3.2 Preparation parameters for the presented on-surface experiments . . . . 34

7.1 Bias values of molecular resonances for adsorbed hexacene and heptacene 79

# 1 Introduction

Acene molecules are a series of polycyclic aromatic hydrocarbons (PAH) composed of linearly fused benzene rings. Figure 1.1a shows the respective chemical structures of oligoacenes starting from anthracene (3-acene). The next two members, tetracene (4-acene) and pentacene (5-acene), are two of the most well-studied and promising small molecules for organic electronics [1]. Oligoacenes with more than five rings are expected to show superior properties [2, 3] but they are also highly unstable under ambient conditions as large oligoacenes react with molecular oxygen or undergo photoinduced dimerization [4]. Therefore, only insufficient experimental data is available for the characterization of hexacene and beyond. Conceptually, one can think of oligoacenes as graphene nanoribbons with the narrowest possible width and a zigzag edge topology as illustrated in Figure 1.1b. In the limit of a large number of rings, the structure can be eventually treated as polymer, and one can refer to the infinite case as polyacene.

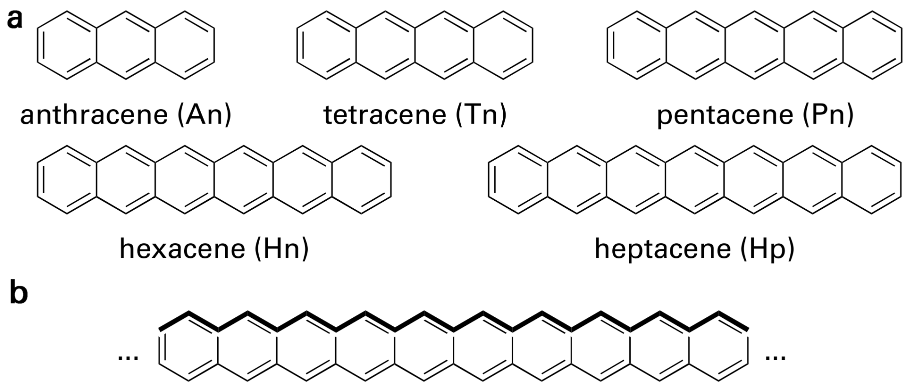

**Figure 1.1 – Chemical structure of acenes. (a):** The first five members of the oligoacenes. In this thesis, the following convention is used: anthracene, tetracene, and pentacene (top row) are referred to as the *short acenes* while acenes with more than five rings are called *large acenes* due to their extremely limited stability. **(b):** Large oligoacenes can be considered as graphene nanoribbons with a zigzag edge topology; however, the here shown decacene (10-acene) is already the smallest oligoacene which has not been detected in any experiment to date.

Ever since the pioneering synthesis attempts of E. Clar [5, 6], large acenes and their anticipated properties have intrigued scientists for many decades. While the characterization in solution or solid state has been the focus of synthetic chemists, atomic-scale investigations of single molecules have the potential to unravel their electronic structure. The recent *on-surface* synthesis and characterization of the elusive triangulene [7], a PAH with six benzene rings forming a triangle and chased by chemists for a long time, highlights the relevance of this approach. To this end, stabilization of acenes at a surface and in vacuum conditions is a promising approach to contain their high reactivity.

Since acenes have an extended conjugated backbone, their $\pi$-electrons are strongly delocalized, and the energy gap between the highest occupied molecular orbital (HOMO) and the lowest unoccupied molecular orbital (LUMO) level is decreasing with the number of benzene rings. By applying a tight-binding calculation for the $p_z$-orbitals of the carbon atoms of polyacene [8], a simple electronic level structure for acenes of a finite length can be deduced [9]. Figure 1.2a depicts the energy levels of oligoacenes schematically as a function of the size. Apparently, the energy spacing between electronic levels is closing as one would expect for a simple particle-in-a-box picture. The reduced gap between frontier levels can be related to the experimental absorption spectra. Figure 1.2b shows the longest-wavelength transitions: With increasing acene length, the absorption energy is shifted to a shorter wavenumber (red shift) indicating the shrinking HOMO-LUMO gap.

The reduced electronic level spacing, among other intriguing chemical and physical properties, makes oligoacene molecules attractive for organic electronics [3, 10, 11] as low bandgap and high mobility materials. For instance, pentacene has been widely studied in organic field-effect transistors as prototypical thin-film or crystalline semiconductor with a high charge carrier mobility [12–14]. This property is advantageous for applications in electrical engineering; however, the particularly narrow HOMO-LUMO gap of acenes results in a high reactivity and makes processing challenging. In fact, pentacene has already a limited photochemical stability under ambient conditions and slowly degrades in air [15]. Larger acenes are highly reactive and can only be handled in particular environments. For instance, hexacene (6-acene) can be obtained in-situ through a solid-state synthesis from a monoketone precursor via annealing; however, the resulting hexacene crystals and thin films must be stored in the dark to avoid a photochemical oxidation [16]. Furthermore, the work by H. Bettinger et al. showed the experimental absorption spectra of pentacene up to nonacene (9-acene) in a stabilizing solid argon matrix at 30 K [17, 18]. The respective acenes were generated in-situ from diketone precursors via irradiation. In general, large acenes require a tedious synthesis and have a very low solubility which limits its detailed characterization by standard solution-based methods.

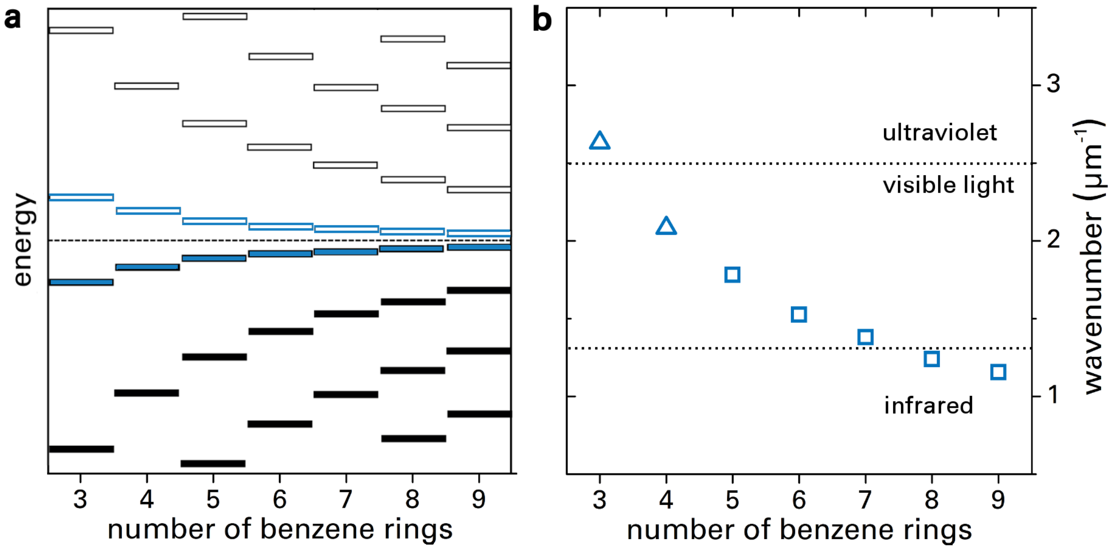

**Figure 1.2 – Energy levels and optical excitation of acenes.** **(a):** The energy levels of acenes as one would derive by applying the method of zone-folding [9] to the band structure of polyacene [8]. If a simple tight-binding model for the $\pi$-electrons of polyacene is considered and quantization conditions are imposed, the energy spacing between occupied (filled bars) and unoccupied levels for acenes of finite length can be derived. In particular, the energy gap between the highest occupied and first unoccupied level is decreasing with acene length. **(b):** The optical longest-wavelength excitations of acenes are presented as reported in the literature and correspond mainly to the HOMO-LUMO transition. The values for anthracene and tetracene were obtained in solution [19] while the larger acenes were isolated in an argon matrix [17, 18]. A recent discussion of the optical absorption data of acenes is given in [20].

The primary goal of this thesis is to explore a way for the *on-surface* fabrication of large acenes and to characterize their electronic properties at a *single-molecule level*. In this regard, on-surface chemistry provides indispensable tools for the formation of extended molecular structures which cannot be prepared by standard solution-based methods due to reasons of solubility and stability. Designing vacuum-processable precursors and inducing the final steps of synthesis on-surface is an advantageous method which has been proven to be a suitable approach to study molecular nano-architectures [21–23]. Most notably, there are many examples of the atomically precise fabrication of two-dimensional networks [24, 25] and molecular wires [26–28]. In the case of graphene nanoribbons, thermally activated and surface-assisted carbon-carbon coupling reactions followed by a cyclodehydrogenation (CDH) [29] can be employed to produce extended strips of graphene with atomically precise width and edge topology [30–32]. Spurred by the recent approaches of the stabilization of nanographene molecules through intramolecular surface reactions [33, 34], a novel way to fabricate acenes on a surface is studied in this present work.

Experimental verification of the underlying synthetic strategy is crucial and relies on the characterization of the obtained reaction products with high resolution. Recent advances in atomic force microscopy (AFM) with atomic resolution have demonstrated that this method is well suited to elucidate surface reactions due to its powerful capability to image the *chemical structure* of reaction products in real space. After the seminal work by L. Gross and coworkers on sub-molecular imaging with a CO-functionalized tip in non-contact mode [35], AFM has been applied to resolve the molecular structures of thermally activated surface reactions [34, 36–38], single-molecule chemistry [7, 39–41], as well as of natural products [42], mixtures [43], and solution chemistry synthesis [44].

Following on from the on-surface generation, studying the fabricated acene molecules with scanning tunneling microscopy (STM) and spectroscopy (STS) allows the characterization of the *electronic structure* with sub-molecular resolution. In the field of scanning probe microscopy (SPM), single-molecule investigation of pentacene can be considered as a molecular model system which has been studied by many research groups. These efforts led to groundbreaking insights and a fundamental understanding of the adsorption [45], bond formation [46], ultrafast motion [47], single-electron transfer [48], and high-resolution imaging of single molecules. The latter includes resolving the chemical structure via AFM [35], mapping the molecular orbital resonances through STM [49] and STS [50] with a metal tip, as well as a functionalized CO-terminated tip [51].

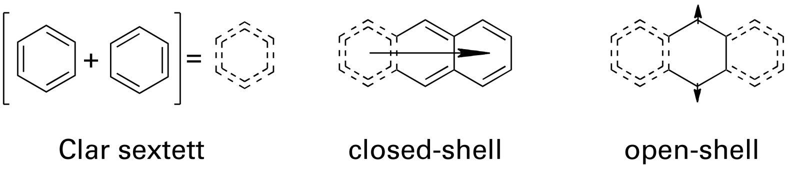

**Figure 1.3 – Resonant Clar structures of acenes as illustrated for anthracene.** The Clar structure of the closed-shell form always features just *one* $\pi$-sextet which migrates along the molecule. Therefore, the aromatic character (six $\pi$-electrons localized in a benzene-like ring) of acenes decreases with the number of rings. In contrast, the open-shell form exhibits at least *two* aromatic rings at the cost of losing one $\pi$-bond. The two unpaired electrons show an anti-ferromagnetic coupling, i.e. are in the singlet state [52]. The observed low stability of large acenes can be related to this increasing radical character in their structure [4].

Aside from the fundamental interest to make large acenes beyond pentacene accessible for on-surface and SPM investigations, they are predicted to present superior properties for molecular electronics. The central idea of using single molecules to perform basic functions of electronic circuits goes back to a pivotal paper from A. Aviram and M. A. Ratner [53]. In contrast to well-established organic technologies for light emitting diodes, solar cells, and field effect transistors, functional devices based on a single molecule are still more vision than a real technology. While there are many challenges for the fabrication and operation to make the step out of the laboratory [54], the joint efforts from chemistry and physics have already showcased novel concepts to create functionality at the ultimate smallest length scale. For instance, spin-polarized edge states in nanographene structures with zigzag topography display a promising way to use spin and charge of electrons for magnetic data storage or nano-scale and energy-efficient transistors [32, 55, 56]. Based on theoretical calculations, the ground state of acenes beyond a certain length is also predicted to become spin-polarized. This term refers to the fact that all electrons along one long zigzag edge would feature the same spin direction while an anti-ferromagnetic coupling between opposite zigzag edges is predicted [2, 57]. This intriguing property can also be illustrated in the following way: The closed-shell ground state of any acene can be described qualitatively by the Clar structure [52, 58] as depicted in Figure 1.3. One stabilizing aromatic sextet is shared among all constituting six-membered rings. At a certain acene length, it becomes energetically beneficial to break up the $\pi$-conjugation in favor of a second Clar sextet leading to a biradical structure with two unpaired $\pi$-electrons. In a similar way, one can think of a polyradical form which matches the predicted spin-polarized state [59, 60]. This magnetic property as well as a small but finite bandgap could be the cornerstone to use spin and charge transport in a single-molecule device. Thus, extended acenes are a particularly intriguing class of nano-scaled materials with possible applications for organic and molecular electronics, as well as important implication for the field of scanning probe microscopy.

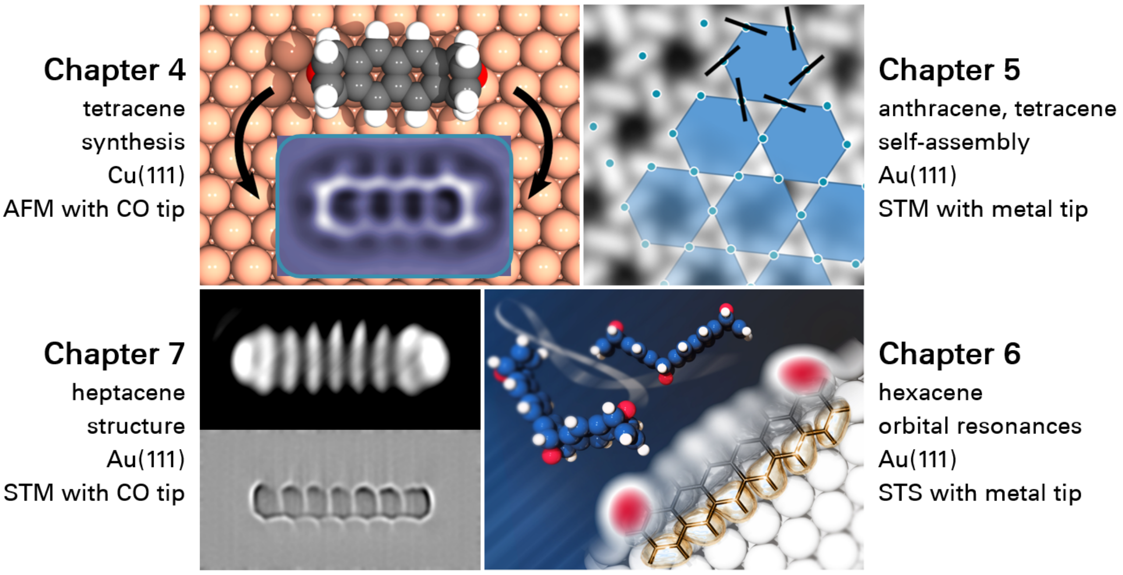
Chapter 4
tetracene
synthesis
Cu(111)
AFM with CO tip
Chapter 5
anthracene, tetracene
self-assembly
Au(111)
STM with metal tip
Chapter 7
heptacene
structure
Au(111)
STM with CO tip
Chapter 6
hexacene
orbital resonances
Au(111)
STS with metal tip

**Figure 1.4 – Graphical outline of the experimental results.** For each of the four Chapters, the studied acene molecule, the point of emphasis, used surface, and key technique is given. In addition, the findings are supported by theoretical modeling as implied by the shown visualizations.

This thesis is structured as follows: The underlying fundamentals of the employed SPM techniques are introduced in Chapter 2. Following that, a description of the used experimental setup, materials, and methods is given in Chapter 3. The key empirical findings of this thesis are presented in the following Chapters as shown by the graphical summary in Figure 1.4. First, a novel surface-assisted way to stabilize acenes in-situ is explored on Cu(111) via AFM with atomic resolution (Chapter 4). Using specially designed precursors with incorporated oxygen atoms has substantial implications for the self-assembly of fabricated acene molecules as studied on Au(111) in Chapter 5. After the thorough description of the formation of tetracene and anthracene via deoxygenation, the method of on-surface reduction is successfully applied to the larger hexacene as demonstrated in Chapter 6. Thus, this highly unstable molecule is imaged and characterized via STM and STS for the very first time. Chapter 7 shows the efforts to combine two surface reactions to explore the fabrication of acene-based polymers. Surprisingly, the data shows the stabilization of heptacene (7-acene) despite the use of Br-substituted precursors. While the chemical structures of the studied molecules are obviously similar throughout this thesis, they show an increasing complexity, and many experimental conclusions can only be derived by the systematic comparison. Besides, different scanning probe methods are employed to shine a light on the adsorbed acenes. Notably, all the experimental images of single molecules in Figure 1.4 show intramolecular resolution of the highest quality but rely on different fundamental principles. First, AFM measurements (Chapter 4) benefit from the fact that this technique is sensitive to the total electron density of the respective molecule. Therefore, the image contrast is determined by the atomic structure. Second, STS measurements resolve the extended molecular orbital resonances with their pronounced intramolecular corrugation as presented in Chapter 6 and 7. Third, STM measurements with a functionalized tip (Chapter 7) can be used to probe the atomic structure as well as the frontier orbital densities depending on the used imaging parameters. Finally, Chapter 8 presents a summary and aims to put the obtained results into perspective.

# 2 Fundamentals of scanning probe microscopy

*Scanning probe microscopy (SPM) allows investigations of a sample by moving a physical probe over the surface. Unlike optical microscopy, the spatial resolution is not limited by diffraction but instead is determined by the size of the sample-probe interaction. In this Chapter, the most important principles of the used SPM techniques are presented.*

## 2.1 Scanning tunneling microscopy

### 2.1.1 The working principle

Scanning tunneling microscopy (STM) was designed [61] and experimentally realized [62, 63] in 1982 and soon acknowledged as pioneering tool in the field of nanotechnology by awarding the Nobel Prize in physics to G. Binnig and H. Rohrer. The underlying fundamental principle is presented in Figure 2.1a and shows an atomically sharp metal tip which can be laterally scanned over a metallic substrate at a precisely controlled tip-surface height by the help of piezoelectric actuators (piezos). If the vacuum gap $d$ between both conducting electrodes is in the sub-nanometer range, the overlap of the electron wave functions of tip and substrate becomes crucial and enables tunneling through the vacuum barrier.

In the simplest case, the electron states of both electrodes are filled up to the respective Fermi energies $E_{F,t}$ and $E_{F,s}$ which can be shifted relative to each other by applying a bias voltage $V$ to this metal-vacuum-metal junction as depicted in Figure 2.1b. Despite the fact that their associated energy $eV$ is small compared to the work functions $\Phi_t$ and $\Phi_s$ of tip and substrate, electrons can still penetrate through the barrier and a tunneling current $I$ across the junction becomes measurable. Here, the convention is

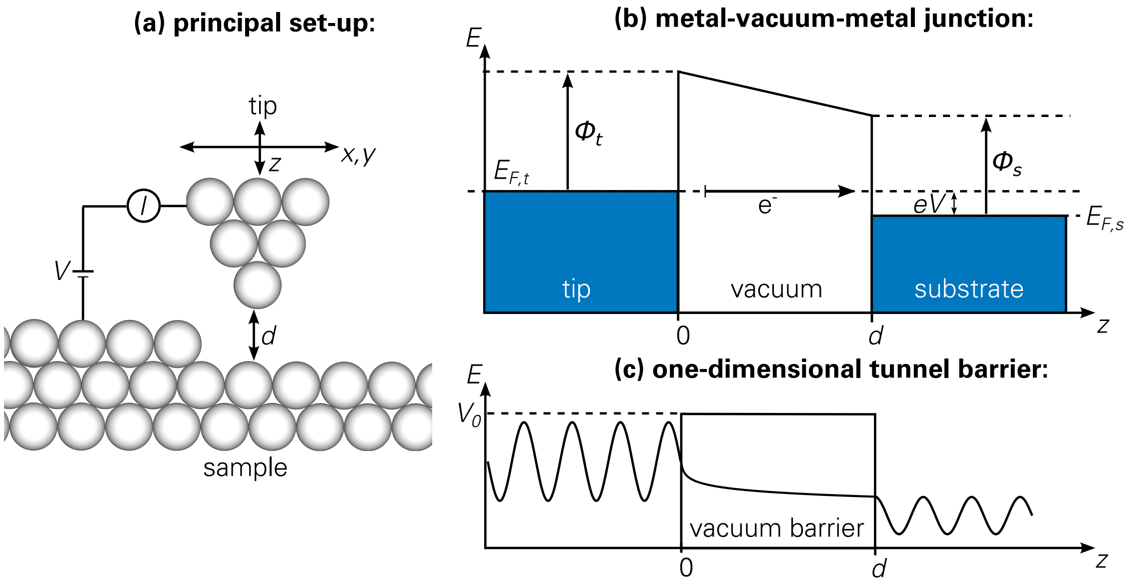

**Figure 2.1 – Basics of scanning tunneling microscopy. (a):** An atomically sharp tip is scanned over a substrate. Due to the exponential decay of the tunneling current with the distance $d$, the apex atom of the tip is dominant for STM imaging. During constant-current scanning, the tip height is determined by the applied bias $V$ and set tunneling current $I$. **(b):** Energy diagram for the general metal-vacuum-metal junction. **(c):** Real part of the electron wave function $\psi$ plotted for a one-dimensional potential barrier.

used that a *positive* bias establishes a net flow of electrons from the tip to the sample. If one treats this tunneling phenomenon as one-dimensional problem by applying elementary quantum mechanics as in [64], an incoming electron from the tip described by the time-independent wave function $\psi(z)$ has a finite probability of being localized in the sample at the position $d$:

$$|\psi(d)|^2 \propto |\psi(0)|^2 \exp(-2\kappa d)\,, \quad \text{with } \kappa = \frac{1}{\hbar}\sqrt{m_e(\Phi_t + \Phi_s - eV)} \tag{2.1}$$

This relation is valid if $eV$ is small compared to the work functions $\Phi$ of the tip and substrate, respectively. The corresponding schematic Figure 2.1c shows that the wave function is exponentially damped within the barrier. Furthermore, the tunneling current $I$ across the whole junction can be expressed as follows:

$$I(d) \propto \exp(-2\kappa d) \tag{2.2}$$

The high spatial resolution of STM relies primarily on the fact that the tunneling current decays exponentially as a function of the tip-surface gap $d$. Assuming similar materials with a typical value of $\Phi \sim 5.1$ eV for gold, the decay parameter $\kappa$ can be simplified to:

$$\kappa = \frac{1}{\hbar}\sqrt{2m_e\Phi} \sim 12\,\text{nm}^{-1} \tag{2.3}$$

Consequently, if the tip height is increased by 1 Å (Angstrom, $1 \times 10^{-10}$ m = 0.1 nm), the tunneling current will drop by approximately one order of magnitude. Due to this strong decay, the majority of the electrons tunnel between the sample and the last atom of the tip making the current very sensitive to the atomic structure of the substrate. By using a feedback loop to adjust the tip-sample height while scanning, STM is usually carried out in the *constant-current* mode. While keeping the tunneling resistance $V/I$ constant, the recorded tip height can then be plotted as a function of the lateral coordinates $x$ and $y$ to give an apparent height image of the scanned surface topography. For imaging, the range of the tunneling resistance is usually between $10^8$ Ω and $10^{12}$ Ω. On the contrary, the STM tip can also be scanned at *constant-height* without any feedback system; however, this requires high stability in the experimental setup and an atomically flat surface.

In the following, a more rigorous way to describe the tunneling current based on the formalism from J. Bardeen [65] is presented. In this approach, tip and sample are considered to be separate parts of one system, and if both are far apart [66], the corresponding electron wave functions $\Psi_t$ and $\Psi_s$ just decay into the vacuum. In proximity, the presence of a counter-electrode is treated as a perturbation potential for the respective unperturbed states. Hence, the probability that an electron is transferred from one electrode to the other is related to the tunneling matrix element $M_{t,s}$ which is defined as:

$$M_{t,s} = -\frac{\hbar^2}{2m_\mathrm{e}} \int_\Sigma (\Psi_t^* \nabla \Psi_s - \Psi_s \nabla \Psi_t^*) \, \mathrm{d}\vec{S} \tag{2.4}$$

This integral is calculated over any surface $\Sigma$ separating tip and sample, and through which the entire tunneling current flows. Accordingly, the probability $w_{t,s}$ that an electron in the state $\Psi_t$ at the energy $E_t$ tunnels into a state $\Psi_s$ and $E_s$ is known as Fermi's golden rule and given by:

$$w_{t,s} = \frac{2\pi}{\hbar} |M_{t,s}|^2 \delta(E_t - E_s) \tag{2.5}$$

Here, the $\delta$-function ensures that the energy is conserved and only elastic transitions are considered. The tunneling current at applied bias $V$ is then obtained by calculating the sum over all possible states. Since electrons can only transfer from an occupied state into an unoccupied one, the Fermi-Dirac distribution $f(E)$ must be taken into account to include the mean occupation probability of a state at energy $E$. Furthermore, one needs to subtract the transmission in the opposite direction to obtain a value for the net current:

$$\begin{aligned} I = \frac{4\pi e}{\hbar} \sum_{t,s} & \{f(E_t)[1 - f(E_s + eV)] - f(E_s + eV)[1 - f(E_t)]\} \\ & \cdot |M_{t,s}|^2 \delta(E_t - (E_s + eV)) \end{aligned} \tag{2.6}$$

where a factor of two for spin degeneracy is included. This equation holds true for a small bias $eV \ll \Phi$. Further, it can be expressed as energy integral by introducing the density of states (DOS) $\rho_t$ and $\rho_s$ for tip and sample, respectively.

$$
\begin{aligned}
I = \frac{4\pi e}{\hbar} \int_{-\infty}^{+\infty} & [f(E_F - eV + E) - f(E_F + E)] \\
& \cdot \rho_t(E_F - eV + E) \rho_s(E_F + E) |M(E, V)|^2 \, \mathrm{d}E
\end{aligned}
\tag{2.7}
$$

The Fermi energy of the sample $E_{F,s} = E_F$ is chosen as reference point for the energies, hence the tip Fermi energy $E_{F,t}$ is equal to $E_F + eV$. In the limit of low temperatures, the Fermi-Dirac distribution can be replaced by a step function and a simpler expression for the current is given by:

$$
\begin{aligned}
I &= \frac{4\pi e}{\hbar} \int_{E_F}^{E_F+eV} \rho_t(E - eV) \rho_s(E) |M(E, V)|^2 \, \mathrm{d}E \\
&= \frac{4\pi e}{\hbar} \int_{0}^{eV} \rho_t(E - eV) \rho_s(E) |M(E, V)|^2 \, \mathrm{d}E
\end{aligned}
\tag{2.8}
$$

The second equation is obtained if $E_F = 0$ is set for convenience. At this point, it becomes apparent that the tunneling current is a convolution of the DOS of tip and sample. Since the exact tip and sample wave functions are generally unknown in STM [67], the tunneling matrix element $M_{t,s}$ has to be approximated.

One of the most widely used approaches is based on the model of J. Tersoff and D. Hamann [68, 69]. Figure 2.2 shows that the tip is assumed to be point-like with radius $R$ centered at $\vec{r}_0$, thus the associated wave function has a spherical symmetry, i.e. *s*-wave character. The sample states are modeled by functions that can propagate freely on the surface but decay exponentially into the gap. By inserting this assumption in Equation 2.4, the following relation for the tunneling current between tip and sample is obtained:

$$
I \propto V \cdot \rho_t(E_F) \cdot \sum_s |\Psi_s(\vec{r}_0)|^2 \delta(E_s - E_F) = V \cdot \rho_t(E_F) \cdot \rho_s(\vec{r}_0, E_F) \tag{2.9}
$$

Consequently, the tunneling current is proportional to $\rho_s(\vec{r}_0, E_F)$ which is the local density of states (LDOS) of the sample at the Fermi energy and position of the tip apex atom. If the STM tip is scanned at constant current over the sample, the Tersoff-Hamann model shows that the *contour of constant LDOS* is probed. One should keep in mind that a number of assumptions and approximations were needed to obtain this result. Most importantly, only elastic tunneling in the limit of low temperatures was considered. The point-like tip allows one to calculate simple STM images; however, this modeling is usually not good enough to reproduces sub-atomic features in a tip-

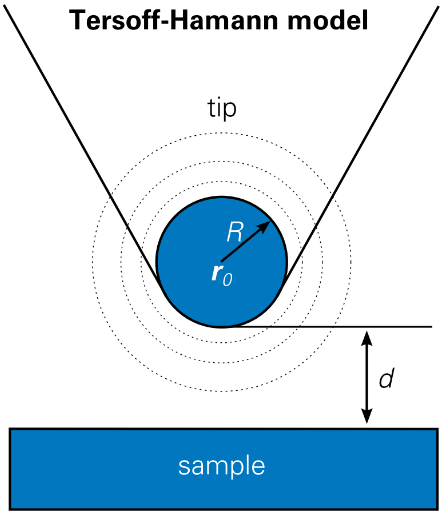

**Figure 2.2 – Tunneling geometry of the Tersoff-Hamann model.** Schematic picture of the assumed geometry. Center of tip curvature is labeled as $\vec{r}_0$ with a distance of $R + d$ to the surface. Adapted from [68].

molecule-surface system. In addition, Equation 2.9 is only true for a small bias, i.e. $eV \ll \Phi$. Otherwise, one needs to take into account that electrons with a higher energy have a larger tunneling probability because of the reduced barrier height. In the case of larger bias values, Equation 2.8 can for example be treated by the semi-classical Wentzel-Kramers-Brillouin approximation for planar electrodes [70]. In contrast to the Tersoff-Hamann model, it does not accurately describe individual sample wave function but introduces a bias-dependence via the one-dimensional transmission function $T$, assuming a trapezoidal barrier [71]:

$$T(E, V) = \exp\left[-\frac{4}{3}d\sqrt{\frac{2m}{\hbar^2}}\cdot\left(\frac{(\phi_t - E + eV)^{3/2} - (\phi_s - E)^{3/2}}{\phi_t + \phi_s + eV}\right)\right] \tag{2.10}$$

The dependence for the tunneling current is then given by:

$$I = A\cdot\int_0^{eV}\rho_t(E - eV)\rho_s(E)T(E, V)\,\mathrm{d}E \tag{2.11}$$

with a constant factor $A$. Here, the quantity $\rho_s(E)T(E, V)$ can be seen as the generalized LDOS $(E)$ in terms of the Tersoff-Hamann model since it is a measure for the charge density that reaches the tip electrode.

### 2.1.2 Scanning tunneling spectroscopy

The experimental investigations with STM are not limited to image acquisition but can be extended to spectroscopic measurements at the atomic scale. In the simplest case, the tip is stabilized over a desired position on the surface. While keeping the tip height constant, the applied bias voltage is varied and a change in the tunneling current can be recorded. The first derivative of the current with respect to the bias is of fundamental importance for scanning tunneling spectroscopy (STS). Using Equation 2.8, the following relation can be obtained [72]:

$$\begin{aligned}\frac{\mathrm{d}I}{\mathrm{d}V} &= \frac{4\pi e}{\hbar}\frac{\mathrm{d}}{\mathrm{d}V}\left[\int_0^{eV} \rho_t(E-eV)\rho_s(E)|M(E,V)|^2\,\mathrm{d}E\right]\\ &= \frac{4\pi e}{\hbar}\left[e\cdot\rho_t(0)\cdot\rho_s(eV)\cdot|M(eV,V)|^2\right]\\ &+ \frac{4\pi e}{\hbar}\left[\int_0^{eV}\rho_s(E)\frac{\partial}{\partial V}\left[\rho_t(E-eV)|M(E,V)|^2\right]\,\mathrm{d}E\right] \end{aligned} \tag{2.12}$$

The second term in this equation can be approximated to be zero if the usually unknown DOS of the tip as well as the average transfer probability $|M(E,V)|^2$ is assumed to be constant over the considered bias range. Therefore,

$$\frac{\mathrm{d}I}{\mathrm{d}V} = \frac{4\pi e^2}{\hbar}\left[\rho_t(0)\cdot\rho_s(eV)\cdot|M(eV,V)|^2\right] \propto \rho_s(eV) \tag{2.13}$$

Consequently, the slope of the tunneling current with respect to the bias is proportional to the DOS of the sample at the energy $E = eV$. In the experiment, the $\mathrm{d}I/\mathrm{d}V$ signal can be obtained by a using standard lock-in amplification technique. The applied bias is then usually modulated with a small voltage of a certain frequency $w$, i.e. $V = V_0 + V_1\sin(wt)$ with $V_1 \ll V_0$. If the tunneling current is expanded as a Taylor series around the point $V = V_0$, the following equation can be obtained:

$$I(V_0 + V_1\sin(wt)) = I(V_0) + \frac{\mathrm{d}I(V_0)}{\mathrm{d}V}\cdot V_1\cdot\sin(wt) + \frac{\mathrm{d}^2 I(V_0)}{\mathrm{d}V^2}\cdot V_1^2\cdot\sin^2(wt) + \dots \tag{2.14}$$

In this approximation, the second term describes the tunneling current modulation with the frequency $w$ while all the higher-order terms have a shorter periodicity in time. Since the lock-in amplifier basically acts as bandpass for the particular frequency $w$, the amplified signal is directly proportional to the amplitude of the first harmonic. Hence, the signal is proportional to $\mathrm{d}I/\mathrm{d}V$ at $V = V_0$. Interestingly, the amplitude of the second harmonic can be used to study processes where energy of the tunneling electrons is dissipated through vibrational [73] or rotational excitation [74]. This technique is called inelastic tunneling spectroscopy (IETS). Taking Equation 2.8 into account, the following explicit result for $I$ can be obtained [75]:

$$\begin{aligned} I &\propto \int_0^{e(V_0+V_1\sin(wt))} \rho_s(E)\,\mathrm{d}E\\ I &\propto \int_0^{eV_0}\rho_s(E)\,\mathrm{d}E + \rho_s(eV_0)eV_1\sin(wt) + \frac{\mathrm{d}\rho_s(eV_0)}{\mathrm{d}V}\frac{e^2V_1^2}{2}\sin^2(wt) + \dots \end{aligned} \tag{2.15}$$

By comparing Equation 2.14 and 2.15, the lock-in d$I$/d$V$ signal is directly proportional to the sample DOS at the energy $E = eV_0$ as expected. However, this relation is again derived by the low bias approximation; therefore, the description of the d$I$/d$V$ signal based on the WKB approximation is usually more appropriate for STS measurements with a larger voltage range of up $\sim \pm 3\,\mathrm{V}$. Since the transmission function $T$ as defined by the exponential dependence in Equation 2.10 increases strongly with the bias value $V$, the sample DOS tends to be hidden in an increasing background current. Thus, it can be beneficial to consider the normalized differential conductance as follows [72]:

$$\frac{\mathrm{d}I/\mathrm{d}V}{I/V} \sim \rho_s(eV) \cdot \left[ \frac{1}{eV} \int_0^{eV} \rho_s(E) \frac{T(E,V)}{T(eV,V)} \, \mathrm{d}E \right]^{-1} \tag{2.16}$$

Due to the fact that second factor slowly varies with voltage [72], the normalized differential conductance is an alternative way to present spectroscopic data as it is approximately proportional to the sample DOS at $eV$.

In STS experiments, the tip height is stabilized at a certain sample position. Then the feedback loop is usually switched off and the applied bias is ramped with the lock-in amplifier on to obtain a spectrum of the DOS of the sample at this point. Furthermore, the surface can also be scanned while recording the d$I$/d$V$ signal at a desired bias voltage. Similar to image acquisition, these d$I$/d$V$-maps can be carried out at constant current to make sure that the tip will not crash into the surface. The integrator time of the current feedback loop should then be large enough that no interference with the applied modulation bias can occur. Importantly, the resulting map does not only depend on the DOS but is a convolution with the sample topography [71, 76].

### 2.1.3 Single-molecule investigations

In contrast to classical and spatially averaging spectroscopy techniques, STS has the distinct advantage that investigations at the atomic scale are made possible. Therefore, this method is well suited to investigate various electronic properties of single organic molecules adsorbed on metal surfaces. Molecular orbital theory is usually the cornerstone to approximate experimental phenomena in a single-particle wave function picture, i.e. the electronic levels of a many-electron system are described by one-electron orbitals [77, 78]. In the general case of a $\pi$-conjugated system and closed-shell electronic ground state $S_0$, the energy levels of a molecule can be described by a set of orbitals each associated with a certain energy. The core orbitals established by $\sigma$-bonds between neighboring atoms are usually strongly localized and large energies are needed to probe these levels. In contrast, $\pi$-orbitals are energetically close to the vacuum level and can host electrons extending over the whole backbone of the molecule. Taking into

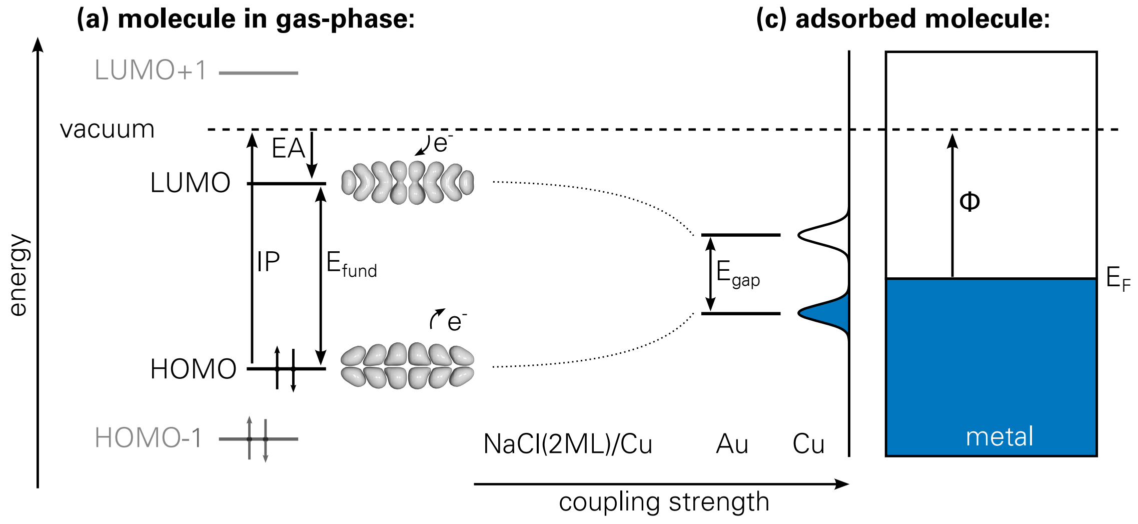

**(a) molecule in gas-phase:**

**(c) adsorbed molecule:**

**(b) electron configurations:**

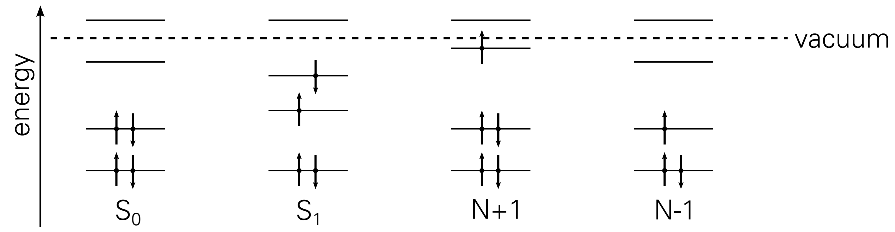

**Figure 2.3 – Simple energy level diagram of a molecule. (a):** Energy levels of a molecule in gas-phase. The electron configuration coincides with the ground state. For simplicity, the electron affinity level is referred to as LUMO level while the ionization potential level corresponds with the HOMO level. **(b):** For a molecule in vacuum and a simple picture, the electron configurations of the ground state ($S_0$), first excited state ($S_1$), electron attached state ($N+1$), and electron removed state ($N-1$) are shown. If correlation effects are included, the number and complexity of possible other electron configurations contributing to the first excited, anionic, or cationic state are much larger [78, 79]. **(c):** Shifting and broadening of the levels into resonances is observed if the molecule adsorbs on a metallic surface.

account the Aufbau and Pauli principle [64], the configuration of the ground state is determined by a number of occupied orbitals each populated by two electrons of opposite spin. Figure 2.3a shows that the occupied level which is the highest in energy is referred to as highest occupied molecular orbital (HOMO). The next higher level is called lowest unoccupied molecule orbital (LUMO) and leads a number of unoccupied orbitals. Naturally, the energy difference between the frontier molecular orbitals (HOMO and LUMO) is crucial to describe the electronic, chemical and transport properties of a molecule. However, the definition of this HOMO-LUMO gap is not straightforward [80].

Strictly speaking, molecular orbitals and their absolute energies cannot be measured [78, 81] since any probing experiment changes the ground state configuration as illustrated in Figure 2.3b. For instance, optical spectroscopy uses photon absorption to promote the system from the ground to the first *excited state* $S_1$. The energy $E_{opt}$

needed to excite an electron from the HOMO to a then singly-occupied LUMO tends to strongly differ from the energy difference between HOMO and LUMO due to Coulomb interactions. If the energy levels are probed via electron addition or removal, ionic states of the molecule are created, and the energy measurements correspond to one-electron differences. By calculating the energy difference between the frontier ionization (IP) and affinity level (EA), the fundamental gap $E_{\text{fund}}$ of the isolated molecule in vacuum is obtained. Figure 2.3a presents these quantities for a molecule in gas phase and suggests that the energy of the HOMO with respect to the vacuum level is equal to ionization potential IP while the LUMO energy coincides with electron affinity EA. However, this is a crude approximation known as Koopmans' theorem [80] and does not take relaxation processes into account which are non-negligible for electron removal or addition to form the cationic or anionic state, respectively. While the energy value of the HOMO level turns out to be usually a good approximation for the ionization level, this is usually not the case for LUMO and the first affinity level. Placing an electron into the LUMO level strongly lifts the energy of the anionic state due to Coulomb interaction [82]. This effect is the reason why the fundamental gap tends to be much larger compared to the optical HOMO-LUMO gap. Experimentally, combined ultraviolet photoelectron and electron attachment spectroscopy in gas-phase can be used to derive a value for IP-EA. Since STS experiments of adsorbed molecules also acquire a spectrum by *electronic* probing of molecular levels, the nomenclature should be simplified, and the frontier ionization and affinity levels will be referred to as HOMO level and LUMO level, respectively.

If a molecule approaches a metal surface as depicted in Figure 2.3c and adsorbs at a certain height above the substrate, the discrete molecular levels are broadened into resonances and energetically shifted due to interaction with the continuous states of the metal [83]. Here, the coupling strength and height between adsorbate and substrate is crucial for the description of the energy states at this interface [84]. Addressing the electronic properties in the low coupling regime known as physisorption has the advantage that the molecular levels still correspond to the ionization and affinity levels of the molecule in gas phase. Those resonances are accessible via STS if the associated energies are within the resonant tunneling regime and the electronic structure can then be mapped with the high spatial resolution of STM. If the tip of the STM is positioned above an adsorbed molecule and the differential conductance is probed with STS, peaks in the spectra can occur and indicate an energy resonance. At certain bias values, the conductance is enhanced due to resonant tunneling [77]. In contrast to the case of the tip being above the bare surface, electrons can then tunnel from the tip via an unoccupied molecular level into the substrate as shown in Figure 2.4a while tunneling from the sample via an occupied molecular level into the tip can also occur if the particle energy and molecular level match. One way to describe this process is the following [86]: Elec-

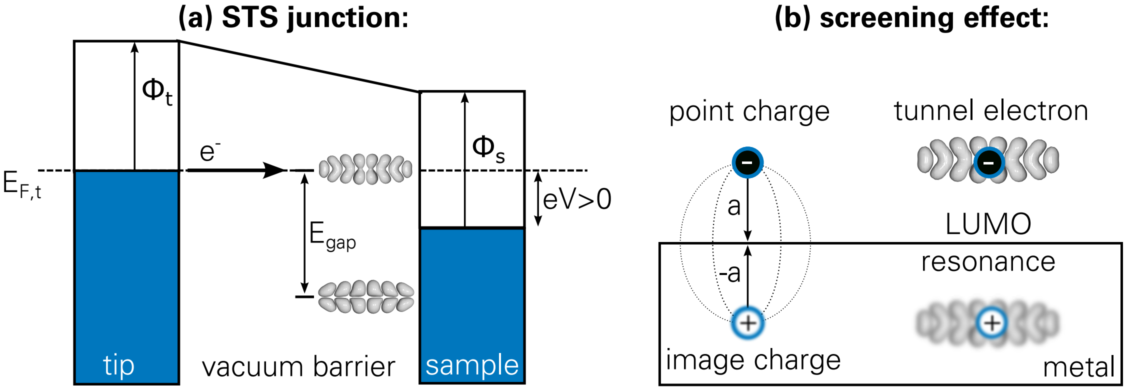

**Figure 2.4 – Organic-metal interface as probed by STS. (a):** STS junction with a resonant bias value. Thus, electrons can tunnel from the tip via an unoccupied level of the adsorbed molecule into the sample. In a similar way, occupied levels can be probed if a negative bias is applied to the STS junction. **(b):** Screening effect of the surface for a single point charge. If an electron is transfered from the tip into a sample via the transient occupation of the LUMO level, screening effects will also occur. Adapted from [85].

trons are assumed to tunnel one-by-one between tip and sample which means that the system can return to its ground state between two tunnel events. Since the molecule with $N$ electrons is physisorbed directly to the metal, tunneling through the STS junction can be viewed as a coherent process. This term describes the electron transfer through the gap as one-step process; however, the molecule retains its individuality [77]. If the Fermi level of tip or sample matches the energy of one of the molecular levels, a resonance occurs. For simplicity, one can refer to empty-state resonances as LUMO, LUMO+1, . . . while filled-state resonances can be called HOMO, HOMO-1, . . . . In a similar way, one can call the energy separation between conduction peaks around the Fermi level as the HOMO-LUMO gap of the molecule. However, one should keep in mind that strictly speaking transient electronic configurations of the molecule with $(N + 1)$ and $(N - 1)$ electrons contribute to these occupied and unoccupied level resonances, respectively.

The extracted value for the HOMO-LUMO gap by STS experiments tends to be reduced with respect to the fundamental gap value due to electrostatic screening effects at the organic-metal interface [87, 88]. This effect can be understood by the method of *image charges* as introduced in classical electrostatics as in [89]. If a point charge is placed at the distance $a$ from a metal surface as presented in 2.4b, polarization effects are induced and the resulting electric field (dashed lines) can be conveniently described by the interaction between the actual charge and its mirror image inside the metal with opposite charge value at the position $-a$. Due to the attractive Coulomb force and the mutual interaction between point and image charge, the energy of the system is lowered if the distance $a$ is decreased. In the case of a neutral molecule on a metal surface, an injected charge is stabilized in the same way [83, 85]. If for instance an electron tunnels from the STM tip into the sample via the transient occupation of the LUMO, a positive image charge is induced in the metal (Figure 2.4b) essentially lowering the energy value of the LUMO resonance [88]. Likewise, the HOMO level moves up in energy with respect to the free molecule if probed by STS. This effect of the dynamical electrostatic stabilization of both the ionization and affinity levels is enhanced with decreasing adsorption height. Consequentially, the HOMO-LUMO gap obtained in STS experiments on a metal surface is clearly reduced compared to the fundamental energy gap and usually closer to the *optical* gap value obtained by absorption measurements. One should again emphasize that this observation is not trivial since the optical value is based on the photo-excitation of a single electron to promote the molecule from the ground state $S_0$ to the first excited singlet state $S_1$.

For weakly adsorbed molecules, electron transfer through molecular resonances can become a predominant contribution of the tunneling current, and STM images at resonant bias values tend to show intramolecular features resembling the orbital density structure [49, 50]. By scanning the tip over the molecule, the tip is able to capture the lobes and nodes of the resonant states. Since the tunneling current at each pixel is proportional to the squared sample wave function as derived from Equation 2.9, the orbital densities of the molecule are probed as a first approximation [77]. Mapping the differential conductance signal has the advantage that it acts as a filter providing information for the applied resonant bias energy $eV$ only while the topography signal is obtained by integrating over an energy range.

If imaged close to the Fermi energy single molecules often markedly appear as protrusion in the STM topography even though the contributions by molecular resonances should be negligible [76]. This observation can be rationalized in part by a local reduction of the work function of the metal [83, 90, 91] since the molecule compresses the tail of the electron wave functions of the substrate which would otherwise just decay into the vacuum [88]. This so-called push-back effect leads to a collective shift of the molecular levels to lower energy values but leaves the HOMO-LUMO gap basically unaltered [92]. In the case of the strong coupling regime, there are additional mechanisms at the organic-metal interface which one needs to take into account. For instance, substantial hybridization between molecule and substrate must be considered. This interaction leads to direct charge transfer and tends to favor the occupation of the LUMO [91]. Additionally, the stronger molecule-surface bonding can change the adsorption geometry substantially and STM/STS data can eventually only be understood by detailed theoretical modeling of the whole system under investigation.

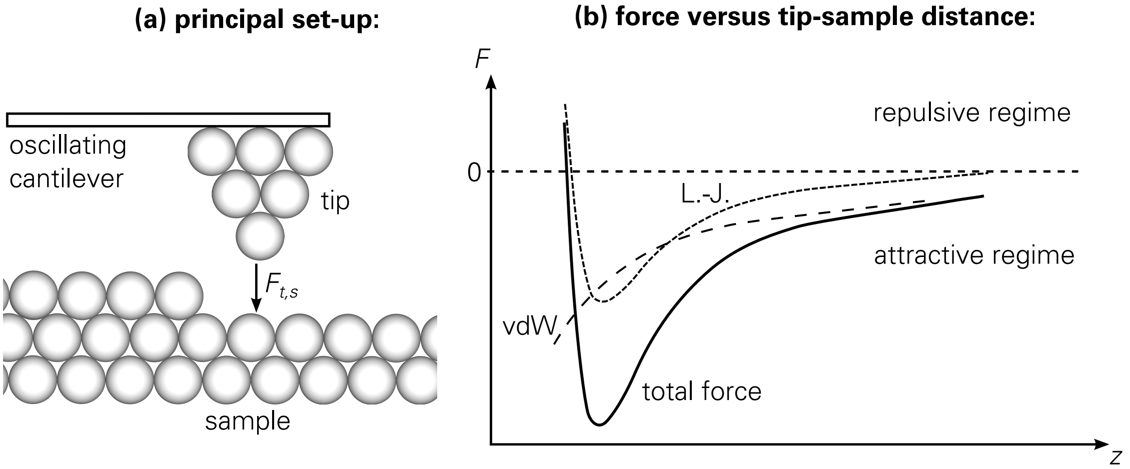

**Figure 2.5 – Basics of atomic force microscopy.** **(a):** An atomically sharp tip is attached to an oscillating cantilever and scanned over a surface. **(b):** The force between tip and sample is a superposition of long-range (vdW) and repulsive (L.-J.) contributions.

## 2.2 Atomic force microscopy

Shortly after the invention of the STM, atomic force microscopy (AFM) was introduced in 1986 by G. Binnig, C. Quate and C. Gerber [93]. Here, a sharp tip is also scanned over a sample surface; however, images are created by recording the force acting between the two as illustrated in Figure 2.5a. This method has the obvious advantage that it be can also be performed on insulating substrates and works reliably under ambient conditions. Thus, AFM has been established as most powerful and versatile tool in nanotechnology and life science. In the following, the focus is however on the principles used for high-resolution imaging using cryogenic systems and ultrahigh vacuum conditions.

Atomic resolution of single molecules can be achieved by performing AFM in the *non-contact frequency-modulated* mode [94]. Here, the tip is attached to a stiff force sensor with a spring constant $k_0$ in the order $1 \times 10^4\,\mathrm{N\,m^{-1}}$. Using a phase-locked feedback loop and driving piezo, the cantilever can be oscillated at a fixed and controllable amplitude in the vertical direction $z$. If probe and sample are macroscopically far apart, the tip with its effective mass $m^\star$ oscillates at the resonance frequency $f_0$:

$$f_0 = \frac{1}{2\pi}\sqrt{\frac{k_0}{m^\star}} \tag{2.17}$$

The interaction with the sample surface leads to a frequency shift of $\Delta f$ as soon as the tip is brought close. Figure 2.5b shows that this is caused by the force $F_{t,s}$ as sum of short range (Lennard-Jones-like) and long-range van der Waals interactions. In the limit of a small oscillation amplitude, the effect of this force on the tip can be modeled as a perturbation with a simple linear response in the vertical direction [95]:

$$k_{t,s} = -\frac{\partial F_{t,s}}{\partial z} \tag{2.18}$$

Thus and in a simple picture, the tip can be considered to be suspended between two spring-like systems. For $k_{t,s} \ll k_0$, one can derive the following expression for the frequency $f$ of the tip within this cantilever-tip-sample system:

$$f = f_0 + \frac{f_0}{2}\frac{k_{t,s}}{k_0} + \mathcal{O}\left(\frac{k_{t,s}^2}{k_0^2}\right) \tag{2.19}$$

The shift with respect to the undisturbed resonance frequency can be simplified to:

$$\Delta f = \frac{f_0}{2k_0}k_{t,s} \propto -\frac{\partial F_{t,s}}{\partial z} \tag{2.20}$$

As first approximation, the recorded $\Delta f$-data in AFM measurements at constant-height is proportional to the force gradient [66]. Since the chemical structure of a molecule is inherently connected to the short-range interactions [35], the force sensor must be able to oscillate at a very small amplitudes below 1 Å and with a quality factor $Q = f_0/\delta f$ larger than $10^5$. In most cases, the experimental realization is based on the so-called qPlus sensor which was first developed by F. Giessibl [96] and allows simultaneous STM and AFM measurement. The atomically sharp tip is then attached to one prong of a quartz tuning fork with a eigenfrequency $f_0 \sim 31$ kHz. Further technical details are presented in Section 3.2.

High-resolution AFM images of molecules are obtained by imaging at constant height. Here, the tip is scanned in one plane over the molecule while constantly oscillating at a fixed amplitude. The attractive forces between tip and sample are mainly caused by intermolecular and additive van der Waals interactions. By using electrostatics, one can show that the total force for this particular geometry follows a $-1/z^2$-dependence [97]. However, the atomic structure of a molecule is probed via the chemical forces. For two neutral atoms, the interaction consists out of a long-range attractive and short-ranged repulsive contribution. While the former is again due to the van der Waals force, the latter is frequently described as the Pauli repulsion of overlapping electron orbitals [97]. The pair potential can be model by the Lennard-Jones potential:

$$U_{\text{L.-J.}} = U_0\left(\left(\frac{z_0}{z}\right)^{12} - 2\left(\frac{z_0}{z}\right)^{6}\right) \tag{2.21}$$

where $U_0$ is the binding energy and $z_0$ the equilibrium distance. For short distances with $z < z_0$, the repulsive potential becomes the dominant contribution and the associated

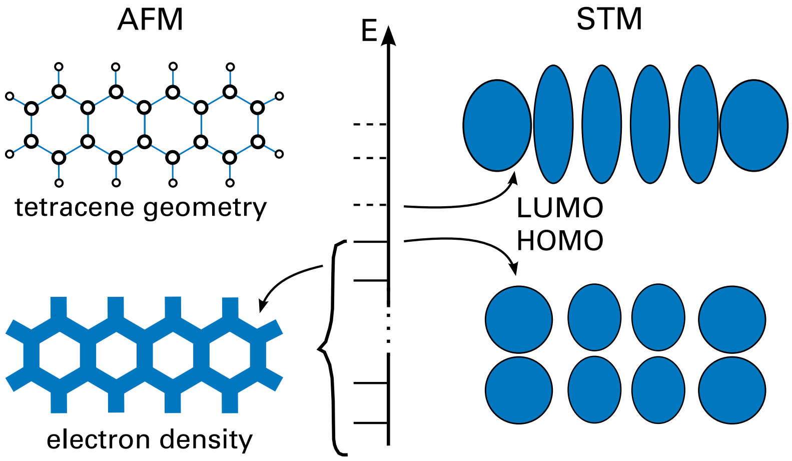

**Figure 2.6 – Scheme highlighting the difference of single-molecule imaging with AFM and STM.** Energy levels of a conjugated molecule formed by $\sigma$- and $\pi$-electrons. The AFM image is sensitive to the total electron density of the localized core electrons while STM images are created by the tunneling conductance and usually dominated by the frontier orbitals which are strongly delocalized over the molecule. Adapted from Figure 3 in [99].

force shows a $+(z_0/z)^{13}$-dependence. Consequently, the total tip-sample force $F_{t,s}$ is dominated for small distances by the chemical interaction between the apex atom and closest sample atom while the macroscopic van der Waals-interaction are the major contribution for large tip-sample distances. Figure 2.5b illustrates this description and makes it self-evident that $\Delta f > 0$ is desirable to achieve atomic resolution of a planar molecule. Interestingly, repulsive forces are usually observed on atoms *and* bonds, since both are electron-rich regions [95]. The long-range forces of the different atoms inside the molecule add up to an unspecific attractive ($\Delta f < 0$) contribution which can be observed as halo-like background around AFM images of planar molecules [35, 98].

Figure 2.6 illustrates the fact that AFM and STM can be considered to be complimentary techniques since both are sensitive to different energy levels. While highly-resolved AFM images are related to the forces by the total electron density stemming from core states and $\sigma$-bonds, STM images are derived from the frontier orbitals of the $\pi$-system. In the case of PAH, the orbital structure matches usually not the position of the carbon atoms within the backbone and the molecular states close to the Fermi levels are usually highly delocalized.

## 2.3 High-resolution imaging

The resolution in STM and AFM images of single molecules can be further increased by using a functionalized tip. This term refers to the controlled transfer of a molecule from the surface to the tip apex via vertical STM manipulation [100, 101]. Here, a metal-terminated tip is placed above the desired adsorbate, and the tip-sample interaction is increased until the molecule is picked up and transfered to the tip. A successful manipulation becomes immediately apparent via STM imaging of the same surface area again.

While there are many suitable options, carbon monoxide (CO) is most widely used for tip functionalization. It can be easily deposited in-situ and transferred from the metal surface or ultrathin insulating layer to the apex. For AFM imaging, this has the advantage that the scanning probe is depassivated [95] and can be brought much closer to the molecule under investigation without displacing it. This case is in contrast to the bare metal-terminated tip with its high reactivity, where lowering the tip height triggers a manipulation event before atomic resolution can be achieved. If instead a small CO molecule acts as apex, the effective tip radius is reduced, and the lateral resolution drastically increased, as demonstrated for many chemical structural elucidations by AFM [95, 102]. It is important to emphasize that the CO is a flexible probe and its orientation will tilt during high-resolution scans. Therefore, image distortions and sharpened bond features can occur [98, 103].

In the case of STM measurements, the symmetry of the dominant tip states has a distinct influence on the obtainable resolution. In general, a clean metal apex is considered to exhibit *s*-wave character and following on from the Tersoff-Hamann model in Section 2.1, this tip allows one to probe the squared sample wave function. On the other hand, CO-terminated tips are known to have a dominant *p*-wave symmetry [51]. Tunneling via the $\pi$-orbitals of a CO molecule allows an increased contrast since the lateral *gradient* of the squared sample wave function is probed [104]. Consequently, constant-current STM images at resonant bias carry sub-molecular features according to the respective orbital densities, as shown for pentacene on Cu(111) [35]. If also an ultrathin insulating layer is used, the obtained image with a functionalized tip even directly resembles the squared electron wave function of the frontier orbital of the gas-phase pentacene [49, 51].

While STM and AFM are in general considered to be complementary techniques for molecule characterization, the former cannot only be applied to the frontier electronic structure of a molecule but also to get an image with atomic-resolution. Usually, this requires entirely planar molecules which are then imaged at constant-height and almost zero bias below any orbital resonance. This phenomenon was first systematically studied in 2008 by introducing molecular hydrogen into the STM chamber [105]; however, it could also be reproduced for a controllably CO-terminated tip later on [42, 106]. While the detailed understanding of the atomic contrast formation in such STM measurements is still under debate [103, 107], short-range forces are considered to act on the flexible CO-terminated tip and give rise to current modulations during scanning. Thus, the apex molecule acts as force-to-current transducer [95, 108] and makes the atomic structure accessible for STM-based investigations. Whenever the tip is forced to bend away from its relaxed geometry due to the repulsive forces of electron-rich (bonds and atoms) areas in a molecule, sharp and spatially localized deviations from a unspecific tunneling current background can be deduced and forms an atomic contrast in the image of a single molecule.

# 3 Experimental setup, materials, and methods

*Single-molecule investigations require an experimental setup of the highest stability and cleanliness. In this Chapter, the experimental details on the microscope, materials, and sample preparation used in this work are given. In addition, the employed modeling methods are shortly introduced.*

## 3.1 Low-temperature scanning probe microscope

The experiments were carried out in two different setups. All the results on Au(111) were obtained at TU Dresden in a custom-built scanning probe microscope (SPM) from SPS-Createc GmbH [109, 110] while a home-built modified version of this instrument was used for the measurements on Cu(111). The latter system is optimized for combined STM/AFM imaging of single molecules with the highest resolution and operated at IBM Research—Zurich. Since both setups have a very similar principal design, the following description is mainly focused on the instrument used for STM measurements in Dresden while a detailed description of the specifics for low-noise SPM measurements can be found in the literature [111, 112].

All the experiments were carried out in ultrahigh vacuum (UHV) conditions with a base pressure better than $1 \times 10^{-10}$ mbar. Such an environment is achieved by using a combination of different pumps for the vacuum system as depicted in Figure 3.1a. The setup is divided into three units separable by all-metal gate valves: load-lock, preparation (PREP) chamber and STM chamber. The respective pressure values can be monitored by ionization gauges at each stage. The benefits of having three different parts in one UHV system (see Figure 3.1b) will be illustrated by describing the preparation process of a sample. First, the substrate desired for on-surface experiments is inserted into the load-lock at ambient conditions. By using a turbomolecular pump and optionally baking

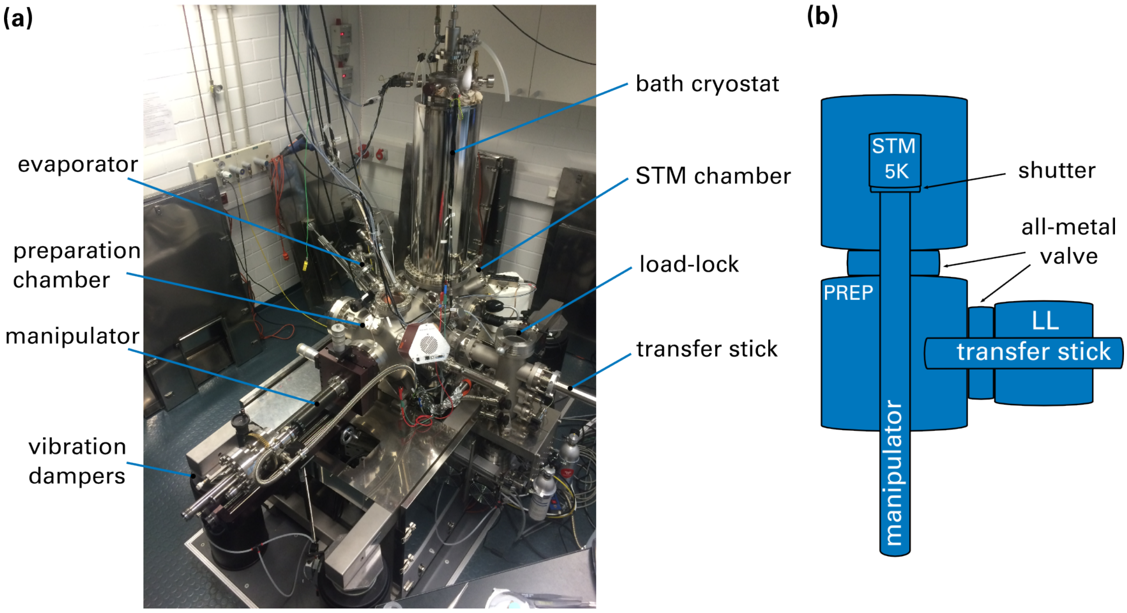

**Figure 3.1 – UHV system used for the experiments.** **(a):** Picture of the UHV system used for experiments on Au(111) in Dresden. In principle, the shown system could also be used for AFM investigation but was used for STM/STS measurements only. **(b):** Corresponding scheme (top-view) showing that the setup is divided into three separable units: load-lock (LL), preparation (PREP) and STM chamber.

out at 120 °C, the pressure inside this small chamber can be reduced to the order of $10^{-9}$ mbar within approximately 1 h. Once a sufficiently low pressure value is reached, the sample can be passed through a gate valve into the preparation chamber by making use of a transfer stick. From this point on, the sample is handled via a manipulator system which allows precise positioning inside the chamber within a limited range of motion. A combined ion-getter and titan-sublimation pump is used in this part of the system to maintain UHV conditions. To further analyze the rest gas, a quadruple mass spectrometer can be utilized. Additionally, the preparation chamber houses a sputter gun (Specs) and a gas inlet with a leak valve. These parts are essential to obtain an atomically clean metal surface via sputtering. Furthermore, a temperature-controlled evaporator (Kentax) can be used to deposit molecular material onto the surface. Once the sample is prepared in the desired way, it is transferred into the microscope inside the measurement chamber. At this point, one makes use of the fact that the manipulator system can be cooled with liquid nitrogen to speed up the transfer process of the attached sample from room temperature down to measuring temperature. Once the sample reaches $T \sim 77$ K, it is detached from the manipulator and put onto the sample support inside the STM where it cools further down. The microscope itself is always kept at $T = 5$ K via coupling to a bath cryostat. Two shields of liquid nitrogen and liquid helium ensure a low consumption and require refilling every 72-90 h only. While the measurement chamber is also operated via a combined ion-getter and titan-sublim-

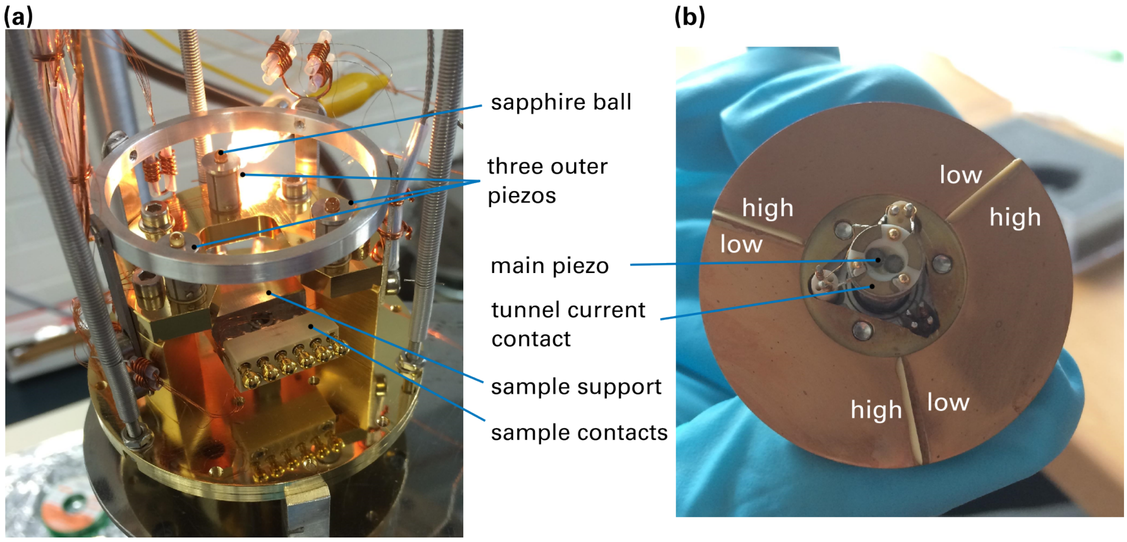

**Figure 3.2 – SPM scanner unit divided into two parts.** **(a):** U-shaped base plate of the scanning probe microscope with three coarse piezos. The sample (not shown here) can be put onto the sample support and is then pushed against the base plate from below. **(b):** Fourth and identically built piezo is attached to a sector ramp. The height difference between the high and low segments of the ramp is 600 µm.

ation pump, the pressure close to the surface of interest within the microscope can be considered to be markedly lower than the base value. This effect is related to the low temperature and the cryogenic pump effect of the microscope walls. Therefore, the sample surface can be investigated for a long time without any noticeable increase of contaminations.

The design of the scanning probe microscope is based on the Besocke beetle-type scanner [113]. In a nutshell, the sample remains in its position while the tip can be scanned over the surface by a highly optimized mechanism. To this end, three tube piezos are assembled on the base plate around the sample support as shown Figure 3.2a. The fourth main piezo is attached to the center of a sector ramp as depicted in Figure 3.2b and can carry the sensor of the SPM via magnetic forces. If the scanner unit is assembled, the sector ramp (see Figure 3.3a) rests on sapphire balls that are glued to the three outer piezos. If an AFM or STM sensor is attached to the main piezo, the tip-sample distance can be precisely controlled by the extension of this piezo while a lateral motion is achieved by its bending. However, one of the main challenges of any scanning probe microscope is to scan a surface with atomic precision and high stability but also to have a coarse approach mechanism at the same time. In the present setup, one can apply cycles of a suitable sawtooth voltage to the three outer piezos which induces a kind of stick and slip motion of the entire ramp and allows coarse movement and approaching of the surface after the sample was inserted. Here, the ramp is designed in such a way that a vertical displacement of up to 600 µm can be

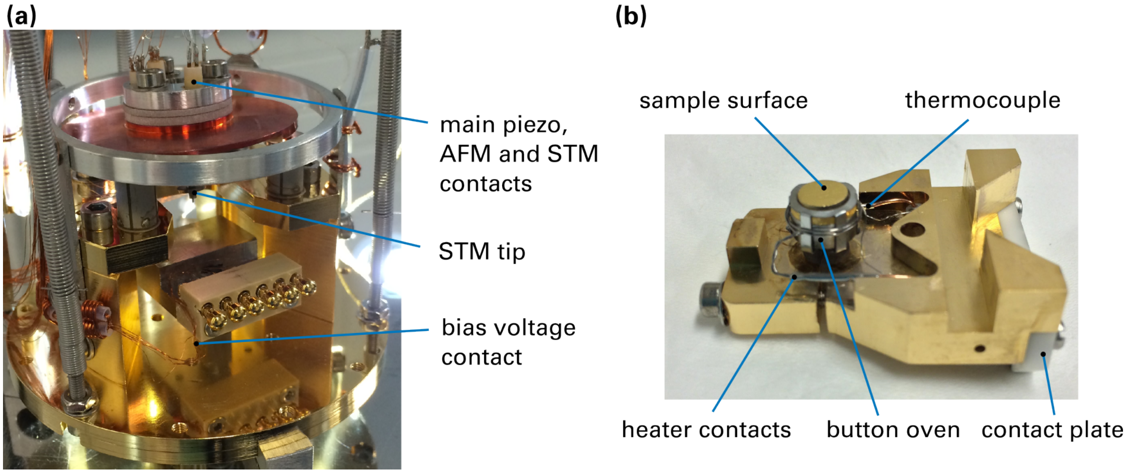

**Figure 3.3 – Assembled scanner unit. (a):** Sector ramp with an STM tip attached to the main piezo rests on the three coarse piezos. **(b):** Au(111) sample holder used for the experiments.

obtained. Thus, the distance between surface and apex of the sensor can be lowered in a controlled manner until a microscopic gap is achieved.

Furthermore, all three coarse piezos can also be collectively actuated in such a way that fine scanning of the entire ramp (including the tip) in the lateral ($x$, $y$) and vertical $z$- direction is made up possible. This configuration was used for all experiment and has the advantage that the main piezo is no longer needed to scan the surface and to control the tip-surface height but can be used to drive the tuning fork of an AFM sensor.

Figure 3.3b shows the setup of the employed sample holder. Here, the Au(111) sample is fixed on a button heater with an attached Ni/Cr-Ni (type K) thermocouple. By soldering the thermocouple as well as the electrical contacts of the oven to the contact plate, the sample can be heated while being attached to the manipulator of the UHV system. A maximum current of about 3.5 A can be passed through the heating connections to achieve the desired annealing temperatures. Once the sample is inside the STM, the same contact plate is used to apply the bias voltage to the substrate.

For measurements, the tip of the microscope is brought close to the surface until a tunneling current becomes detectable. As a matter of fact, this current signal is converted via an amplifier (Femto) into a voltage signal with a typical gain of $1 \times 10^{9}\,\mathrm{V\,A^{-1}}$. By using a digital signal processor board, the measured current value is compared to the set value of the feedback loop, and tip height is adjusted accordingly. Here, the three coarse piezos are fed by a high voltage source to achieve the desired displacement of the tip. In the case of STM experiments on Au(111) at 5 K, the vertical resolution is approximately 1 pm and the minimum obtainable stable current value is in the order of 1 pA. For scanning, the maximum lateral distance is about 300 nm in the $x$ and $y$-directions. The lateral resolution with a metal-terminated tip can be estimated to be around 1 Å.

## 3.2 Sensors and tip preparation

Two different sensors were used as shown in Figure 3.4a. STM measurements on Au(111) were performed with an electrochemically etched tungsten tip prepared from a wire with a diameter of 25 µm. This tip was subsequently flashed inside the UHV system to get rid of the inevitable oxide layer. For Cu(111) and NaCl(2ML) experiments, combined AFM/STM measurements were carried out with the help of a sensor based on the qPlus design featuring a Pt/Ir wire with a diameter of 25 µm attached to a tuning fork [96]. The SPM tip was prepared by focus ion beam cutting of the Pt/Ir wire. An overview of the sensor characteristics is given in the panels b and c of Figure 3.4.

An atomically sharp metal-terminated tip with *s*-wave symmetry was achieved in both setups by repeated and controlled crashing of the apex into the clean metal substrate and subsequent imaging until a satisfactory resolution was obtained. For the STS measurements on Au(111), only those tips were used which showed the surface state at −0.51 V as the dominant feature in the tunneling spectra [114].

Atomic-resolution images of single molecules were obtained by functionalizing a metal-terminated tip with a single CO molecule at its apex. This modification was achieved in both setups by depositing CO molecules with a very low surface coverage onto the respective samples kept at below 10 K. Subsequently, controlled vertical manipulation [101] was performed to obtain a CO-terminated tip with pronounced *p*-wave character as already discussed in Section 2.3. Starting with a metal-terminated tip, CO molecules were imaged as circular depressions on the surface, and the tip could be directly placed above a single CO molecule. By turning off the STM feedback loop and lowering the tip height, the interaction with the molecule was increased enhancing the chances of a manipulation event. If the CO molecule jumped to the apex, a sudden change in the tunneling current was recorded. After turning the STM feedback loop on again, the tip height over the bar metal appeared lowered.

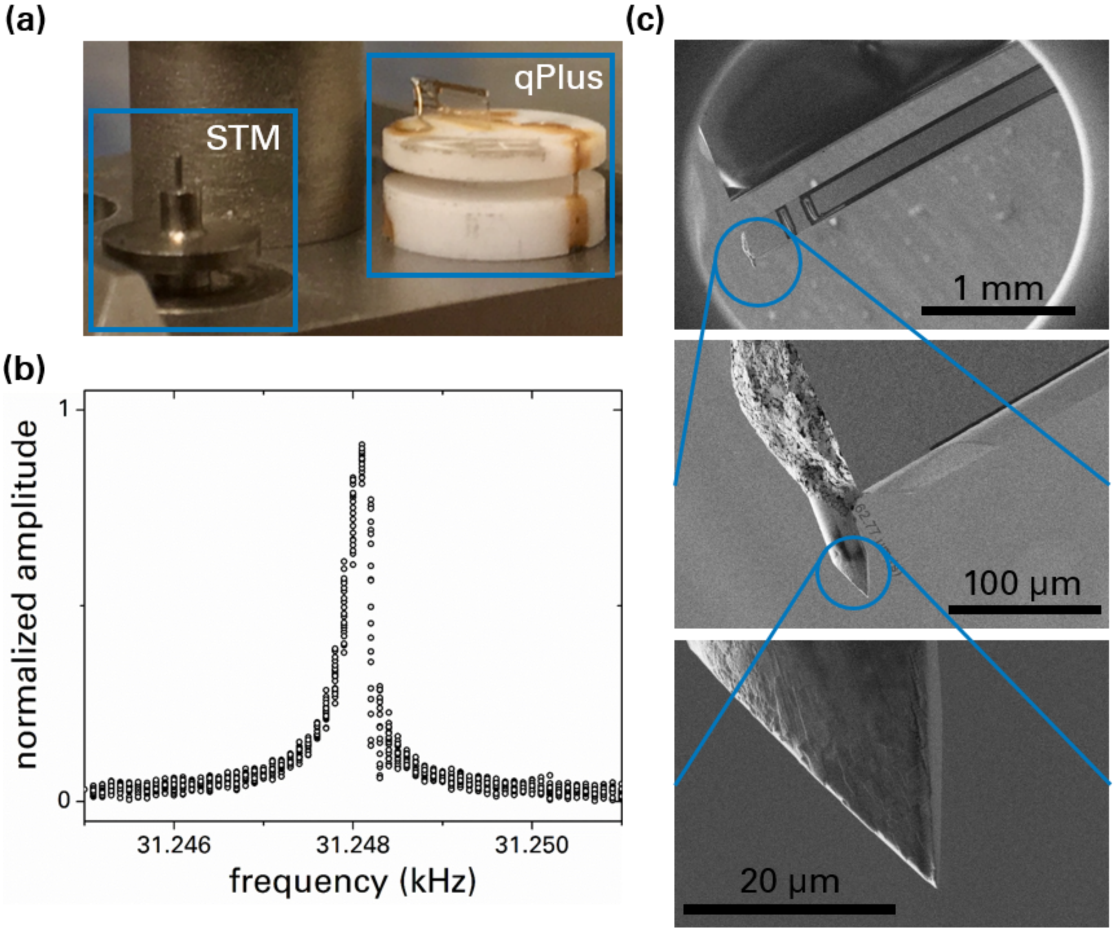

**Figure 3.4 – Employed STM and STM/AFM sensors.** **(a):** Photography of an STM tip (left) and qPlus sensor **(b):** By sweeping the driving frequency, the extremely sharp resonance of such a qPlus sensor becomes vivid. This measurement was obtained in-situ, i.e. at 5 K and UHV conditions. **(c):** Series of scanning electron microscopy images of the scanner shown in (a): A conducting wire is attached to the lower prong of the tuning fork. After focused ion beam treatment, the atomically sharp SPM tip has a total length of about 60 µm. This particular tip was prepared with the help of L. Gross at the *Binning and Rohrer Nanotechnology Center*, IBM Research—Zurich.

## 3.3 Substrates

Scanning tunneling microscopy requires a conducting substrate. The high-symmetry surfaces of coinage metals have the advantage that they are easily prepared by repeated cycles of sputtering and annealing. To get rid of surface contamination and adsorbents of any kind, noble gas ion sputtering with $Ne^+$ or $Ar^+$ at an ion energy of 1 keV and a PREP chamber pressure value of approximately $4 \times 10^{-5}$ mbar was employed. Since this procedure also increases the roughness of the surface, subsequent annealing at temperatures in the range of 700 K - 900 K was applied to the substrate. This experimental protocol leads to clean and atomically flat terraces with up to many 100 nm as lateral dimensions. In the present work, clean Au(111) and Cu(111) surfaces with the properties stated in Table 3.1 were used as substrates to investigate adsorbed single molecules. The former surface was also shortly flashed to an elevated temperature to obtain a clean surface reconstruction. The details of this feature will be introduced in the following Section.

| substrate | work function | bulk atom spacing | annealing temp. | time | flashing |
|---|---|---|---|---|---|
| Au(111) | 5.35 eV | 288 pm | 723 K | 10 min | 773 K |
| Cu(111) | 4.90 eV | 256 pm | 900 K | 15 min | no |

**Table 3.1 – Employed samples and their preparation parameters.** The values for the work functions are taken from [50, 84] while the values for the lattice spacing are from [115].

### 3.3.1 Au(111)

Gold has a close-packed face-centered cubic (fcc) crystal structure as presented in Figure 3.5a. The lattice constant is about 4.08 Å for the bulk material [115]. This value translates into a distance between neighboring atoms of about 2.88 Å. In surface science, the (111) plane is one of the most widely studied facets of gold. It features a hexagonal lattice and three close-packed directions as indicated by the triangle in Figure 3.5b. The atomic corrugation of the substrate can be visualized by STM as shown in Figure 3.5c; however, this kind of high resolution imaging usually requires a *p*-wave character of the tip. Here, atomic resolution was obtained by imaging with a functionalized CO-terminated tip at constant height. The atomic lattice is used to calibrate the lateral scale of the *x*, *y*- piezos. Similarly, the height difference of 2.35 Å for the mono-atomic step between two Au(111) terraces can be used to calibrate the scale for *z*-piezo.

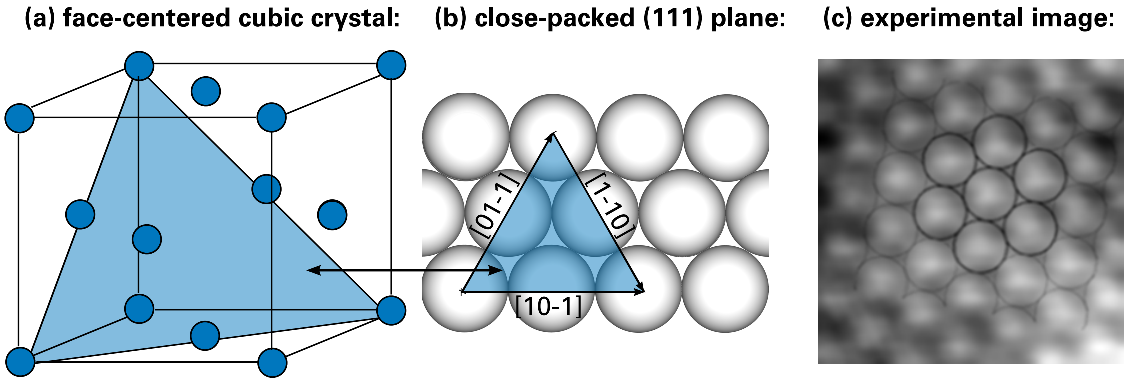
**(a) face-centered cubic crystal:** **(b) close-packed (111) plane:** **(c) experimental image:**

**Figure 3.5 – Crystal structure of the used samples.** (a): Unit cell of the face-centered cubic crystal. The colored plane corresponds to the (111) facet. (b): The hexagonal lattice in the (111) plane with the three close-packed directions. (c): Experimental STM image (17 Å x 17 Å) acquired with a CO-tip at constant height shows atomic corrugation of Au(111). The hexagonal lattice is superimposed.

One peculiar property of the Au(111) surface is the fact that it exhibits a reconstruction which is the energetically preferred state of the surface after flash-preparing. For the topmost surface layer and along one of the three close-packed directions, every 23 atoms fit into 22 lattice sites [116]. Hence, there is a mismatch between the first and second surface layer which gives rise to small height modulation of the surface. In a nutshell, inherent strain in one closed-packed direction is relaxed over two dimensions to form the reconstruction. While most parts of the top layer can either be associated with an fcc-like or hexagonal closed packed (hcp)-like alignment, both regions are separated by a slight buckling which becomes apparent as straight ridges in the STM image of a clean Au(111) surface. This motif governs the whole surface and leads to a characteristic and long-range herringbone pattern as presented in Figure 3.6a. Particular interesting adsorption sites of molecules on Au(111) are the so-called kink or elbow sites as defined in the same Figure, since single molecules tend to be more strongly attached compared to other terrace sites [50]. While the long-range pattern is easy to image with a metal-terminated tip, atomic resolution on the same sample preparation (see Figure 3.6b) was again obtained with a functionalized tip.

The (111) facet of noble metals is known to exhibit a Shockley surface state [117] which stems from electrons at the interface with a quasi-free particle dispersion. In the case of Au(111), the band minimum of the surface state is 0.51 eV below the Fermi energy [114].

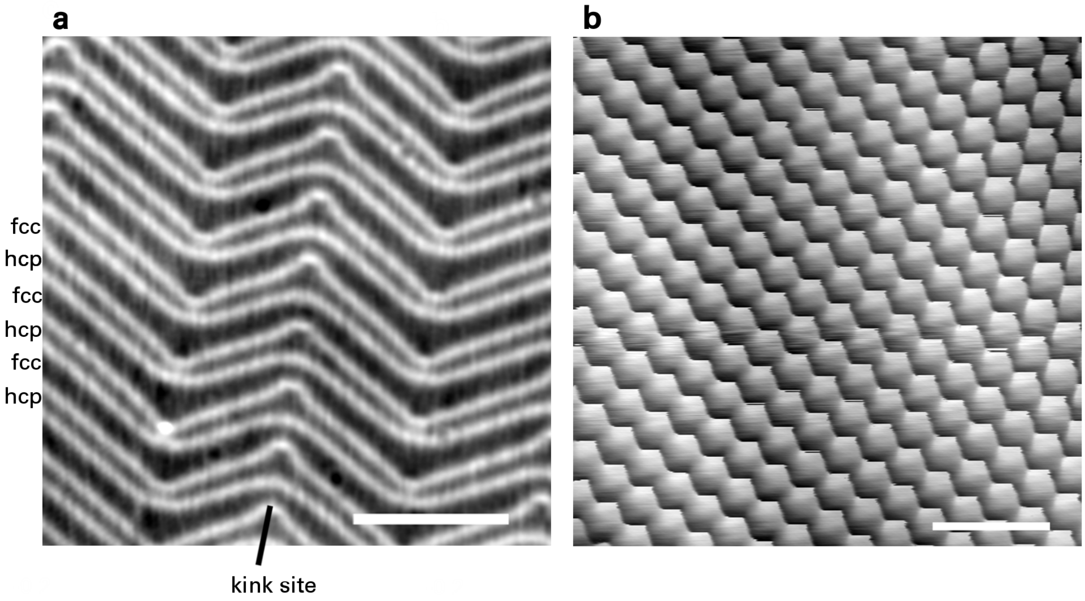

**Figure 3.6 – Long- and short-range periodicity of the Au(111) surface. (a):** STM overview scan ($I$ = 20 pA, $V$ = 0.2 V) of one terrace on the clean substrate. The characteristic herringbone pattern with alternating fcc and hcp domains is visible. In addition, the definition of a kink site becomes apparent. The black and weight color scale refers to an apparent height difference of 20 pm. Scale bar is equal to 20 nm. **(b):** Close-up scan ($I$ = 0.2 nA, $V$ = 0.2 V) of the atomic lattice obtained with an accidentally functionalized tip. Since the gold atoms also follow the surface reconstruction, a continuous variation of the contrast is noticeably in the image. Scale bar refers to 1 nm.

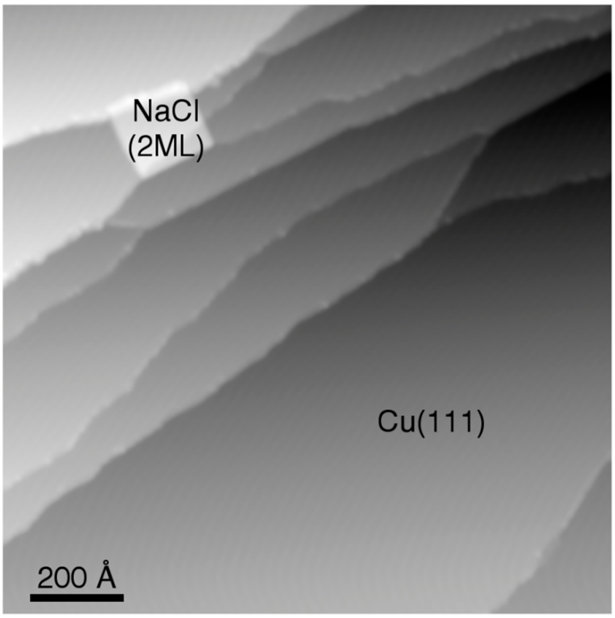

**Figure 3.7 – STM overview of the Cu(111) surface.** Several terraces are visible which are separated by mono-atomic step edges. In addition, a rectangular island of two-layers of NaCl is visible. Scanning conditions: 0.5 V and 2 pA.

### 3.3.2 Cu(111)

Copper features also the face-centered cubic crystal (fcc) structure; however, with a distinctly smaller lattice constant of 3.62 Å for the bulk phase [115]. This value translates to a nearest neighbor distance of 2.56 Å in the (111) plane. Importantly, this facet shows no surface reconstruction.

In addition, NaCl was evaporated onto the Cu(111) surface at a sample temperature of about $T = 270\,\mathrm{K}$. This lead to the formation of (100)-oriented NaCL islands (denoted as NaCl(2ML) in the Figure 3.7) with a thickness of two atomic layers. The crystal structure of this system is again the fcc structure but with a two-atomic basis. The nearest neighbor distance between the ions is equal to 2.82 Å [115]. Despite the fact that bulk NaCl is an insulator with a large energy gap of 8.6 eV [118], electrons can still tunnel through these ultrathin insulating films. However, the absolute tip height over NaCl(2ML) must be clearly reduced compared to bare Cu(111) to obtain the same tunneling current at a fixed bias.

## 3.4 Imaging

The vast majority of SPM measurements were performed in constant-current mode. Only for high-resolution images of single-molecules with atomic resolution, AFM and STM were carried out at constant-height. Here, the presented data was post-processed using Gaussian low-pass and Laplace-filter. This procedure is a widely used technique in image processing to detect edges and increases the contrast of sub-molecular or atomic features in the SPM data. The software Gwyddion[1] was used for image processing.

Differential conductance images were always obtained at constant-current using a metal-terminated tip. The first derivative of the tunneling current was detected by a lock-in system with a modulation frequency of 833 Hz and an amplitude in the range of 20 mV - 40 mV. Those maps were usually also low-pass filtered to increase the visibility of sub-molecular features.

## 3.5 Molecular materials

### 3.5.1 Precursors

The investigated molecules, their chemical structures, and used abbreviation are shown in Figure 3.8a. All four compounds with 1,4-epoxy groups were prepared by Diels-Alder solution chemistry and provided by the group of Diego Peña at CiQUS, University of

---

[1] Gwyddion 2.39, free and open source software, http://www.gwyddion.net

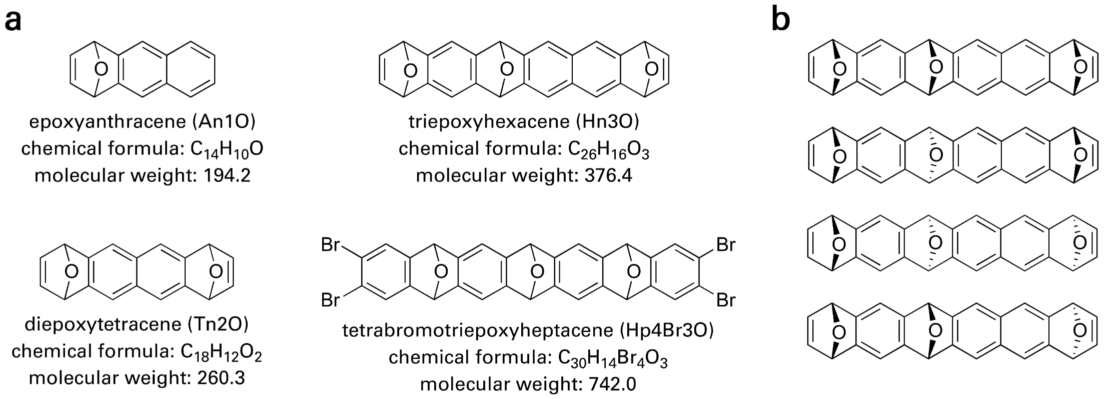

epoxyanthracene (An1O)
chemical formula: $C_{14}H_{10}O$
molecular weight: 194.2

triepoxyhexacene (Hn3O)
chemical formula: $C_{26}H_{16}O_3$
molecular weight: 376.4

diepoxytetracene (Tn2O)
chemical formula: $C_{18}H_{12}O_2$
molecular weight: 260.3

tetrabromotriepoxyheptacene (Hp4Br3O)
chemical formula: $C_{30}H_{14}Br_4O_3$
molecular weight: 742.0

**Figure 3.8 – Molecular materials used in the experiments. (a):** Four different precursors molecules which were investigated in this thesis. In all cases, the epoxy group is at the 1,4-position of the backbone meaning that two carbon atoms at opposite sites are bridged via one oxygen. **(b):** The four diastereomers of Hn3O.

Santiago de Compostela in Spain. Further details on the synthetic strategy to prepare epoxyacenes and detailed characterization of Tn2O and Hn3O can be found in [119, 120].

For on-surface experiments, the molecular compounds were sublimated from a quartz crucible in a Knudsen cell inside the preparation chamber at UHV conditions. In order to ensure that preparations could be carried out in a controlled and reproducible way, I designed a LabView-based program called *tTp-Recorder* from scratch. The graphical user interface is shown in Section A.1 of the Appendix and allows one to monitor pressure values as well as to control the crucible temperature with highest precision. The used crucible temperatures and investigated annealing experiments are shown in Table 3.2.

Notably, all shown precursors larger than An1O are a diastereomeric mixture which means that it contains a number of (stereo)isomers. For Tn2O, the two epoxy groups can either be in *syn*- or *anti*-configuration. Both diastereomers[2] have approximately the same share as confirmed by nuclear magnetic resonances spectra [119]. The larger precursors Hn3O and Hp4Br3O with three epoxy groups are a mixture of four and three different isomers, respectively. Figure 3.8b displays all four possible configuration of the Hn3O. The presence of functional groups has strong implications for the gas-phase geometry of the molecules under investigation as presented in Figure 3.9.

---

[2] For simplicity, diastereomers will also be called isomers throughout this thesis.

| molecule | crucible temp. | substrate | annealing temperatures |
|---|---|---|---|
| An1O | 320 K | Au(111) | as-prepared, 340 K, 390 K |
| Tn2O | 410 K | Cu(111), Au(111) | as-prepared, 390 K |
| Hn3O | 470 K | Au(111) | 390 K, 420 K |
| Hp4Br3O | 620 K | Au(111) | 470 K, 530 K |

**Table 3.2 – Preparation parameters for the presented on-surface experiments.** The indicated crucible temperature was needed to obtain a sub-monolayer coverage after depositing for 30-60 s. Annealing experiments were carried out via keeping the stated temperature for 5 min.

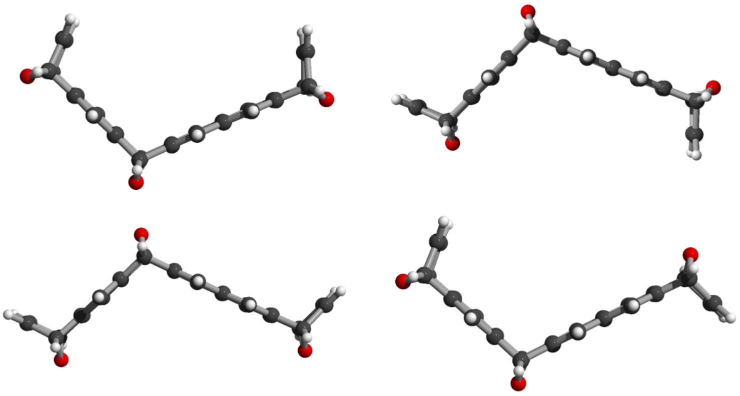

**Figure 3.9 – Simple gas-phase model of the hexacene precursors Hn3O.** All four possible diastereomers are shown with their pronounced non-planar geometry.

### 3.5.2 Perimeter free electron model

After a successful deoxygenation, the reduced forms of the investigated precursors feature a planar and fully $\pi$-conjugated polycyclic backbone. In that case, the so-called perimeter free electron model [121] is a simple but intuitive model to rationalize the HOMO-LUMO gap as function of acene length $n$. Each carbon atom contributes one $\pi$-electron which can move freely around the oval-shaped molecular perimeter embedded in an infinite potential. Thus, the $(2 + 4n)$ electrons in the $\pi$-system of an n-acene are treated as non-interacting particles confined on a 1D ring and a simple plane wave as function of the ring angle $\varphi$ solves the corresponding Schrödinger equation of the system. Conceptually, this is very similar to the quantum mechanical model of a particle in a box but with periodic boundary conditions. Therefore, the following expression for the energy $E_q$ can be derived:

$$E_q = \frac{2\pi^2\hbar^2}{m_e}\left(\frac{q}{L}\right)^2 \tag{3.1}$$

with $q = 0, \pm1, \pm2, \ldots$ as quantum number and $L = (2 + 4n)a$ as perimeter length using the carbon-carbon interatomic distance $a$. Given the spin and level degeneracy, four electrons can occupy each state with $q > 0$. Thus, the highest occupied level $E_q$ for an n-acene is obtained for $q = n$ and the HOMO-LUMO gap can be calculated:

$$\Delta E_n = \frac{\pi^2 \hbar^2}{2 m_\mathrm{e} a^2} \left( \frac{1}{2n+1} \right) \propto \frac{1}{n} \tag{3.2}$$

Accordingly, the energy spacing scales with $1/n$ and reproduces the trend in available experimental data for short acenes [121, 122] illustrating the delocalized nature of the frontier orbitals. Obviously, this model is extremely crude and more sophisticated approaches are needed to describe the energy separation of the molecular orbitals accurately. From a fundamental point of view and within the simple model, the predicted increasing radical character of the ground state [57, 123] is at odds with a vanishing energy gap for $n \to \infty$, since a transition from a closed-shell to an open-shell shell ground state is conceptually equivalent to the break down of the full $\pi$-conjugation of the molecule [52, 124].

## 3.6 Modeling

The analysis of scanning probe investigations of single molecules can be tremendously improved by the help of theoretical modeling. In this work, the adsorption geometry of non-planar precursors, intermediates, and acenes were addressed via density functional theory (DFT) calculations while the differential conductance maps of single molecules were simulated by the elastic scattering quantum chemistry (ESQC) code. In this thesis, all the shown sophisticated models and calculations were performed by Thomas Lehmann under the supervision of Dmitry A. Ryndyk and Christian Joachim. In contrast, the shown geometry and frontier orbital calculations of free molecules were obtained by the help of ArgusLab[3].

### 3.6.1 Density functional theory

In physics and chemistry, this theory is a well-established and widely applicable general method to derive the properties of a many-body system in the ground state [125]. Based on a theorem from P. Hohenberg and W. Kohn [126], the electron density $n_e = f(\vec{r})$ of interacting electrons determines the potential $V(\vec{r})$ and thus also the ground state wave function of this system uniquely. In addition, the total ground state energy $E_\mathrm{tot}$ of system of electron and ions[4] can be expressed as unique functional of $n_e$ [127]:

$$E_\mathrm{tot}[n_e] = T_\mathrm{S}[n_e] + E_\mathrm{ion}(\{\vec{R}_a\}, [n_e]) + E_\mathrm{H}[n_e] + E_\mathrm{XC}[n_e] \tag{3.3}$$

---

[3] ArgusLab 4.0.1, M. A. Thompson, Planaria Software LLC, Seattle, WA, http://www.arguslab.com

[4] treated in the widely applied Born-Oppenheimer approximation

where the five summands have the following meaning: kinetic energy of the electrons, electron-ion energy, electron-electron Coulomb energy, exchange-correlation energy, and the classical electrostatic repulsion energy between the ions. For the system to be in the ground state and the correct choice of the functional $n_e$, the total energy must become minimal. Finding the electron density is equivalent to solving the single-particle Kohn-Sham equations [128]:

$$\hat{F}\chi_i = \epsilon_i \chi_i(\vec{r}) \tag{3.4}$$

where $n_e = \sum_i |\chi_i|^2$. Here, $\epsilon_i$ and $\chi_i$ are the Kohn-Sham eigenstates and eigenvalues, respectively. The Kohn-Sham operator $\hat{F}$ is given by

$$\hat{F} = -\frac{1}{2}\nabla^2 + V_{\text{ext}}(\vec{r}) + V_{\text{XC}}(\vec{r}) + \int \frac{n_e(\vec{r'})}{|\vec{r} - \vec{r'}|} \mathrm{d}\vec{r} \tag{3.5}$$

where $V_{\text{ext}}$ and $V_{\text{XC}}$ are the external ionic and the exchange correlation potential, respectively. In practice, the ground state is obtained by solving in a self-consistent cycle the Kohn-Sham equations. The accuracy of the obtained solution depends critically on the used approximation for the exchange-correlation potential.

The adsorption geometry of molecules on metals was determined by DFT calculations implemented in the quickstep code of CP2K [129]. The used exchange-correlation was based on the Perdew-Burke-Ernzerhof functional [130]. The Cu(111) and Au(111) surfaces were modeled by a periodic slab of five and six layers, respectively with the three bottom layers being fixed at their bulk position during relaxation. By exploring the potential energy surface for several initial positions, the preferred adsorption geometry was obtained.

### 3.6.2 Elastic scattering quantum chemistry

Following on from the previous Section, the obtained adsorption geometry is the starting point for the image calculation of STM/STS measurements of a single molecule. If the tip is modeled beyond a simple point-like completely symmetric Tersoff-Hamann approach (see Section 2.1), the arising quantum mechanical interactions between the tip and sample are complex. One sophisticated approach to address the electronic properties of this system is based on the elastic scattering quantum chemistry (ESQC) code as it takes the full geometry of tip, molecule, and substrate into account. In the case of hexacene adsorbed on Au(111), tip and substrate were both modeled by six layers of Au atoms with the former being arranged in a pyramidal shape.

The employed ESQC code was developed by P. Sautet and C. Joachim [131–133]. Unlike many other simple methods for image calculations, the tunneling from one electrode to another is treated as scattering problem for a single-electron Hamiltonian. The system is formally divided into different parts, where the electrodes are modeled periodically by identical layers while the molecular region (including tip apex and tunneling gap) is the one layer which breaks the translational symmetry. If this central part is first neglected, the asymptotic electron states for each of the two electrodes can be calculated by taking the chemical nature of all atoms into account [134]. As a next step, the elastic scattering of those states at the molecular region is addressed in a single-particle approximation. The corresponding scattering matrix is calculated by including the spatial position and chemical structure of all atoms in the molecular region. The quantum chemistry interactions can be constructed by tight-binding, extended Hückel, or Hartree-Fock theory. Finally and very similar to Equation 2.7, the tunneling current $I$ for the junction at a given bias is computed via the Landauer formula [64]

$$I = \frac{4\pi e}{\hbar} \int_{-\infty}^{+\infty} T(E)[f_s(E) - f_t(E - eV)]\, \mathrm{d}E \tag{3.6}$$

Here, $f_s$ and $f_t$ are again the Fermi functions for each electrode. While $T(E)$ is the transmission function as obtained by numerical solving the scattering problem for the in- and outgoing electron states between both electrodes.

A two-dimensional map is calculated by moving the tip over the surface and just alternating the molecular region of the system accordingly. A constant-current tip trajectory can be used to obtain an image for the topography as well as for the differential conductance maps for the molecular resonances.

# 4 Tetracene formation on Cu(111)

*The work presented in this Chapter is centered around the deoxygenation as novel surface reaction and has been published as article in the peer-reviewed journal ACS Nano. Parts of the text and figures are reproduced from reference [119] with permission from the American Chemical Society.*

In this Chapter, the surface-assisted reduction of epoxyacenes to obtain the corresponding acenes on a metallic surface is introduced. This novel surface reaction is demonstrated by depositing molecules with two epoxy groups at the terminal rings (Tn2O) and inducing their deoxygenation to form genuine tetracene on Cu(111). The precursors are a mixture of two diastereomers with the epoxy groups in either *syn* or *anti* configuration as depicted in Figure 4.1. The on-surface reaction is achieved by STM tip-induced manipulation as well as by thermal activation and can be conclusively demonstrated by means of AFM with atomic resolution. In particular, the adsorption geometry of precursors and the actual nature of the intermediate and reaction product can be drawn on solid grounds by using this high-resolution imaging technique. All AFM measurements were acquired in the frequency-modulation mode at constant-height with a bias $V = 0\,\mathrm{V}$ and an oscillation amplitude of $\sim 0.5\,\text{Å} = 50\,\mathrm{pm}$.

Designing precursors with epoxy groups at the terminal rings of their molecular backbone has a definite influence on their geometry and electronic structure compared to tetracene. First, the four oxygen-bridged carbon atoms are $sp^3$-hybridized leading to a pronounced non-planar structure in gas-phase. Second, the largest $sp^2$-hybridized system of carbon atoms in the *syn*/*anti*-Tn2O is limited to the two central benzene rings leading to a larger HOMO-LUMO gap and a higher stability compared to the four-ring system of genuine tetracene. In solution chemistry, the reduction of epoxy precursors is a nontrivial transformation which requires the use of reducing reagents [135–138].

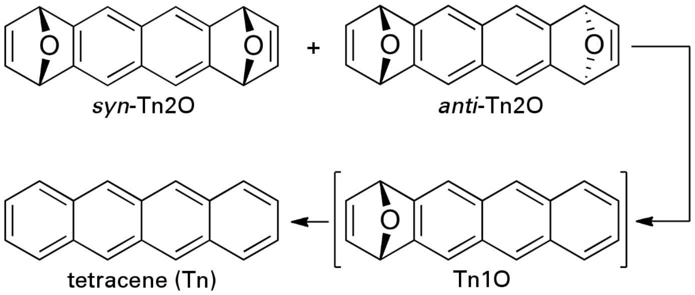

**Figure 4.1 – Surface-assisted reduction.** A mixture of diepoxytetracenes is reduced on a metallic surface via the intermediate epoxytetracene to form genuine tetracene.

## 4.1 Imaging of the precursors

The molecular precursors were investigated on a Cu(111) surface with islands of bilayer NaCl, referred to as NaCl(2ML). Since the mixture of the two diastereomers was deposited onto the sample kept at a temperature of approximately 10 K, the sticking coefficient for the adsorption of the tetracene precursors *syn/anti*-Tn2O on the bare Cu(111) and NaCl(2ML) was close to one. Therefore, both diastereomers were present on the surface and could be resolved as single molecules on the metal *and* the ultrathin insulating layer as shown in the STM image in Figure 4.2. In addition, this scan shows round depressions which are identified to be CO molecules.

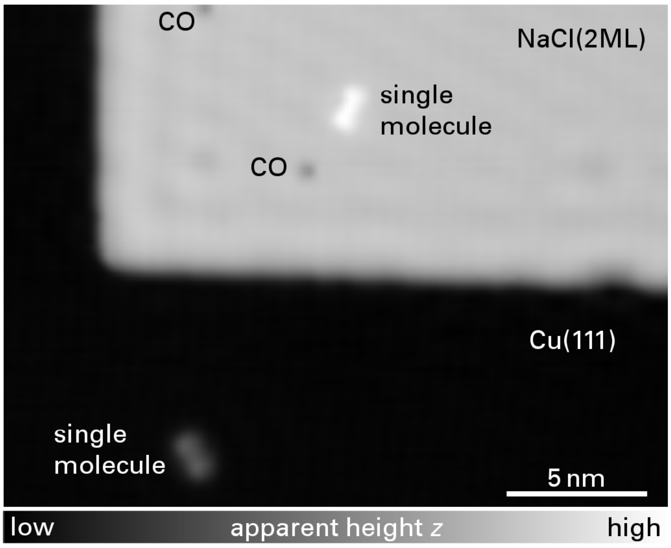

**Figure 4.2 – STM overview image after molecule deposition.** Single molecules appear as protrusions (bright) while CO molecules are imaged as depressions (dim). Constant-current scan with a metal-terminated tip acquired at +0.1 V and 2 pA.

High-resolution images were obtained in the following way: Isolated molecules were first localized with STM scans at constant-current since this mode allows a faster operation mode. High-resolution and slow speed AFM measurements with a functionalized tip at constant height were performed at the last step. Starting from a certain set point, the tip was gradually brought closer to the surface until the short-range, and repulsive forces of the molecule could be sensed via the recording of $\Delta f$-signal. Due to the pronounced non-planar adsorption geometry (see top row in Figure 4.3), the outer upright segments of the molecules interacted strongly with the tip. Thus, these parts showed a less negative frequency shift than the faint contribution of the two inner planar benzene rings. With decreasing tip height, the strong repulsive contrast of the outer parts became even more pronounced in the raw AFM images (see Section A.2 in the Appendix) before the more closely to the surface adsorbed benzene rings could be fully resolved. Figure 4.3 presents the Laplace-filtered $\Delta f$ images with enhanced contrast. In particular, panels a and b display typical images obtained for *syn*-isomer on bare Cu(111) and NaCl(2ML), respectively. It is evident that they are characterized by their symmetric shape and reveal additional details at the center of their images due to the applied Laplace-filtering. Apparently, there is no significant difference between the molecular structures on Cu(111) and NaCl(2ML) and the images show that two upright CH groups are pointing toward the tip on either side of the molecules. All the imaged *syn*-isomers featured this particular configuration and no molecule with both oxygens pointing away from the surface was observed. One can conclude that the preferred adsorption geometry coincides with the oxygen-rich side of the molecules facing the surface. On the contrary, adsorbed *anti*-isomers featured always one protruding oxygen atom. This geometry is illustrated by the DFT-based calculated model in Figure 4.3d. The resulting Laplace-filtered AFM images were identified by two dissimilar sides as this oxygen atom leads to a different contrast which is shown in Figure 4.3e for *anti*-Tn2O on NaCl(2ML).

When constant-height AFM measurements with two different tip height domains were employed, the molecular structure, as well as the underlying atomic lattice could be resolved. This technique was used to determine the adsorption site of the *syn*-isomer on NaCl(2ML). The experimental gray-scale image in Figure 4.3e corresponds to the unfiltered but distortion corrected $\Delta f$ data and features a sharp edge where the tip-height was switched from low (lattice) to high (molecule). Since the Cl atoms give a stronger repulsive (bright) contrast if imaged with a CO-functionalized tip [139], the atomic structure of the NaCl lattice could be superimposed to identify the adsorption position. A laterally displaced ball-and-stick model of the free molecule illustrates that the electronegative oxygen atoms are in close proximity to the Na atoms. This observation further rationalizes the experimental images of 4.3a and 4.3b, since the oxygen-rich side of the molecule is indeed facing the surface.

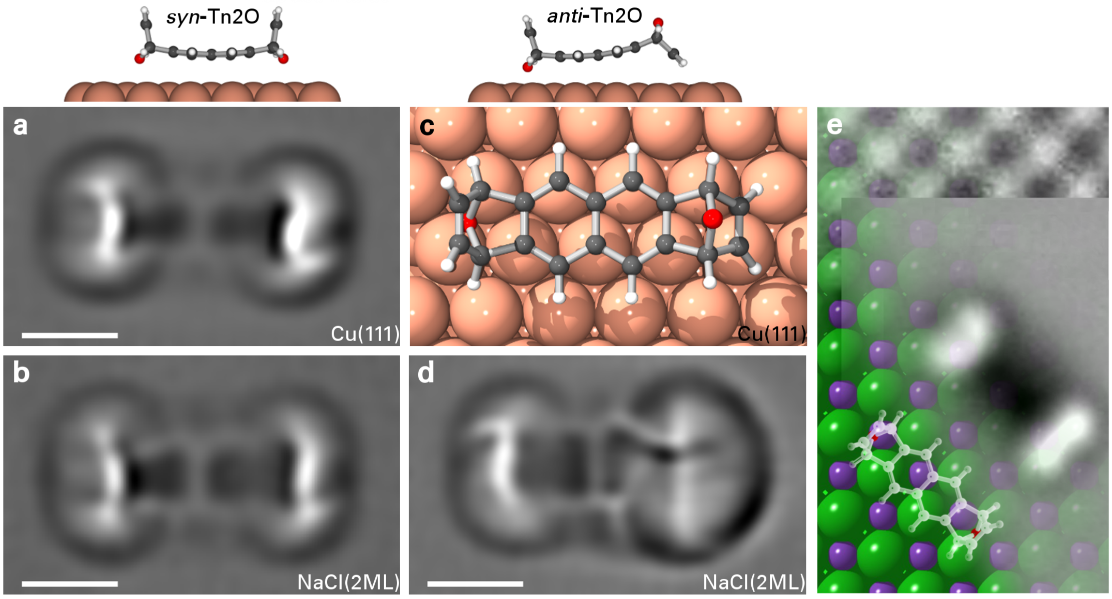

**Figure 4.3 – Tetracene precursors on Cu(111) and NaCl(2ML).** DFT-based adsorption geometry on Cu(111) is shown in the top row. **(a,b):** Laplace-filtered AFM images of *syn*-isomer on bare Cu(111) and NaCl(2ML), respectively. **(c):** Ball-and-stick-model of *anti*-isomer's geometry as calculated for this molecule after full relaxation on a Cu(111) surface. A corresponding experimental AFM image is given in Figure A.2 in the Appendix. **(d):** Laplace-filtered image of *anti*-isomer on NaCl(2ML) with different contrast on the right-hand side due to protruding oxygen. **(e):** Observed adsorption site of a *syn*-isomer on NaCl(2ML). Experimental gray-scale AFM data (unfiltered) and modeling are superimposed. All scale bars refer to 5 Å.

## 4.2 On-surface conversion

### 4.2.1 Single-molecule chemistry

One of the outstanding features of STM is the fact that it cannot only be used to image but also to manipulate single atoms and molecules. After the first demonstration by D. Eigler and his group at IBM Research—Almaden [140, 141], many research groups followed this path. Most notably, by applying voltage pulses with the tip of an STM, conformational changes [142, 143] and chemical reactions [40, 41, 144–146] can be induced in a molecule. Obviously, the fact if a reaction can be successfully triggered by STM relies on some parameters. For instance, the activation energy of the desired reaction needs to be in tune with the interaction between tip, adsorbate, and surface. If the binding of the adsorbate to the surface is too low, voltage pulses will lead to a displacement event of the molecule rather than a chemical reaction [147]. Additionally, if the interaction between tip and adsorbate is increased beyond a certain threshold, the molecule will be transferred to the tip before a reaction can be observed.

Due to the larger coupling of single precursors directly on Cu(111) compared to the adsorption with the ultrathin NaCl(2ML) in between, the controlled manipulation

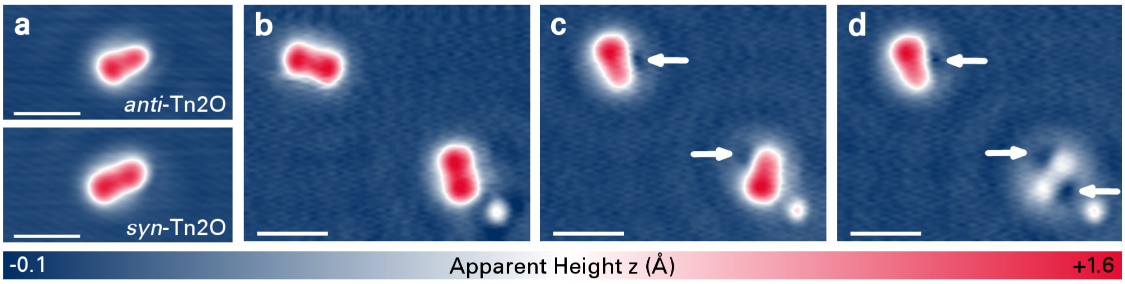

**Figure 4.4 – Constant-current STM images acquired with a metal-terminated tip on Cu(111). (a):** Images of a single *anti*-Tn2O and a *syn*-Tn2O molecule acquired at +0.1 V and 2 pA. **(b-d):** Set of images (+0.1 V and 0.5 pA) which illustrate the tip-induced molecular conversion. **(b):** Two *syn*-Tn2O molecules imaged as protrusions with a dumbbell shape. In addition, a defect is visible in the bottom right corner. **(c):** The resulting intermediates Tn1O after STM imaging at a bias of +2.2 V are shown. **(d):** Upon application of another higher-voltage scan at +2.6 V to the molecule on the lower part, the final conversion to tetracene was obtained. All scale bars refer to 20 Å.

of such small molecules proved to be more feasible on the metal. Therefore, all the observations described in the following were obtained on Cu(111).

First, the unreacted molecules were imaged by STM with a metal-terminated tip at a low bias of 0.1 V. As one can see in Figure 4.4a, both isomers appear as dumbbell-shaped protrusions; however, the *anti*-isomer features two dissimilar sides. These STM images could be correlated to the AFM images of both isomers; therefore, the initial molecules were unambiguously characterized. A chemical conversion was then already obtained by constant-current STM imaging with a metal-terminated tip at a higher bias voltage. The corresponding threshold for any first tip-induced reaction was found to be at 2.2 V. This value was derived by many subsequent STM scans at gradually increasing bias (starting value = 0.1 V, step size = 0.05 V) and at a constant current of 0.5 pA for ten different precursor molecules. While scanning, a sudden contrast change of the molecular topography indicated the successful conversion. This observation could be confirmed by a subsequent STM scan at low bias of 0.1 V. In the case of *syn*-isomers, on-surface reactions were usually triggered in a two-step process via the formation of an intermediate. Figure 4.4b shows two *syn*-isomers before manipulation. After a tip-induced reaction at 2.2 V, both molecules appear flattened on one side as presented in Figure 4.4c. Additionally, very shallow depressions close-by can be recognized (see arrows). A second manipulation step applied to the lower intermediate lead to an additional faint indentation, and the resulting molecule appears distinctly smaller in apparent height than the precursor. AFM imaging with a CO-terminated tip at constant height was then performed to characterize both the intermediate as well as the final product of the reaction.

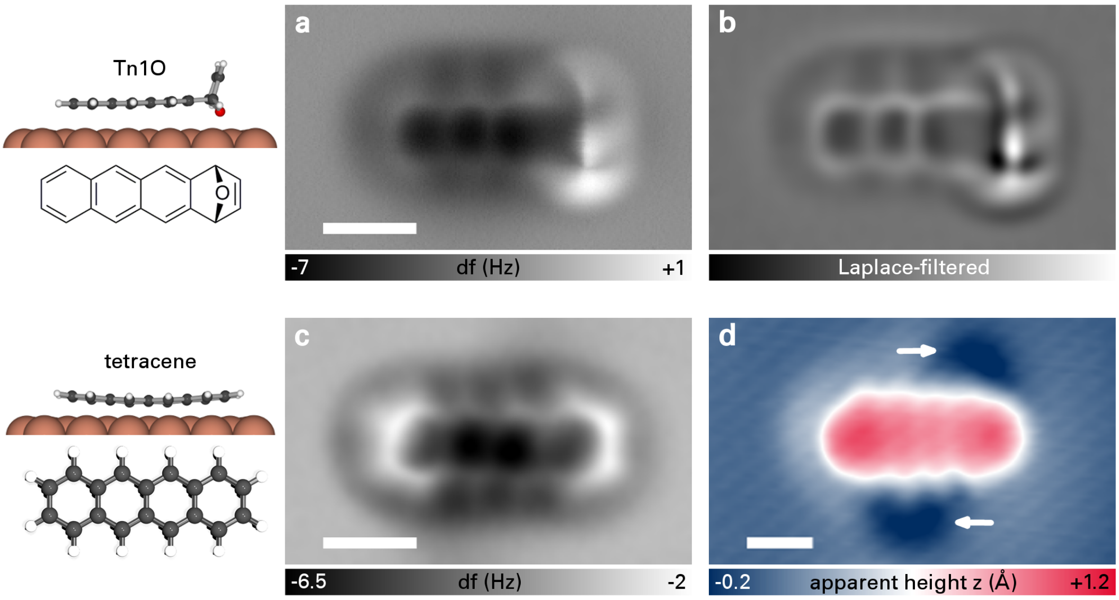

**Figure 4.5 – Intermediate Tn1O and final product tetracene.** Both were obtained after tip-induced conversion of a *syn*-Tn2O molecule on Cu(111). **(a,b):** Constant-height AFM image and Laplace-filtered data of the intermediate Tn1O after the first oxygen detachment. **(c):** Constant-height AFM image of the resulting tetracene molecule after complete deoxygenation. **(d):** Constant-current STM image (+0.1 V, 2 pA) of the same molecule. The arrows point to close-by shallow depressions and suggest the presence of atomic oxygen. Scale bars refer to 5 Å.

Panels a and b of Figure 4.5 show the resulting AFM data after the first manipulation event and demonstrates that one oxygen atom was separated by two C-O bond cleavages, i.e. the molecule Tn1O. Tip-induced excitation of the molecule was followed by energy dissipation to break bonds, and a partial planarization of the remaining molecule took place in the presence of a surface. Hence, an additional benzene ring becomes visible in the AFM image. After the second manipulation step, the molecule was completely planar and an aromatic backbone of four linearly fused benzene rings could be resolved, as indicated in the unfiltered Figure 4.5c. This image is in accordance with the AFM images of the previously investigated pentacene on Cu(111) [35]. In particular, it shows the same apparent feature that the outer rings are imaged more repulsive (brighter) than the two inner ones. Therefore, the structure of the final product of the reaction is unambiguously determined to be tetracene. Further STM images with a CO-terminated tip (see Figure 4.5d) revealed that the detached oxygen atoms were situated near to the newly formed tetracene molecule. They were imaged as indentations which are only observed on the surface after a successful tip-induced reaction. One should emphasize the fact that tip-induced reactions are frequently applied for single $\sigma$-bonds[1]; however, that the dissociation of oxygen atoms from a carbon backbone via two bond breaks has not been reported before.

---

[1] For instance, tip-induced cleavage of a carbon-halogen bond [40, 41, 145].

It is worth noting that applying the same manipulation protocol to *anti*-Tn2O did not lead to the full conversion to tetracene. After the first successful reduction step, AFM imaging showed that the intermediate molecules Tn1O could be identified but with the remaining oxygen atom pointing away from the metal surface. If these intermediates were scanned at a higher voltage at up to 3.0 V, the second reduction could not be obtained in the experiment. Even if the rate of single-molecule conversions may also depend on the particular tip shape, this observation still suggests that the tip-induced cleavage depends on the orientation of the oxygen with respect to the underlying substrate. Apparently, a larger O-Cu interaction is favorable for a tip-induced on-surface reduction. Accordingly, all successfully triggered reactions were accompanied by a displacement of the molecule while the separated oxygen atoms remained close to their presumed adsorption site.

### 4.2.2 Thermally induced reaction

To extend this single-molecule reaction to a general preparation method, a thermally induced conversion was also investigated. The sample with a low molecule coverage was transferred out of the STM/AFM chamber and annealed at a temperature of 390 K for 5 min. Then it was cooled again and transferred back into the microscope chamber without breaking the UHV conditions at any time. After heating and due to the low coverage, the terraces were mostly empty and molecules assembled solely at Cu step edges. As a matter of fact, an exemplary overview image after annealing is given in Figure 3.7 in Section 3.3. Panels a-c of Figure 4.6 illustrate the fact that all atomically resolved AFM images showed the presence of tetracene on the surface, and no precursors could be observed anymore. More importantly, no molecules with one oxygen atom still attached were found in the experiment. This implies that the temperature activated reaction took place at a high rate and regardless of the oxygen orientation of the precursors. Nevertheless, the latter observation is not necessarily a proof that molecules of *anti*-Tn2O react in the same way as *syn*-isomers. After the first reduction step, the resulting intermediate Tn1O may still have considerably different activation barriers to form tetracene depending on the orientation of the remaining oxygen. Upon annealing, molecules diffuse on the surface to more reactive step edges/kink sites or may even switch their oxygen configuration and are then fully reduced due to the enhanced coupling to the Cu; however, the true reaction path remains elusive.

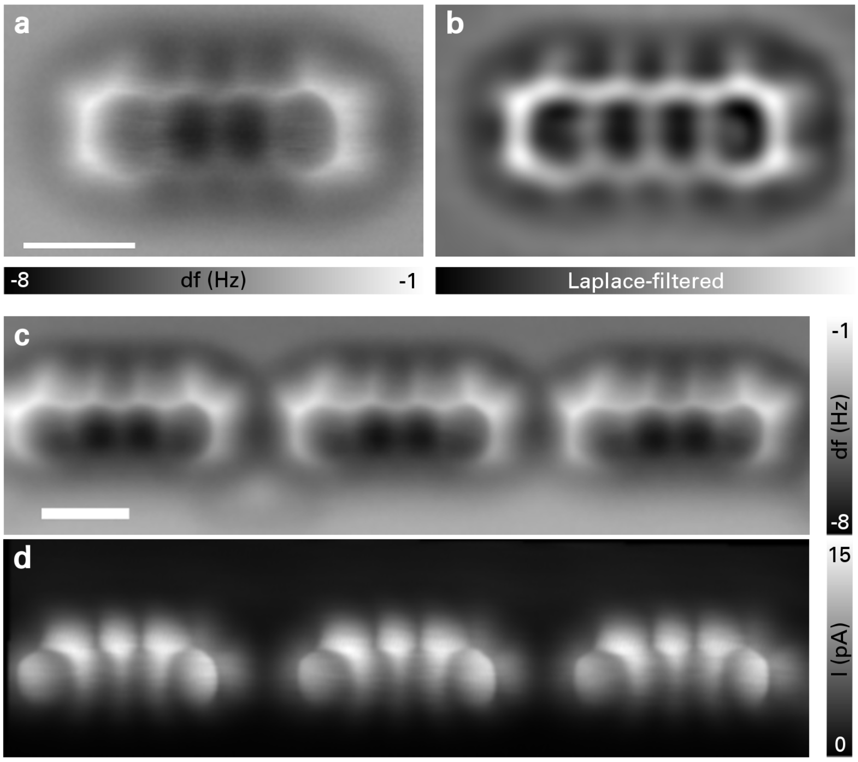

**Figure 4.6 – Product of the on-surface reduction on Cu(111). (a,b):** AFM and its Laplace-filtered image of an on-surface produced tetracene. **(c):** AFM image of three tetracene molecules assembled along a step edge. **(d):** By repeating the same scan with a minimal bias of $V = 1$ mV, the tunneling current can be recorded. All images were acquired at a constant height and with a CO-terminated tip. All scale bars refer to 5 Å.

Finally, the obtained AFM images of the on-surface generated tetracene are of the highest quality since even the bonds between carbon and hydrogen atoms can be recognized in Figure 4.6a and b. Therefore, one can assume that the adopted adsorption geometry on Cu(111) is very similar to the one of pentacene which has been intensively studied before [148]. The high interaction with the metal leads to a small adsorption height and parabolic trough geometry along the molecular long axis as also found by DFT modeling for tetracene (see Figure 4.5). As a result, the electronic structure of the molecules is strongly influenced by the surface and investigation of the molecular orbitals is difficult. If the adsorbed tetracenes are imaged at a minimal bias of $V = 1$ mV, the obtained STM images show pronounced sub-molecular features as demonstrated by Figure 4.6d. This observation is a strong hint that the tunneling electrons can access a molecular resonance even though the applied bias is almost zero. In other words, one molecular resonance is centered around the Fermi level $E_F$ of the unpolarized (zero-bias) tunnel junction which is usually related to a strong coupling and partial charge transfer between substrate and molecule [88].

## 4.3 Discussion

In summary, this Chapter demonstrates the on-surface reduction of a diepoxyacene to produce the corresponding acene on Cu(111). Notably, thermally induced experiments allow one to induce the tetracene formation in a very efficient manner regardless of the starting diastereomer. Single molecule experiments show a different behavior of *syn* and *anti* diastereomeric diepoxyacenes which suggests that the O-Cu interaction lowers the activation barrier and is crucial for the deoxygenation. It is clear that the role of the metallic surface is not limited to the deoxygenation but extends to the planarization after bond cleavage. Therefore, the shown reaction leads essentially to the extension of an aromatic system from two to four rings on a metallic surface. Given the various strategies to obtain acenes from different precursors [149, 150], other approaches may also work on the surface effectively. The strong electronic interaction between the generated molecules and the underlying copper substrate makes subsequent investigations of the electronic structure at this interface difficult. Therefore, it is desirable to extend the acene formation to less reactive surfaces.

# 5 Molecular self-assembly on Au(111)

*The work presented in this Chapter is centered around the observed molecular ordering of the precursors as well as of the generated acenes and has been published as article in the peer-reviewed Journal of Physical Chemistry C. Parts of the text and figures are reproduced from reference [151] with permission from the American Chemical Society.*

In this Chapter, the experimental investigation on the surface-assisted formation of short acenes is extended to the Au(111) surface. Since this substrate is considered to be less reactive than the copper substrate [152], this shows that the reaction is more widely applicable. In contrast to the experiment presented in the previous Chapter, all the compounds were deposited onto the surface kept at *room temperature* instead of 10 K. Upon adsorption, the thermal energy of the substrate translates into kinetic energy of the molecules. At room temperature, this value is typically large enough to overcome the diffusion barrier of the gold surface. Hence, the molecules can move and explore preferred surface sites which are determined by molecule-substrate interactions and can also self-assemble into supramolecular structures due to molecule-molecule interactions [153]. Since the STM measurements were always carried out at a temperature of 5 K, the dynamics of the surface diffusion could not be captured in the experiments; however, the obtained overview images showed the molecules at positions which are energetically favorable. STM investigations are particularly suited to study molecular self-assembly since a *real-space* image is obtained which allows one to shed light on the influence of functional groups for intramolecular bonding and the molecule-substrate interactions [154, 155].

The focus of this Chapter is on the role of the incorporated oxygen bridges in the molecular backbone at the terminal rings. In particular, the aim is to describe the distinct influence of this moiety on the molecular self-assembly of two different epoxyacenes.

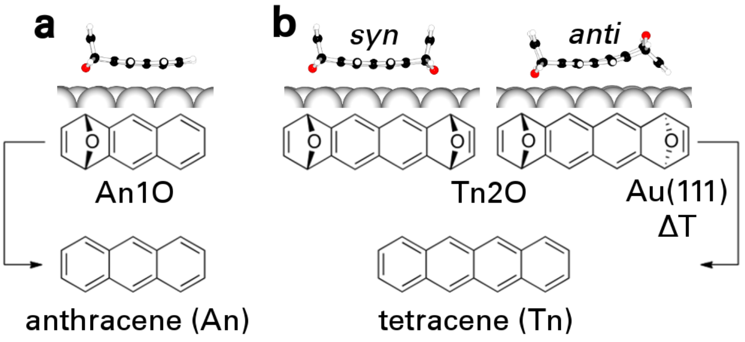

**Figure 5.1 – Chemical structure, adsorption geometry, and reduced form of the investigated molecules on Au(111). (a):** An1O molecule which is reduced to anthracene upon annealing. **(b):** The two diastereomers of Tn2O and tetracene as a product of on-surface deoxygenation. The shown adsorption geometries were derived by DFT.

First, the anthracene-derivative An1O (see Figure 5.1) with one epoxy group at the terminal ring only was studied. This system allows the detailed understanding of the adsorption geometry and modeling of observed nanostructures. Once this system is comprehensively described, the experimental observations for the tetracene-derivatives Tn2O are addressed. Obviously, the presence of two epoxy groups in either *syn* or *anti*-configuration leads to a more complex system.

## 5.1 Formation of anthracene trimers

### 5.1.1 Self-assembly of precursors

The An1O molecules (Figure 5.1a) were deposited with low surface coverage onto the Au(111) surface kept at room temperature. STM images showed that molecules on terraces were isolated or formed triangular-shaped nanoassemblies with two different chiral motifs $\delta$ and $\lambda$[1] as presented in Figure 5.2a. The former could be recognized by a teardrop-shaped topography which corresponds to a non-planar adsorption geometry. DFT calculations proved that single molecules preferably adsorb with the oxygen-atom facing the surface, thus two C-H groups are upright and give rise to a distinctly enhanced apparent height at one side of the molecule as visible in the close-up image of Figure 5.2b. The triangular nanostructures were formed by the self-assembly of three An1O molecules with the non-planar ends coming close to each other. This geometry was modeled by DFT calculations to prove that the relaxed structure of three molecules on Au(111) as presented in Figure 5.2c indeed corresponds to an energetically favorable structure on the surface. The calculated geometry suggests that the trimers are stabilized by three hydrogen bonds formed by intermolecular interactions

---

[1] Both motifs are mirror-symmetric, thus called enantiomers.

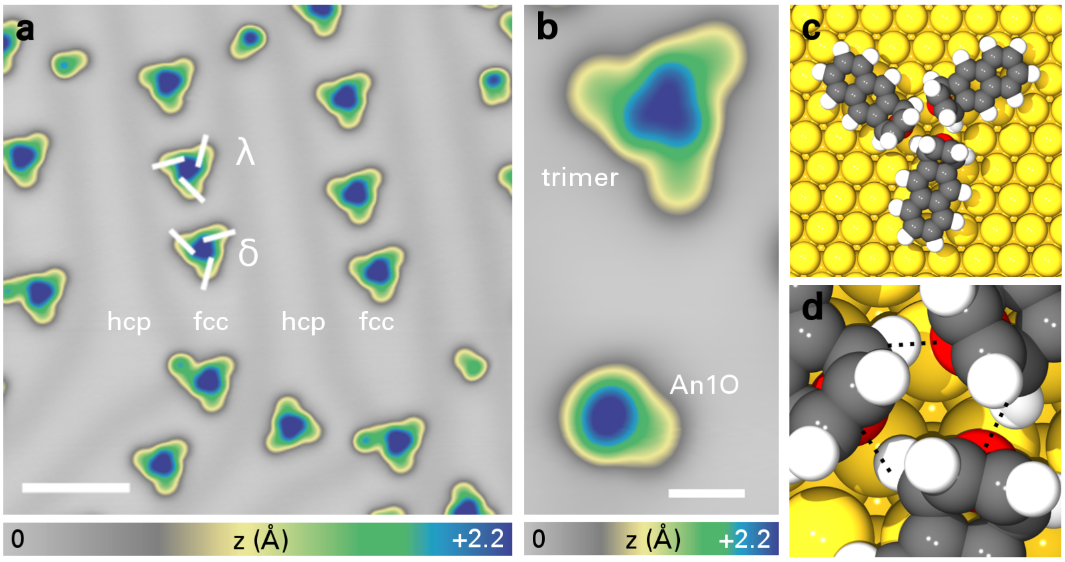

**Figure 5.2 – STM image of An1O molecules as deposited on Au(111) kept at room temperature.** **(a):** Overview STM image acquired at 0.5 V and 80 pA. Two symmetric mirror forms of trimers, as well as fcc and hcp domains of the surface reconstruction, are visible. Scale bar refers to 5 nm. **(b):** STM image ($V$ = 0.1 V, $I$ = 100 pA, scale bar equal to 1 nm) of one isolated An1O molecules as well as one An1O trimer. **(c):** DFT-based modeling of the trimers. **(d):** Stabilization based on hydrogen bonds between oxygen and hydrogen as indicated by dashed lines.

between electronegative oxygen and hydrogen at the sp$^3$-hybridized bridgehead carbon atom as shown in the Figure 5.2d.

### 5.1.2 Chemical conversion

As a next step, thermally induced experiments were performed to investigate the observed structures upon induced deoxygenation. Figure 5.3 shows the different adsorbed molecular species after annealing. Investigations of the substrate after heating at 340 K allows the direct comparison between isolated An1O and anthracene molecules as the reduction was not yet achieved at a very high rate. Precursors were identified by their characteristic teardrop shape while on-surface produced anthracene appeared flat with a clearly reduced apparent height (see the color scale in Figure 5.3a). Similar to the precursors, anthracene molecules were either found to be isolated or in a trimer assembly. Thus, Figure 5.3a shows all frequently observed motifs for this preparation in one close-up STM image. By superimposing the molecular structures, it becomes evident (see Figure 5.3b) how three anthracenes are aligned in such a triangular-shaped assembly. However, it is not clear how this structure is stabilized since the interaction between hydrocarbon molecules without any functional groups should not favor directed intermolecular forces but rather be based on non-selective van der Waals force [153]. By considering possible intermolecular interactions which can be pertinent

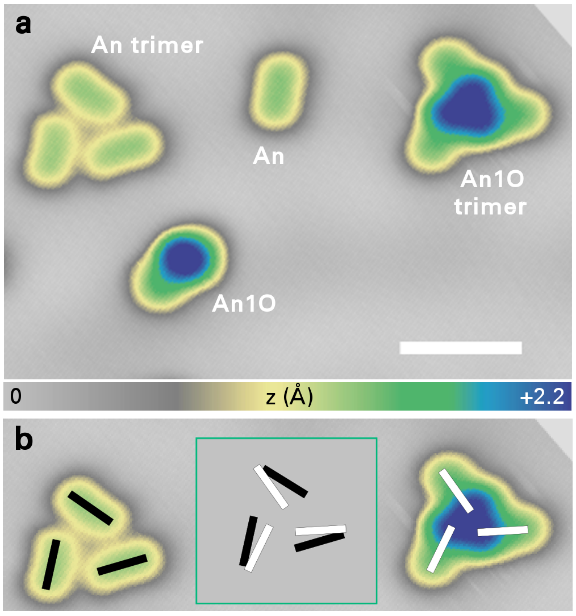

**Figure 5.3 – STM image of precursors and anthracene on Au(111) after annealing a An1O-covered Au(111) surface at 340 K. (a):** Close-up STM image ($V$ = 0.1 V, 80 pA, scale bar equal to 2 nm) showing prevailing structures observed on the surface. **(b):** By superimposing the molecular long axis of single molecules onto the trimers observed in (a), the triangular nanostructures are elucidated. Both trimers are overlaid in the central box to show the slightly different molecular orientation within those two trimers.

on metal surfaces [156] and bearing in mind the induced surface reaction, it seems likely that this kind of assembly of three anthracene molecule is supported by the byproduct of the on-surface reduction, i.e. cleaved oxygen atoms. First, the molecules adsorb in such a way that all three oxygen atoms face the surface and are positioned at the center of the trimer. Upon thermally induced deoxygenation, the three cleaved oxygen atoms remain presumably close to the initial adsorption position and stabilize the anthracene molecules. Resolving single oxygen atoms at the center of the trimer assembly is difficult by STM; however, closer inspection of the constant-current images shows that the molecules within those trimers appear slightly bent, e.g. by comparing the isolated anthracene and the bottom left molecule within the trimer assembly (Figure 5.3a) makes a slight difference evident. This observation may be a hint that the proximity of the atomic oxygen has a distinct influence on the electronic structure of anthracene and causes the small distortion in the STM image. After annealing the An1O-covered sample at 390 K, no precursors were observed anymore but isolated anthracene and trimers only.

While the focus of this Chapter was not on the electronic structure, it is still interesting to note that STS measurements of single molecules were challenging to obtain and frequently led to a lateral manipulation as soon as a bias larger than 1 V was reached. However, trimer structures proofed to be more stable and spectra at the center of both unreacted and reacted trimers could be measured. Figure 5.4 shows that three self-assembled anthracene molecules have a very strong and particularly broad resonance at around 2.4 V which stems from the spatial overlap of three unoccupied molecular state resonances. In contrast, there is only a small increase in the differential conductance at the center of for three unreacted An1O molecules compared to the bare metal substrate.

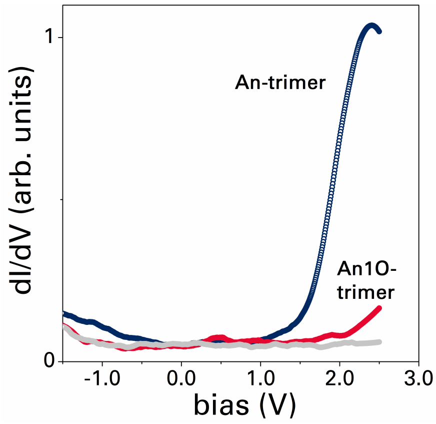

**Figure 5.4 – STS measurements of trimers.** The corresponding STM image is given in Figure 5.3a. The tip was stabilized at the center of an An-trimer (blue curve) as well as at the center of an An1O-trimer (red curve). The tip-sample height was stabilized at 140 pA and 2 V for both cases. The gray curve shows a background spectrum.

## 5.2 Supramolecular networks of tetracene

### 5.2.1 Self-assembly of the precursors

The Tn2O molecules were deposited on Au(111) with a slightly higher coverage than in the case of An1O; however, the important experimental observations for the as-prepared surface were in line. Single Tn2O molecules also adsorb with a non-planar geometry and were accordingly imaged as dumbbell-shaped protrusion as presented in Figure 5.5 and in agreement with STM images[2] on Cu(111). Similar to the case of An1O, self-assembly patterns were observed which are however not limited to isolated nanostructures. This fact can be attributed to the higher coverage and the presence of two moieties that favor directed interaction on both ends of the molecule. The majority of the molecules were stabilized in assemblies with two or three molecules coming close to each other as indicated by the arrows in Figure 5.5a. Notably, the dimeric structure features an off-center arrangement and the trimeric structure is equivalent to the triangular nanostructure observed for An1O. Further, one can find hexagonal motifs which are composed of six Tn2O molecules forming trimeric or dimeric patterns with an inner hexagon of six Tn2O molecules. Figure 5.5b singles two mirror symmetric examples out where individual molecules are marked with white bars. Large-scale scans (Figure 5.5c) showed that one could occasionally find honeycomb domains formed by several adjacent hexagons to form an open-porous 2D network. Hence, a simple selective and directed hydrogen bond interaction gives rise to a complex and intriguing self-assembled network which is not limited in size by the underlying surface reconstruction. In the field of surface science, there are many examples of supramolecular networks formed by intermolecular bonds between oxygen and hydrogen of neighboring molecules on coinage metal surfaces [157–160]. Since the diffusion barrier is low

---

[2] For comparison, see Figure 4.4a

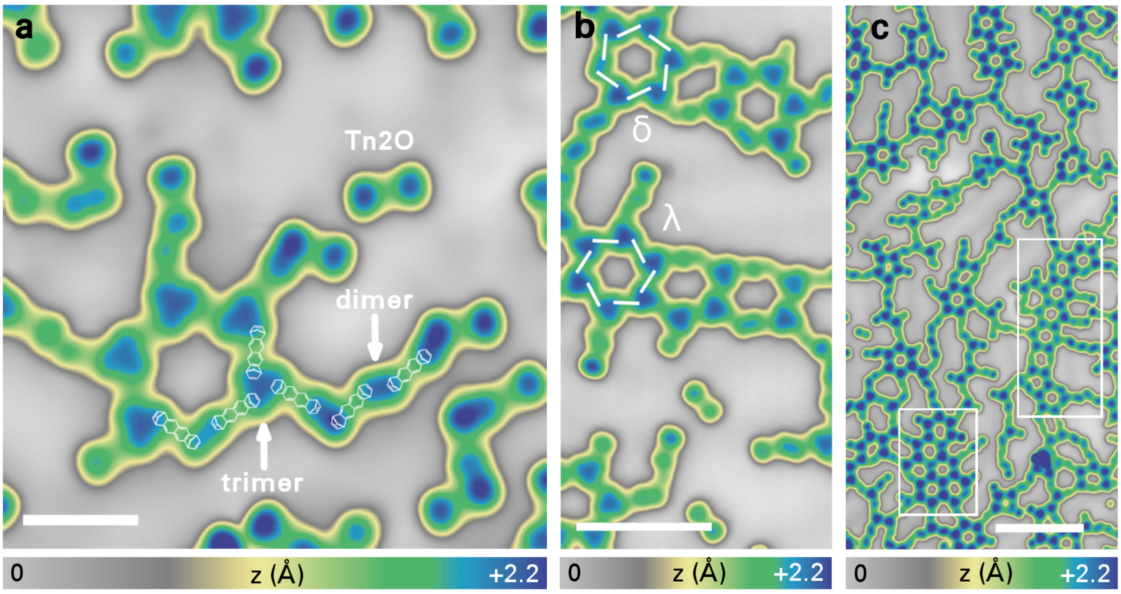

**Figure 5.5 – STM images of Tn2O molecules as deposited onto the Au(111) surface. (a):** STM image acquired at $V = 0.1$ V and $I = 100$ pA showing a single molecule (labeled with Tn2O) as well as self-assembled dimeric and trimeric structures. Scale bar refers to 2 nm.**(b):** STM image ($V = 1$ V, $I = 100$ pA, scale bar equal to 5 nm) showing regular hexagons. **(c):** Large-scale STM image ($V = 1$ V, $I = 100$ pA, scale bar equal to 10 nm) of complex networks including regular honeycomb domains (white frames). This supramolecular network can be interpreted as a Kagome lattice as will be discussed in Figure 5.7.

on such surfaces, hydrogen bonds strongly dominate the molecular assembly despite the fact that the associated force is considered weak [156].

## 5.2.2 Chemical conversion

Thermally induced experiments for Tn2O on Au(111) showed that an annealing temperature similar to the An1O experiments was needed to trigger the on-surface reduction. After heating at 390 K (Figure 5.6), one could not observe any precursors but the reduced form of the molecules only, i.e. tetracene. Similar to the anthracene formation, a successful reaction became apparent by a distinctly different topography of single molecules. Figure 5.6a shows that tetracenes appeared as elongated featureless protrusions if imaged at a bias close to the Fermi level. Furthermore, the STM measurements indicated that isolated molecules had the tendency to be easily dragged by the tip during scanning. One can recognize several imaging artifacts in the Figure 5.6a which correspond to tetracene molecules that suddenly jumped to a different surface position during scanning and hence appear longer or just as fragments. This high surface mobility at cryogenic temperatures was also observed for the on-surface produced anthracene as well as reported in the literature [161] for tetracene on Ag(111) at 8 K. By contrast, molecules in supramolecular assemblies were found to be less prone to STM tip-induced

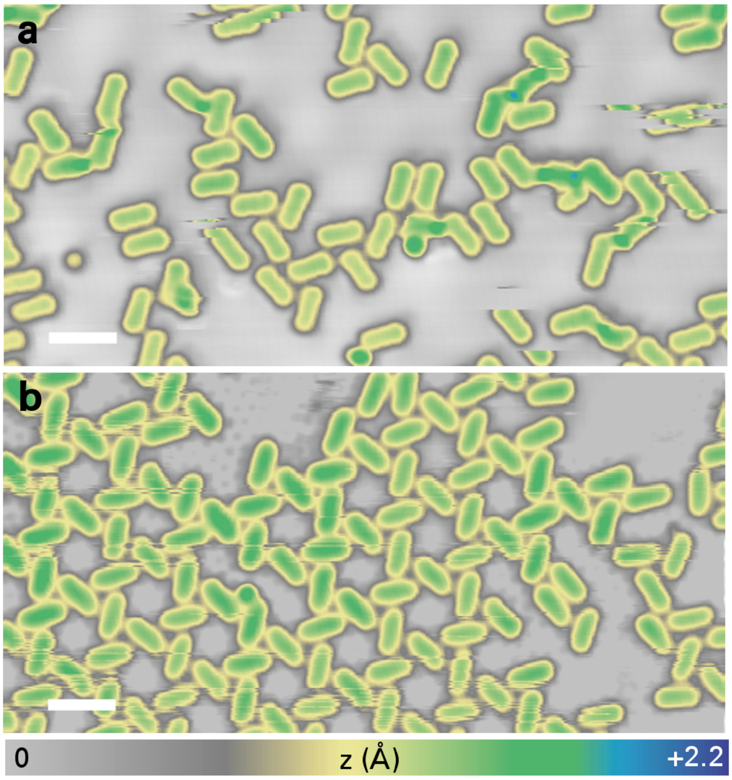

**Figure 5.6 – STM image of tetracene molecules on Au(111) after annealing a Tn2O-covered surface.** **(a):** STM image acquired at $V = +0.1$ V and $I = 80$ pA showing on-surface fabricated tetracene molecules. The used annealing temperature was 390 K. Scale bar refers to 2 nm. **(b):** STM image (1 V, 100 pA, scale bar refers to 2 nm) recorded at another region of the same sample preparation showing ordered structures.

movement and could always be imaged in a stable manner. Notably, scans of large surface areas occasionally showed parts of the surface with well-ordered domains. It is apparent from the detail image in Figure 5.6b that single molecules within this regular lattice display three different adsorption orientations with the same three-fold symmetry as the underlying hexagonal gold lattice. If the center coordinates of single molecules are considered, the spatial distribution of molecules can be described by a Kagome lattice as presented in Figure 5.7a where two hexagons (marked in blue) and two triangles join at each vertex. This kind of self-assembly of linear molecules has been reported in the literature [162, 163] on-surface for simple oligophenylenes functionalized with two nitrile groups which are however clearly ditopic meaning that they feature two distinct binding sites on either side. By contrast, no experimental observation of such assembly for hydrocarbons without any functional group has been presented so far. Performing the control experiment and depositing tetracene directly onto a clean gold sample kept at room temperature led to the observation that no Kagome lattice was observed for the as-prepared surfaces as well as after annealing at 390 K as described in Section A.3 of the Appendix. Therefore, it seems likely that the oxygen separated from the precursors adsorb on the surface as atomic oxygen and stabilize the self-assembly of the acenes. This is supported by the fact that the minimum annealing temperature needed to fully reduce the An1O and Tn2O molecules is just 390 K. Previous studies of chemisorbed atomic oxygen on Au(111) have reported that a sample temperature of about 500 K to 550 K is needed to detect its desorption as molecular oxygen [164, 165].

One can conclude that this regular lattice of tetracene molecules is connected to the self-assembly of precursor molecules and persists even after the thermally-induced reduction. Accordingly, the open-porous networks occasionally observed for as-prepared surface with Tn2O molecules (Figure 5.5c) and first introduced as hexagonal assembly can also be viewed as Kagome lattice by marking the position of single molecules instead of trimeric centers. The result is shown in Figure 5.7b and illustrates that the ordered self-assembly of the Tn2O molecules as well as of their reduced form can be described in an equivalent way by the Kagome lattice (see Figure 5.7c for the ideal two-dimensional lattice) with similar spatial dimensions. A large-scale comparison between both self-assemblies can be seen in panels d and e of Figure 5.7. Thus, the ditopic character of the precursors with two preferred intermolecular hydrogen binding sites lays the basis for the regular pattern for the tetracenes after on-surface reduction.

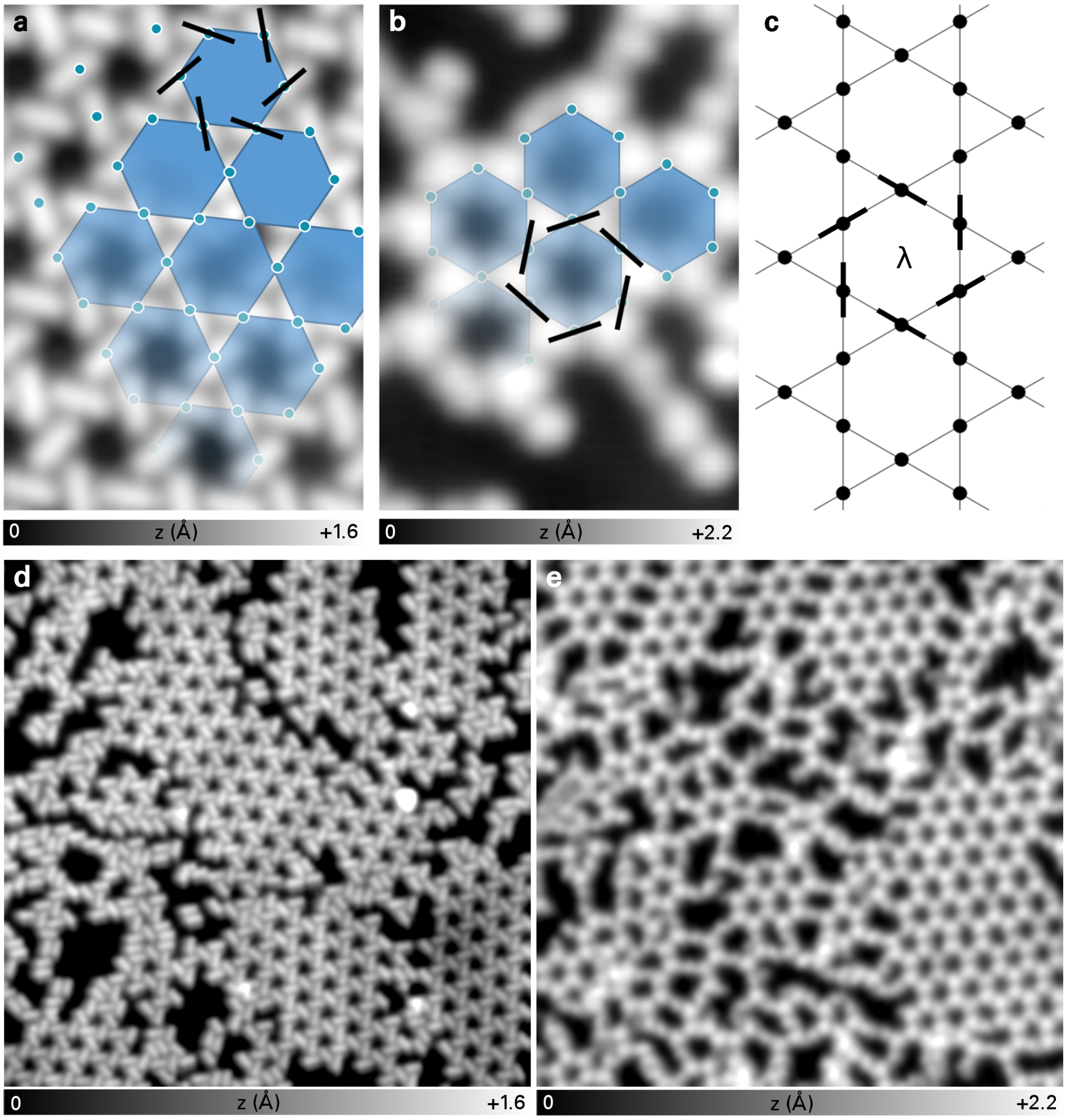

**Figure 5.7 – Supramolecular assemblies described by Kagome lattices.** **(a,b):** Close-up STM images (7.5 nm x 10 nm) of surface-produced tetracenes (a) and as-deposited Tn2O molecules (b). The center position of single molecules (black bars) are marked by blue dots while the blue areas correspond to the hexagons of the Kagome lattice. **(c):** Ideal Kagome lattice where two triangles and two hexagons meet at each lattice point. **(d,e):** Large-scale STM image of surface-produced tetracenes (d) and as-deposited Tn2O molecules (e). Image sizes are 40 nm x 40 nm.

## 5.3 Discussion

In summary, this Chapter shows the nanostructures and networks that are formed by epoxyacenes on Au(111) after room temperature deposition as well as annealing experiments. In the case of the non-symmetrical anthracene derivative An1O with a single terminal epoxy group, trimer nanostructures are favorable assemblies due to the presence of intermolecular hydrogen bonds, as confirmed by DFT calculation. Notably, these trimer structures persist even after the oxygen is cleaved using thermally induced on-surface reduction. The experimental observations for the tetracene derivatives Tn2O with two terminal epoxy groups show a clear overlap. First, the stabilization of trimeric patterns is rediscovered and can be identified as principal building block for well-ordered hexagonal domains. Second, STM images after annealing at 390 K showed the reduced form (tetracene) as the only molecules on the surface. Surprisingly, one occasionally observed also a Kagome lattice formed of tetracenes which one would not expect for symmetric hydrocarbons without functional groups. Bearing in mind the induced on-surface reaction, it seems likely that this well-ordered structure is carried over from the self-organization of the epoxyacenes.

The implications of these results are self-evident. While high-symmetry acenes tend to form densely packed and well-structured layers on coinage metal substrates [161, 166–168], inserting an epoxy group breaks the symmetry and favors directed interaction. Consequently, on-surface generated acenes will not form well-aligned structures but their assembly is governed by the supramolecular ordering of the precursors. Therefore, if the complexity of precursor molecules is further increased to make large acenes accessible via on-surface reduction, disorder at the organic-metal interface should be expected.

# 6 Electronic structure of hexacene stabilized on Au(111)

*Most of the work presented in this Chapter has been published as a communication in the peer-reviewed journal Chemical Communications. Parts of the text and figures are reproduced from reference [120] with permission from the Royal Society of Chemistry.*

In this Chapter, the method of acene formation is applied for the on-surface preparation of unstable hexacene. The isolation and characterization of this molecule has been a long-standing chemical challenge since 1939 [5, 169–171]. Due to its high sensitivity to light and air, it took almost 70 years before a first reproducible synthesis of this compound was reported in 2007. Hexacene quickly undergoes dimerization in solution and could be stabilized in a poly(methyl methacrylate) matrix for 12 h only until it was slowly oxidized by diffusing molecular oxygen [172]. In the corresponding work from D. Neckers et al., hexacene was photochemically generated from a diketone precursor by the expulsion of two CO molecules. The same approach was used by the group of H. Bettinger at the University of Tübingen to obtain hexacene in a solid argon matrix [17] which allowed absorption spectra measurements. Recently, Chow and coworker reported the properties of hexacene crystals obtained from a monoketone precursor in 2012 by thermal expulsion of one CO molecule [16]. They found that the solid-state phase of hexacene has a larger stability and could be stored in the dark in air; presumably because the oxidation is limited to the surface of the crystal.

Nevertheless, no vacuum-processable strategy towards hexacene on surfaces has been presented so far. By designing air-stable epoxy precursors Hn3O (see Figure 6.1a), the surface-assisted reduction can push the boundaries set by stability and allow single molecule investigations for the first time. Using scanning tunneling microscopy (STM) and spectroscopy (STS), the thermally induced deoxygenation of Hn3O on Au(111) is described in this Chapter via the detailed characterization of selected intermediates as

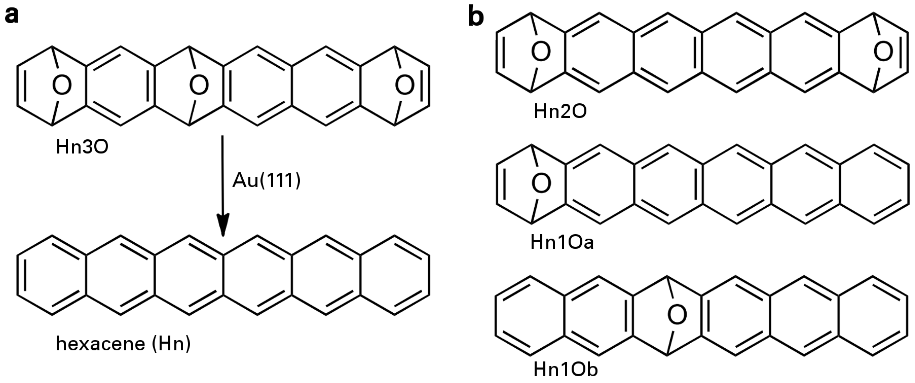

**Figure 6.1 – On-surface route towards hexacene.** **(a):** Generation of hexacene from triepoxyhexacenes (Hn3O). **(b):** Selected epoxy intermediates observed on Au(111).

indicated in Figure 6.1b. In addition, sub-molecular STM imaging of the final product of the reaction shows the stabilization of hexacene and spectroscopy measurements reveal its detailed electronic structure.

## 6.1 On-surface generation

### 6.1.1 Thermally induced synthesis

Hn3O molecules were deposited as a mixture of the four possible diastereomers on a clean Au(111) surface kept at room temperature. Subsequently, the sample was directly annealed at 390 K to induce surface-assisted deoxygenation as introduced in Chapter 4. Figure 6.2a presents a constant-current STM image of the resulting preparation with sub-monolayer coverage recorded a bias voltage close to the Fermi level. One can observe single molecules as elongated protrusions and recognizes various species concerning distinct peaks in their topography. For instance, the isolated molecule at the top right of Figure 6.2a features a marked dumbbell shaped topography. Density functional theory (DFT) calculations were performed to model the adsorption of all relevant molecules on Au(111) and proved that this particular topography is connected to the adsorption geometry of the *syn*-diastereomer of Hn2O with both remaining oxygen atoms facing the surface as illustrated in Figure 6.2b. Since the as-prepared surface without an annealing step was not investigated in depth, isolated precursors could not be found in the experiment. In fact, DFT-based modeling of the adsorption of Hn3O showed that exploring an energetically-favorable geometry on Au(111) was difficult and sometimes led to meta-stable position only. Due to the highly non-planar structure of all four isomers (see Figure 3.9), deposition on the surface kept at room temperature is most likely already followed by a deoxygenation reaction to adopt a more favorable geometry. Molecules without a pronounced peak in their topography are of particular interest since

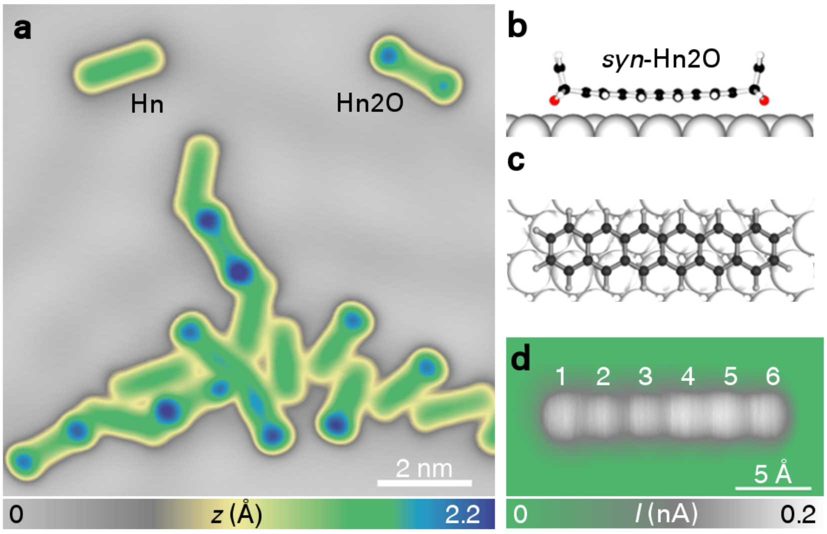

**Figure 6.2 – Surface-assisted deoxygenation on Au(111). (a):** After annealing, the surface showed the presence of hexacene molecules as well as partially deoxygenated intermediates. STM scan (*V* = 0.1 V, *I* = 45 pA) features isolated hexacene (Hn) adsorbed at a kink site of the surface reconstruction while a protrusion with a dumbbell shape close-by indicates the presence of the *syn*-diastereomer of diepoxyhexacene (Hn2O). In addition, self-assembled molecules with different topographies are present. **(b):** Ball-and-stick model of the fully relaxed *syn*-Hn2O molecule obtained by DFT. **(c):** Minimum energy adsorption configuration of physisorbed hexacene with its two middle benzene rings centered above fcc sites of the Au(111) surface. **(d):** Hexacene imaged with a CO-terminated tip at constant height and *V* = −5 mV.

this species indicates the successful formation of hexacene and can be clearly seen for the isolated molecule at the top left of Figure 6.2a. Thus, the final product of the deoxygenation and various intermediates (see a self-assembled cluster of molecules in the overview scan in Figure 6.2a) were present on the surface after annealing at this particular temperature.

Surface-assisted cleavage of all three oxygen atoms from a hexacene precursor is accompanied by a full planarization of the molecule. Hence, the aromatic system is extended to six linearly fused benzene rings. The adopted planar geometry is shown as a DFT-based model in Figure 6.2c and is beneficial for detailed investigations by STM. After functionalizing the tip apex with a single CO molecule, the resolution in STM images of planar hydrocarbons could be increased as has already been demonstrated in many different cases before [35, 51, 106]. Here, this technique was used to image a single hexacene molecule with its chemical structure. After the functionalized tip was stabilized over the bare surface with a set point of *V* = −0.7 V and *I* = 10 pA, the tip height was decreased by 2.2 Å and then kept constant during scanning. The recorded tunneling current data in Figure 6.2d shows that six linearly fused benzene rings can be clearly resolved, thus confirming the formation of hexacene. It should be emphasized that the applied bias is close to zero and can be considered as off-resonant. If the same molecule was imaged with a metal-terminated tip, the constant-height image was featureless and qualitatively similar to the constant-current topography. Clearly, the CO-terminated tip is needed to sense the atomic structure of the molecule.

On the same sample preparation, a detailed comparison between the two diastereomers of the Hn2O intermediate was obtained. Figure 6.3 shows the differences between the topography, adsorption geometry, and electronic resonances of the isolated *syn*- and *anti*-Hn2O, respectively. Both were imaged on Au(111) as dumbbell shaped protrusions as indicated in panels a and b of Figure 6.3. There is, however, a notable difference between the topography of both species, as the *syn* configuration is symmetric in its extent, the *anti* diastereomer shows one tapered part. This side coincides with a single oxygen atom facing away from the surface while the wide part of the dumbbell is related to the fact that two CH groups are pointing towards the tip on this side of the molecule. As a matter of fact, these two particular intermediates are very similar to the used precursor for the tetracene generation in Chapter 4 except that the aromatic core is increased from two to four benzene rings. By probing the differential conductance regarding tunneling spectroscopy at edge positions of the molecular topography, clear resonances could be singled out for both diastereomers as shown in Figure 6.3c.

In the case of *syn*-Hn2O, the corresponding resonant bias values for occupied and unoccupied level are at −1.15 V and 2 V, respectively. These values are shifted to slightly larger values for *anti*-Hn2O and account for −1.05 V and 2.05 V. Nevertheless, the energy difference between frontier resonances is very similar for both diastereomers. The constant-current images of the differential conductance at the respective resonance energies are depicted in Figure 6.3d and 6.3e with a further analysis of the data being shown in the panels f and g. Notably, the maps for *syn*-Hn2O reveal that the recorded images of the molecular resonances are symmetric with respect to two axes, despite the fact that the simultaneously acquired topography image (Figure 6.3a) shows an asymmetry of the apparent height of the two maxima. On the contrary, the $dI/dV$ maps at resonances bias values of the *anti* diastereomer display two dissimilar sides as one would expect from the asymmetric molecule configuration. For comparison, the topography and HOMO resonance of the isolated Hn1Oa molecule is given in Figure 6.4. Here, ten lobes are in total visible if the differential conductance is mapped at a bias of −0.85 V. This resembles the pentacene-like aromatic system of the molecule. Notably, only one configuration of this intermediate with the oxygen pointing towards the surface was observed during the measurements.

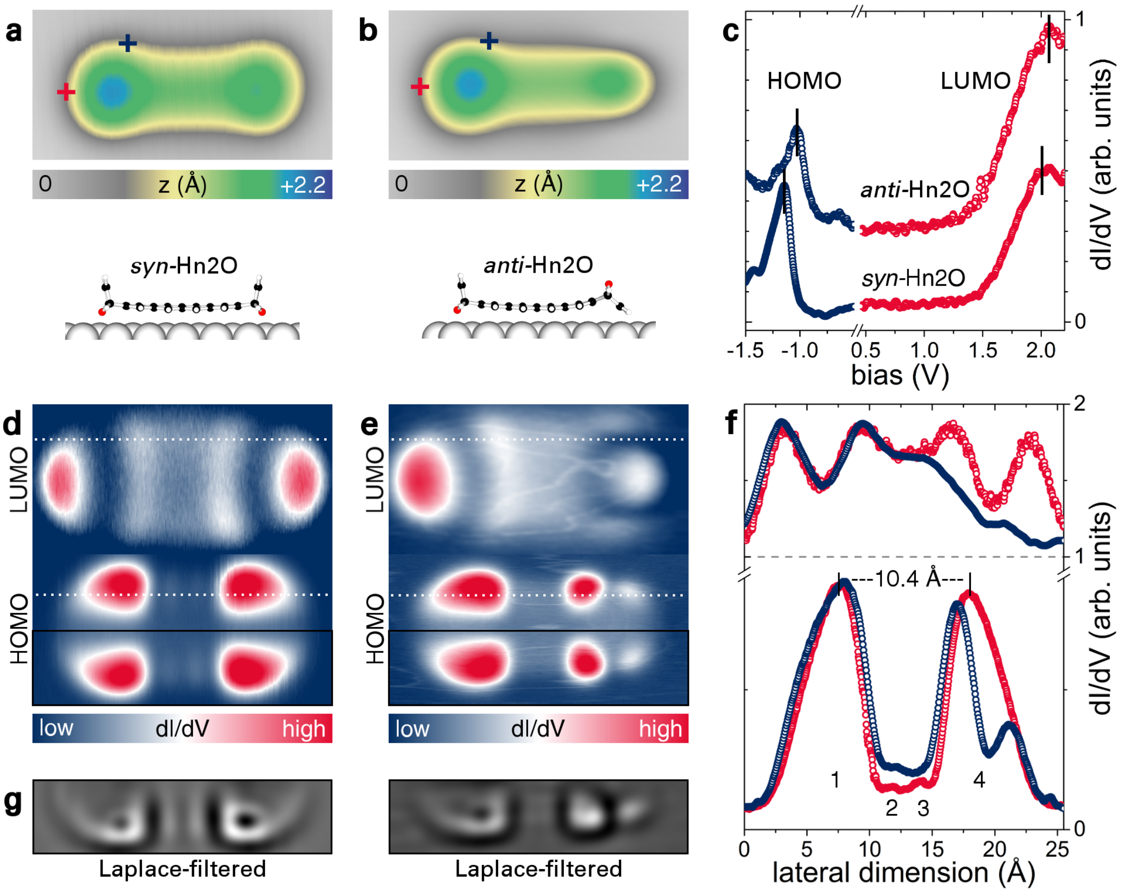

**Figure 6.3 – Topography and electronic resonances of intermediates Hn2O on Au(111).** **(a,b):** STM images ($V$ = 0.5 V, $I$ = 30 pA) of *syn*- and *anti*-Hn2O, respectively. Additionally, the adsorption configuration of both are shown as derived by DFT. **(c):** d$I$/d$V$ spectra of *syn*- (lower curve) and *anti*-Hn2O (upper) taken on the position as indicated by blue and red marks. Spectra are shifted vertically for clarity. **(d):** d$I$/d$V$ maps for *syn*-Hn2O at 2 V (top), −1.15 V (down), and V = 0.1 nA. **(e):** d$I$/d$V$ maps for *syn*-Hn2O at 2.05 V (top), −1.05 V (down), and I = 0.2 nA. All images are 1.3 nm x 2.6 nm. **(f):** Extracted line scans along the d$I$/d$V$ maps as indicated by white dashed lines in the images in d and e. The curves were normalized and shifted for clarity. **(g):** Laplace-filtered images of the lower half of the HOMO maps.

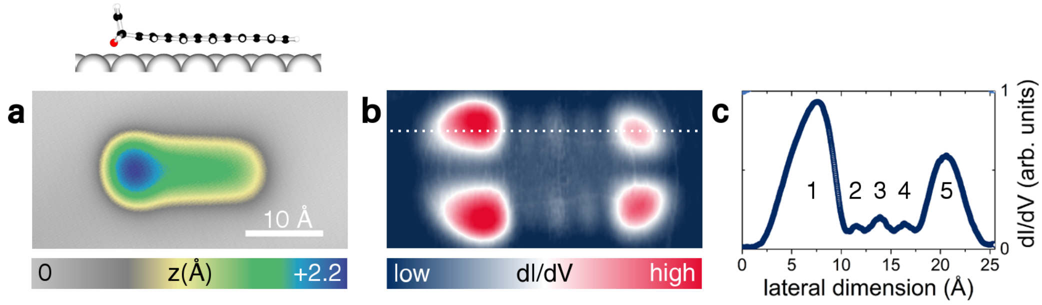

**Figure 6.4 – Intermediate Hn1Oa on Au(111).** **(a):** STM image acquired at $V$ = 0.1 V and $I$ = 40 pA. **(b):** Constant-current ($I$ = 0.1 nA) map of the differential conductance at $V$ = −0.85 V. Image size: 1.3 nm x 2.6 nm. **(c):** Line scan along as indicated by dashed line in b.

### 6.1.2 Self-assembly

Following on from the experimental findings in Chapter 5, one should at least shortly address the observed self-assembly of hexacene precursors and hexacene itself. While the presence of epoxy moieties again clearly favors hydrogen bonding between single molecules, the observed structures are to a great part not regular and without any recurring pattern. Since the precursors feature three oxygen atoms and are a mixture of four different diastereomers, the self-assembly upon adsorption should be complex and remains irregular after annealing as shown for the molecular cluster in Figure 6.2a. Notably, one can occasionally find trimeric structures which are very much in line with the observed anthracene trimers and trimeric tetracene patterns. The corresponding Figure 6.5 shows that intermediates *syn*-Hn2O are again stabilized through hydrogen bonding at their terminal rings. Nevertheless, these ordered domains are too small in size and the assembly after the on-surface generation appears mostly irregular.

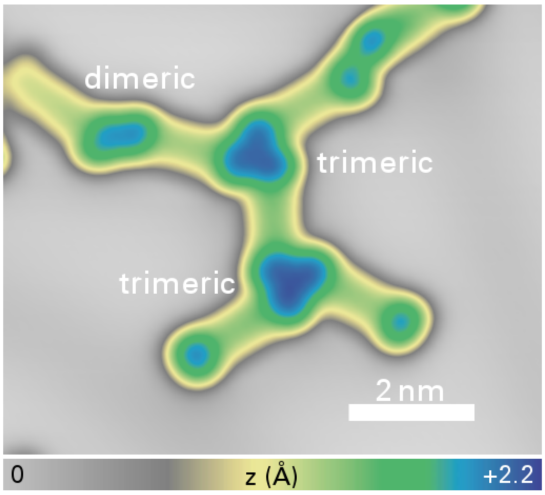

**Figure 6.5 – Self-assembly observed for Hn2O molecules.** Surface was studied after annealing at 390 K. Constant-current image acquired at $V = -0.65\,\mathrm{V}$ and $I = 80\,\mathrm{pA}$ showing *syn*-Hn2O intermediates forming two regular self-assembled trimeric patterns.

### 6.1.3 Higher annealing temperature

To further explore the on-surface reaction mechanism of the hexacene generation, the sample was investigated after annealing at a higher temperature of 420 K. The complexity of different observed molecular species was drastically reduced, since no pronounced peaks in the topography of single molecules were observed anymore. Consequently, this finding indicates that the oxygen atoms at the terminal rings were very efficiently reduced from the precursors. However, thorough examinations showed that not all the molecules featured the same flat topography and slight deviations gave a hint that the central oxygen atoms was not reduced from all precursors. High-resolution imaging at constant-height with a CO-terminated tip as in Figure 6.6 helped to disentangle the true nature of the observed molecular species. Hexacene molecules were imaged

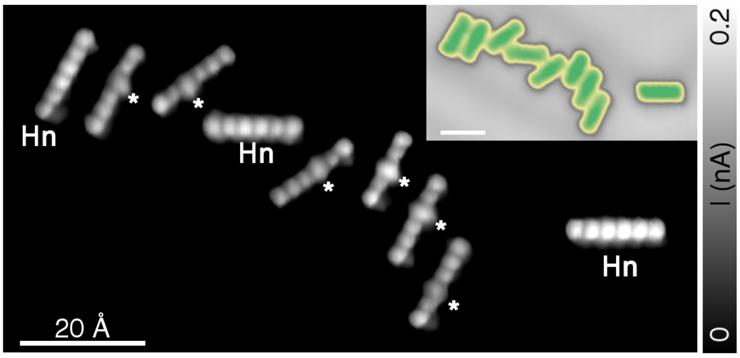

**Figure 6.6 – Sample after annealing at a higher temperature.** Constant-height measurement of the surface annealed at 420 K with a CO-terminated tip and at an applied bias $V = -5$ mV. Hexacene as well as Hn1Ob are present and can be distinguished by a different contrast at the third benzene ring (marked by a star). Inset shows the same surface area as imaged at constant-current and at a bias of $V = -0.1$ V. Since the apparent height scale is the same as in Figure 6.2a, the successful deoxygenation at the terminal rings is immediately clear.

with a sub-molecular corrugation where all six rings appear with the same contrast. However, a fraction of the molecules showed a different contrast at their third benzene ring (marked with a star in Figure 6.6) which is most likely related to the attached center oxygen and matches the structure of the intermediate Hn1Ob. This finding suggests that the activation barrier to cleave the middle oxygen is crucial and must be considerably higher than the barrier involved in the deoxygenation of a terminal ring. Notably, the on-surface generation of hexacene from intermediates Hn2O via Hn1Oa is obtained in a very efficient manner.

## 6.2 Molecular orbital resonances

Scanning tunneling spectroscopy (STS) was performed on single hexacene molecules to investigate the electronic structure in more detail. After STM imaging with a metal-terminated tip as depicted in the panels a and b in Figure 6.7, differential conductance spectra on the periphery of the molecular topography showed strong conductance peaks. By positioning the tip on the end position (red cross in Figure 6.7a), maxima at 1.20 V and 2.55 V were obtained as shown by the red curves in Figure 6.7c. For convenience, one can refer to these electronic molecule resonances as the lowest (LUMO) and second lowest unoccupied molecular orbital (LUMO+1) of the hexacene molecule, respectively. In contrast, probing the occupied molecular levels was achieved by positioning the STM tip on a corner position of the molecule. Typical spectra (see Figure 6.7c) showed well-defined resonances at −0.65 V and −1.65 V, and a weaker peak at around -2.25 V which one can assign for simplicity to the bias values of the highest (HOMO), second highest (HOMO-1) and third highest (HOMO-2) occupied molecular

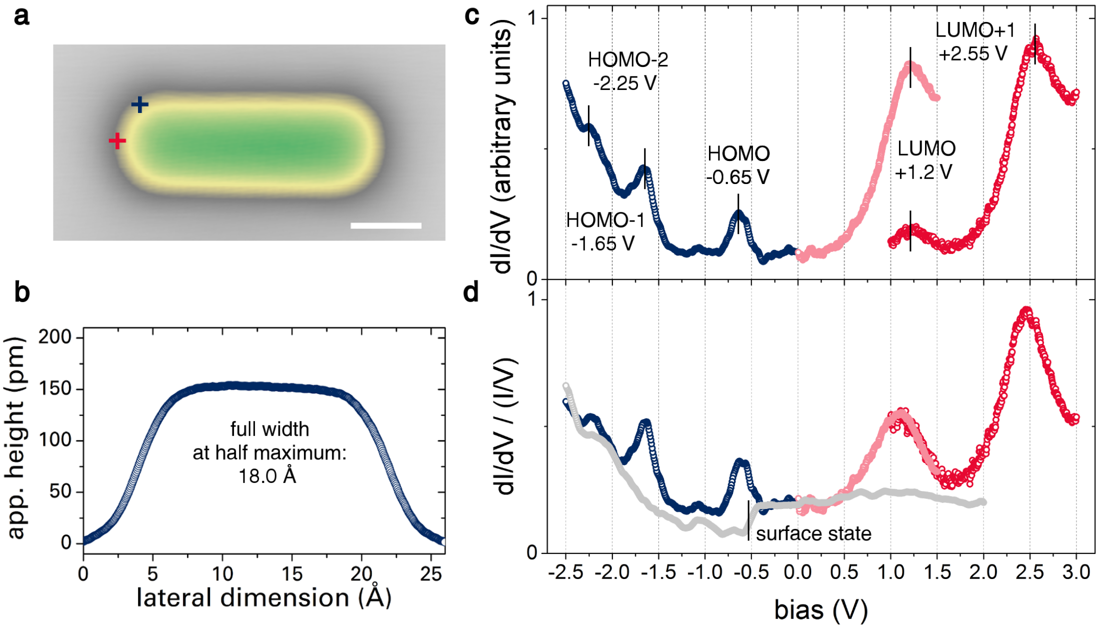

**Figure 6.7 – STM and STS measurements of single hexacene. (a):** Constant-current STM image of a single hexacene molecule at 0.2 V and 30 pA. The scale bar refers to 5 Å. **(b):** Apparent height profile along the molecular long axis in the previous image. **(c):** Three separate differential conductance spectra recorded at constant-height; the blue spectrum was obtained on the corner position while the red curves were acquired at the end position of the molecule as indicated by the STM image in (a). Tip heights were stabilized at $V = 1$ V and, from the left, $I = 0.15$ nA, 0.15 nA and 0.06 nA. **(d):** Normalized differential conductance (differential conductance multiplied by tunneling resistance) for the three respective molecule spectra as well as for one measurement of the bare gold surface (gray curve).

orbitals, respectively. The bias value of the frontier orbital resonance is close to the Au(111) surface state [114] at −0.51 V; however, both features can be well separated by comparing typical spectra of the bare gold surface as shown in Figure 6.7d. In contrast, spectroscopy measurements of single pentacene on Au(111) displayed the LUMO level at 1.3 V and HOMO at −0.9 V [50]. Therefore, one can conclude that the HOMO–LUMO gap probed with STS on Au(111) decreases from 2.2 eV to 1.85 eV. These values are remarkably close to the respective optical gaps determined in an argon matrix [17].

Mapping the spatial distribution of the d$I$/d$V$ signal allowed one to image in detail the electronic structure of adsorbed hexacene, confirming that the observed resonances are coming from tunneling channels built up from the molecular states of hexacene. What all the maps shown in Figure 6.8a have in common is the fact they appear laterally expanded in comparison to the topography[1] and show the highest intensity at the molecular periphery. In fact, this compares well to the measurements for pentacene [50] and is mostly related to the constant-current imaging mode [173]. Here, topography and DOS are convoluted, and the tip interacts more strongly with the π-orbitals when the tip height is lowered at the periphery. The HOMO signature, in particular, illustrates conclusively the aromatic backbone of six linearly fused benzene rings as it shows two times six lobes separated by a nodal plane along the molecular long axis. This symmetry resembles the structure of the frontier orbital density of the free molecule which is in line with previous experiments on pentacene weakly coupled to ultrathin NaCl films [49] or physisorbed on Au(111) [50]. In the experimental image of hexacene, four pronounced lobes are spaced over the whole molecule with a peak-to-peak distance of 16.2 Å along the molecular long axis. Additionally, eight faint inner lobes can be identified from the line scans in Figure 6.8b.

---

[1] Notably, the images in Figure 6.7a and 6.8a have the same lateral dimensions.

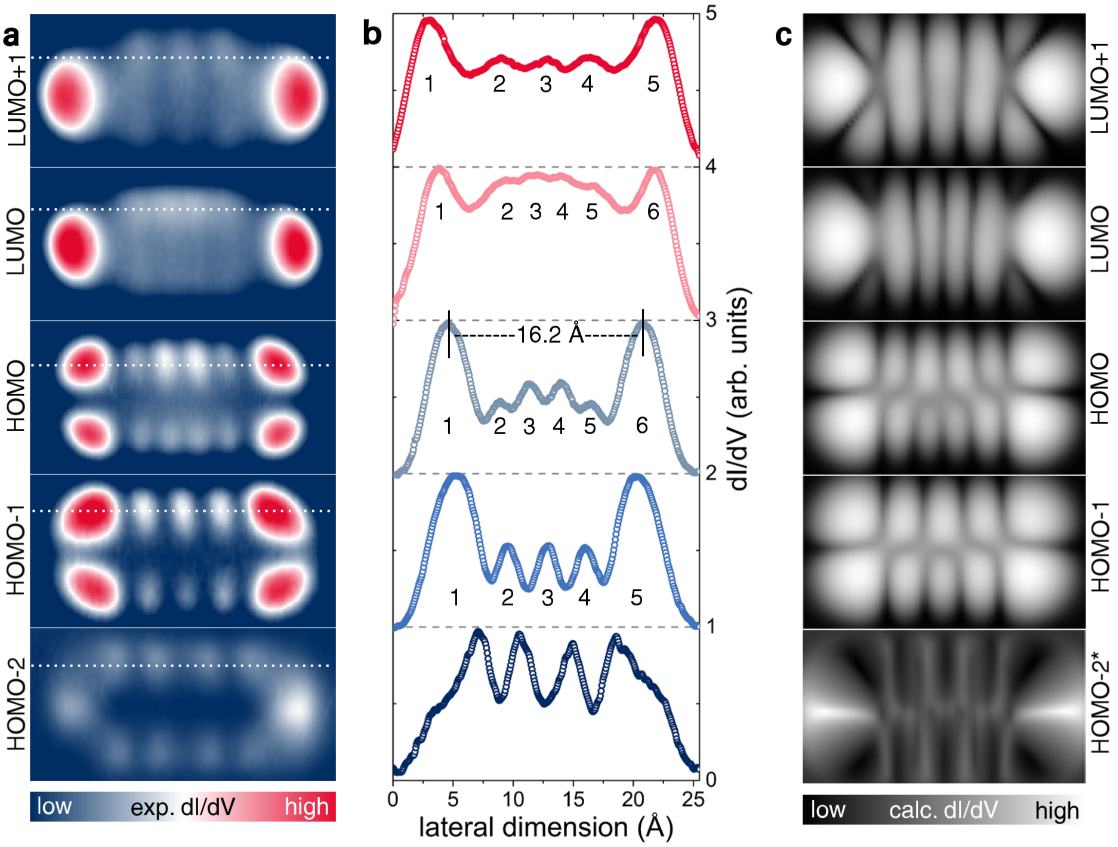

**Figure 6.8 – Imaging of molecular orbital resonances of hexacene.** **(a):** Constant-current maps of the differential conductance at respective resonant bias values. Image sizes are 1.3 nm x 2.6 nm. Current values are, from the top, 0.3 nA, 0.5 nA, 0.2 nA, 0.2 nA, and 0.4 nA. **(b):** Extracted line scans along the d*I*/d*V* maps as indicated by white dashed line in the image in (a). The curves are normalized and shifted for clarity. Despite the used metal-terminated tip, the sub-molecular features become immediately apparent. **(c):** Calculated differential conductance maps at the corresponding energy resonances using ESQC.

If one compares this result with the HOMO map obtained for the key intermediate *syn*-Hn2O (see panel d in Figure 6.3), the on-surface generation can be rationalized through the differences in the measured conductance maps. If the two terminal oxygen atoms are still attached, the largest aromatic system are the four central linearly fused benzene rings. Therefore, the spatial distribution of the four strongest conductance peaks of the HOMO appeared not extended over the whole molecule but were strongly confined to the central part with a peak-to-peak distance of 10.4 Å along the long axis as is shown in Figure 6.3f. The fact that the ratio $16.2/10.4 \sim 1.56$ is close to 6/4 further proves that this confinement of the $\mathrm{d}I/\mathrm{d}V$ map is a quantitative and qualitative fingerprint of the tetracene unit in *syn*-Hn2O. Besides the four major lobes, one can also identify four very faint inner lobes in the HOMO map of this intermediate (see line scans in Figure 6.3f and Laplace-filtered image in Figure 6.3g). Eight lobes separated by a nodal plane along the molecular long axis matches the symmetry of the frontier orbital of the free tetracene molecule. A similar observation can be made for the intermediate Hn1Oa with the pentacene-like aromatic system as shown in Figure 6.4. Consequently, the HOMO maps for different molecular species is ideal to illustrate the on-surface generation of extended aromatic systems.

The spectroscopic measurements show that the first four observed electronic resonances of hexacene (from HOMO-1 to LUMO+1) are well separated in energy and appear as non-degenerate resonances based on the comparison with calculated differential conductance maps. The mono-electronic elastic scattering quantum chemistry (ESQC) approach [131] was adopted to simulate constant–current $\mathrm{d}I/\mathrm{d}V$ maps for hexacene physisobed on Au(111) at the corresponding resonant energies. Panels a, b and c of Figure 6.8 show the striking agreement between experiment and theory as the structure, symmetry, and corrugation of nodes and lobes match very well. Two differences stand out: First, the two second outermost lobes of the LUMO+1 are not visible in the experiment, most likely because they are too low in intensity to be picked up from the metall-terminated tip. Second, the four most inner lobes at the position of the third and fourth benzene rings of the experimental HOMO map are particularly pronounced. This feature is not well reproduced by the corresponding ESQC map. How this peculiar image contrast is depending on the adsorption on Au(111) would need further investigations. Furthermore, it is worth mentioning that the measured $\mathrm{d}I/\mathrm{d}V$ map at the resonance named HOMO-2 largely deviates from what is expected for the STM image of a pure HOMO-2 calculated in a mono-electronic approximation. Further details are given in Section A.4 of the Appendix. One can conclude that an intermixing of molecular orbitals is building up this HOMO-2 electronic resonance, similar to the case of adsorbed pentacene [50].

## 6.3 Discussion

In summary, this Chapter reports on the surface-assisted preparation of hexacene and its first detailed characterization by STM and STS. Notably, the results prove that the introduced acene formation by on-surface reduction of epoxyacenes is not limited to short acenes but also works for larger acenes on a low reactivity Au(111) substrate. This substrate is beneficial for the subsequent investigations of their intrinsic properties since the electronic coupling between fabricated nanographenes and gold can be considered weak [174]. Therefore, the frontier orbital resonances as well as HOMO-1/LUMO+1 levels of hexacene could be visualized in the experiment and showed a conclusive agreement with calculated d$I$/d$V$ maps. Further, the spectroscopic measurements show that the Fermi level of hexacene adsorbed on Au(111) is well separated from any molecular resonances[2], i.e. the LUMO resonance is clearly above zero bias while the HOMO resonance is well below. In that sense, the adsorbed molecule retains a semi-conducting property and the charge transfer between substrate and molecule is small. If a strong charge transfer from the substrate to the molecule were present, the spectrum would lose the semi-conducting character, and the LUMO resonance should be pinned close to the Fermi level as observed for pentacene on more reactive metal substrates [88, 92].

---

[2] By subtracting the metallic background curve from the molecular spectrum in Figure 6.7d, this property becomes evident.

# 7 Br-substituted precursors of heptacene on Au(111)

*Substituting hydrogen atoms with halogen atoms changes the chemical reactivity of the precursors and increases the complexity of possible surface reaction. However, this Chapter shows that unsubstituted heptacene can be imaged on the surface.*

The success of on-surface synthesis as a bottom-up strategy towards the fabrication of atomically precise nanostructures has been mainly connected to the Ullmann type intermolecular coupling reaction [21]. By designing halogen-substituted precursors, selected bonds of deposited molecules can be activated via thermally-induced dehalogenation [24]. This is related to the fact that bonds between carbon and halogen atoms are considered substantially weaker than bonds between carbon and hydrogen [175]. Upon diffusion, precursor molecules are then likely to fuse through C-C coupling at the preselected activated sites and can form extended covalent structures. While conventional sublimation of large molecular systems would eventually lead to their fragmentation due to the required high thermal energy, employing the Ullmann type surface reaction is a truly vacuum-processable approach to fabricate 1D and 2D structures on a metal substrate. This has been instrumental in the formation of networks [24, 25], molecular wires [26, 28], and graphene nanoribbons of various edge topography and width [29–32].

In this Chapter, the experimental efforts to combine on-surface reduction, bond activation, and Ullmann type coupling to fabricate extended covalent structures with acene subunits are shown. Starting from the molecular precursor Hp4Br3O as depicted in Figure 7.1a, the Br-substituted terminal rings are likely to become activated for C-C coupling reactions while intramolecular reduction should lead to a heptacene-like seven aromatic ring system. Once the Br atoms are dissociated, the structure of the intermediate (see Figure 7.1a) can be considered as aryne-like radical in the $\sigma$-electron system

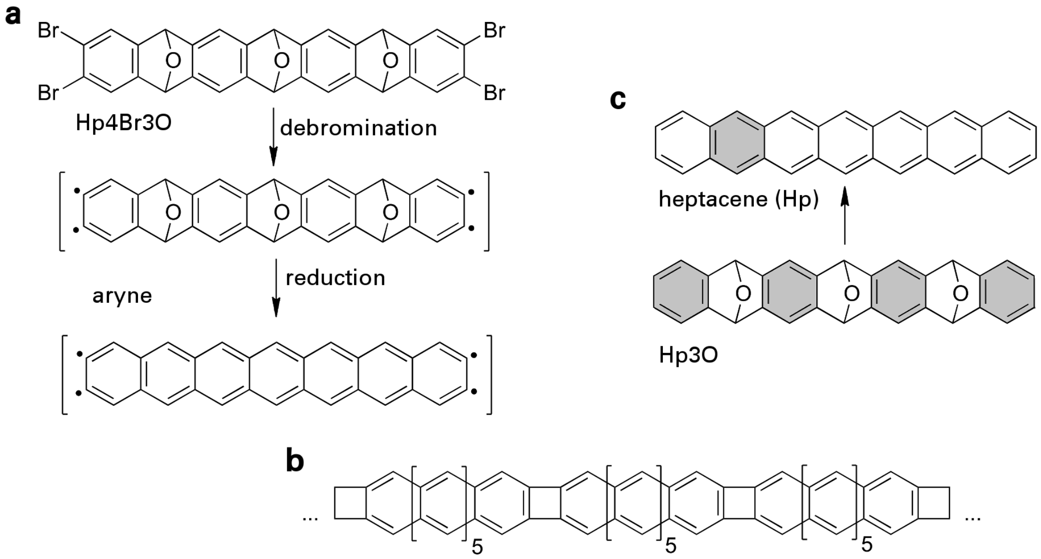

Figure 7.1 – On-surface chemistry of a Br-substituted epoxyacenes. (a): Precursor molecule tetrabromotriepoxyheptacene (Hp4Br3O). (b): One possible idea of heptacene-based polymer based on Ullmann-type coupling as proposed by the group of D. Peña at the University of Santiago de Compostela. (c): Unsubstituted triepoxyheptacene (Hp3O) and its reduced form heptacene. The aromatic Clar sextets are marked with gray.

which shows an exceptional high reactivity even at cryogenic temperatures [40]. The main idea is that many of such activated intermediates diffuse on the surface and can couple to each other. For the reaction scheme, one can expect that extended covalent 1D copolymer structures are formed through subsequent C-C coupling steps at the terminal rings as shown in Figure 7.1b. It is important to emphasize that this route cannot lead to the fabrication of polyacenes.

Given the fact that each heptacene-subunit would have an extraordinary low gap between the HOMO and LUMO level, the resulting polymer should be a promising material with a finite but very low transport gap. By performing so-called lifting experiments with the tip of the STM [26, 28, 176], the transport conductance could be further studied for possible applications in molecular and organic electronics.

## 7.1 On-surface chemistry

By analogy with a suitable heptacene precursor with four aromatic sextets[1] as shown in Figure 7.1c, the closely-related derivative Hp4Br3O was used for on-surface experiments. It was deposited onto the Au(111) substrate kept at room temperature and the resulting surface preparation was intensively studied after annealing the surface first at 470 K and then 530 K. A key experimental observation was that no extended structures could be found in large-scale STM images; however, mostly self-assembled structures of finite size. Further STM images are given in Section A.5 of the Appendix. Similar to the case of the hexacene generation (see Chapter 7), isolated molecules were predominately found at the elbow site of the surface reconstruction and could be studied in greater detail. In fact, after annealing at 470 K most molecules appeared completely flat or with one peak in their topogaphy. Both cases will be discussed in the following.

---

[1] Following the discussion of E. Clar [58], four aromatic sextets in the Clar structure of the precursor increases the stability drastically compared to the closed-shell state of genuine heptacene with just one aromatic sextet.

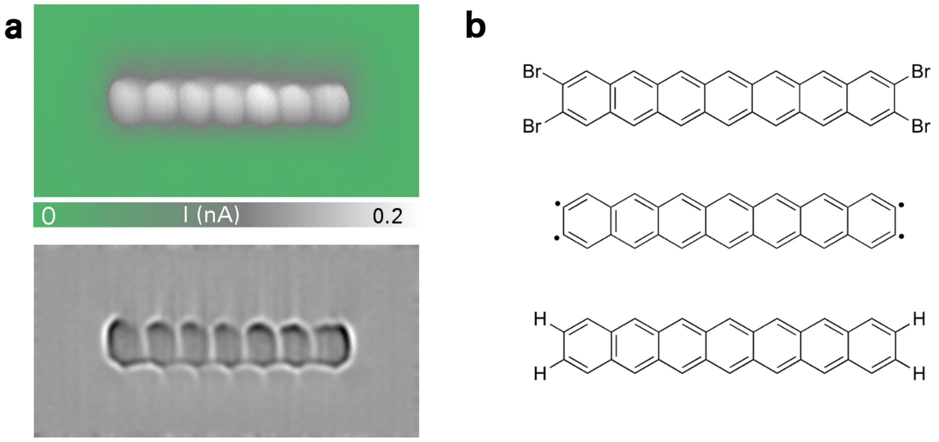

**Figure 7.2 – Imaging of the chemical structure of heptacene.** **(a):** Constant-height image recorded with a CO-terminated tip at $V = -5$ mV. The lower image corresponds to the Laplace-filtered data. Image size: 1.5 nm x 3 nm. **(b):** Three chemical structure which are in principal possible for the observed single molecule; however, the data proofs that the genuine heptacene (bottom row) is observed in the experiment.

First, typical high-resolution images of single flat molecules with a CO-terminated tip at constant-height and small bias showed clearly seven linearly fused rings as demonstrated in Figure 7.2a. Thus, one can conclude that the separation of all three oxygen atoms worked; however, the structure of the terminal rings was not immediately clear. Figure 7.2b shows three possible cases which one should take into account based on the designed experiment. Since the experimental constant-height image does not show any peculiar features at the end rings, the Br-substituted heptacene (top structure in Figure 7.2b) can be ruled out based on the fact that Br atoms would give a pronounced contrast as demonstrated in high-resolution SPM images of single molecules [41]. Second, the intermediate case (middle structure) is known to be highly reactive, and AFM measurements of the aryne structure with atomic resolution have proven that this particular radical structure bonds strongly to the metal surface [40]. Given the fact that no Ullmann-based long-range structures were observed on the surface and Figure 7.2a looks very similar to the current image of hexacene (see Figure 6.2d), one can conclude that the observed structure is genuine heptacene. Since the crucible temperature needed to sublime the precursors was high due to the large molecular weight, it is reasonable to assume that the bromine atoms were already dissociated during deposition. Even though all the experiments were carried out in UHV conditions, residual hydrogen is always present in the vacuum chamber and the dominant part of the rest gas spectrum. Thus, the four activated bonds of the precursors were passivated with hydrogen before a coupling reaction could occur.

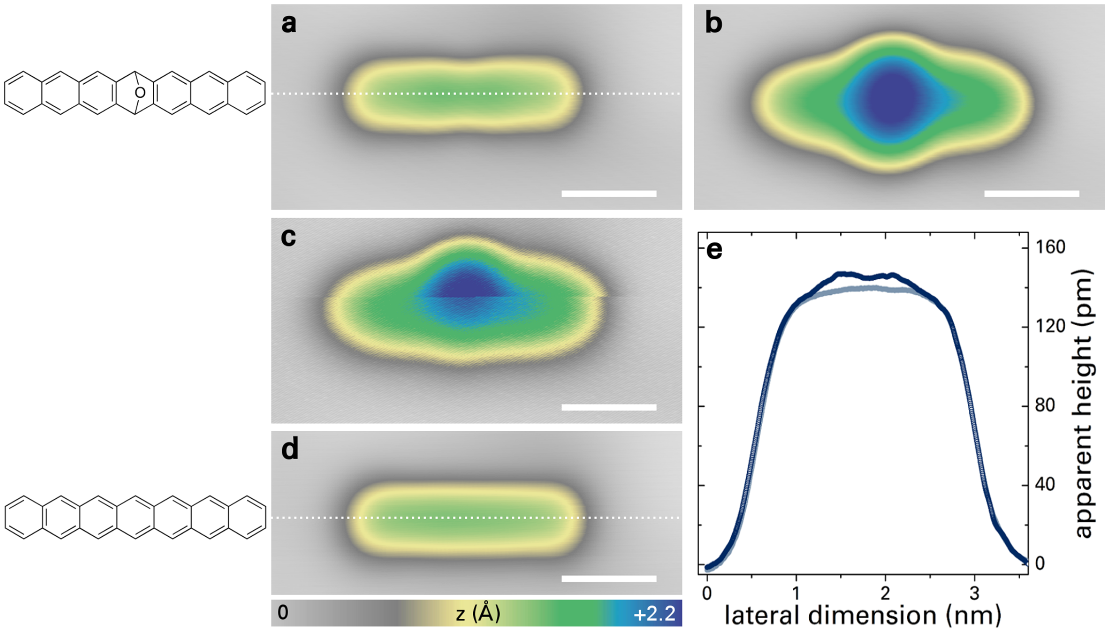

**Figure 7.3 – Imaging of an intermediate and tip-induced reaction to form heptacene. (a):** STM image of intermediate at $V = 0.1$ V and $I = 100$ pA. **(b):** STM image of the same molecule at $V = 2$ V and $I = 100$ pA. **(c):** Imaging at 2.2 V induced a chemical reaction during scanning. **(d):** STM image ($V = 0.1$ V, $I = 100$ pA) after the manipulation event. Notably, if this molecule is now imaged under the same conditions as in (b) (not shown here), the peak at the center of the topography is not present anymore. **(e):** Comparing two line scans along the molecular long axis as indicated by the dashed line in (a) (dark blue curve) and (d). All scale bars refer to 1 nm.

Second, single molecules which appeared elongated but not entirely flat at small bias (see Figure 7.3a) showed a strong bias-dependence for the topography. The constant-current STM image at a higher bias of 2 V features one pronounced peak at the center as indicated by Figure 7.3b and can be assigned to the intermediate with one oxygen atom still attached.[2] This strong contrast change directly at the oxygen position can be rationalized in a simple way as follows. If the epoxy group is still attached, the largest aromatic core of this intermediate is equal to two anthracene-units. For large enough bias values, the LUMO resonance of these two acene-like subunits[3] becomes accessible and shows its strongest intensity at the end positions accordingly to the measurements in the previous Chapter. Since two anthracene-units are fused via the epoxy group, the center of the intermediate is a high-conductance point of the molecule. Thus, the apparent height must be clearly increased in this region if the molecule is scanned at constant-current and large enough bias. One should emphasize that this strong bias-dependence is a clear *electronic* effect and not directly related to the geometry of the molecule. In fact, it is very difficult to deduce information about the configuration of the oxygen bridge, i.e. whether it is pointing up or down. Similar to the experiments on Cu(111), scanning at higher bias occasionally triggered the transition to the completely planar state as illustrated in the panels c-f in Figure 7.3. While this tip-induced reaction was not systemically studied, heating at 530 K led to the observation that virtually all isolated molecules at kink sites could be identified to be flat.

---

[2] In fact, intermediates with one off-center peak at high bias were also observed corresponding to the remaining oxygen atoms at the off-center position.

Evaporating the precursors onto the warm surface kept at 470 K to increase diffusion while deposition lead to the observation of the same principal structures on the surface. This empirical fact supports the assumption that the Br-dissociation already took place in gas-phase, leading to transient states which are then quickly passivated with hydrogen before Ullmann-coupling reaction could be triggered on the surface. While one could occasionally find two or three molecules covalently fused through a single carbon-carbon bond as shown in Figure A.7 in the Appendix, the rate of this process is too low to be of any interest. However, the fabrication of unsubstituted heptacene molecules is an intriguing result and further proofs the applicability of on-surface reduction to stabilize large acenes. In the following parts of this Chapter, the properties of single molecules are investigated in greater detail. At this point, one should emphasize the fact that the synthesis of unsubstituted heptacene dates back to the earliest attempts from E. Clar in 1942 [6]. Nevertheless, it took more than 60 years until an unambiguous evidence for its isolation could be obtained [177]. Similar to their work on hexacene, the group of D. Neckers obtained heptacene from a diketone precursor which was found to be stable up to 4 h in a polymer matrix. The characterization in solution and in thin films were very recently achieved via temperature cracking of a diheptacene precursor [178].

## 7.2 Heptacene stabilized on Au(111)

### 7.2.1 Bias-dependent topography

Single heptacene molecules were studied in more detail. In particular, the topography was imaged with a functionalized tip. STS measurements proved to show the sur-

---

[3] See Section 5.1 for the description of the LUMO resonance of anthracene.

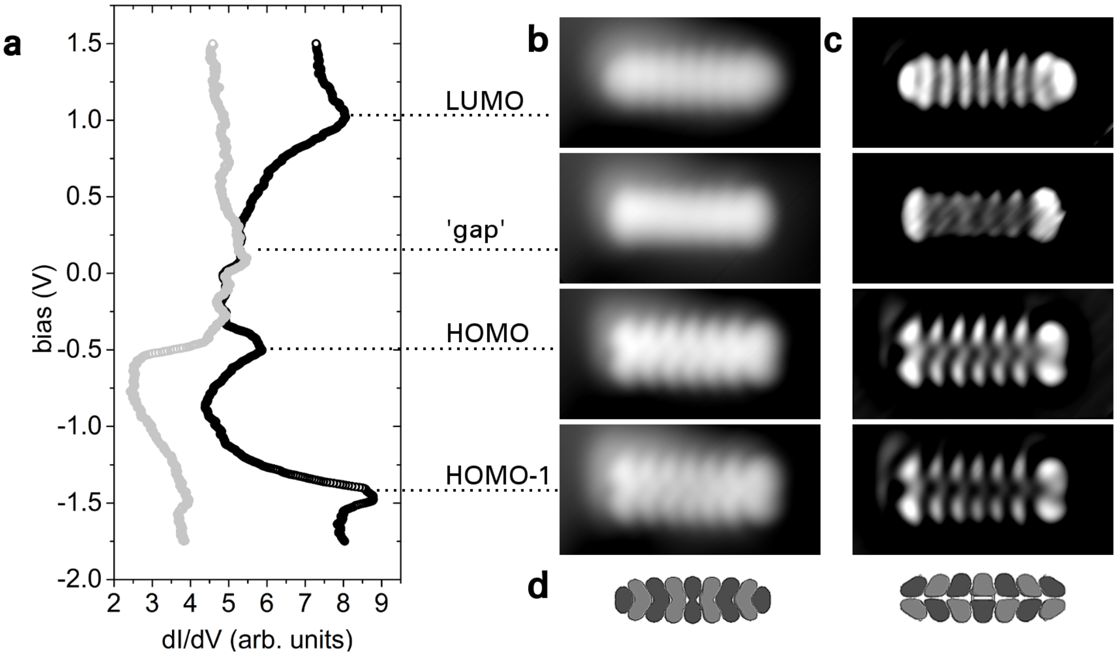

**Figure 7.4 – Bias-dependent topography of heptacene. (a):** Differential conductance spectra acquired of a heptacene molecule (black curve) and of the bare Au(111) surface (gray curve). For simplicity, the peaks in the spectrum are referred to the orbitals of the free molecule. **(b):** Constant-current topography acquired at *I* = 0.3 nA and the indicated bias values. Image size: 1.8 nm x 3.6 nm. **(c):** Laplace-filtered topography. **(d):** Contour plot of LUMO and HOMO of the free heptacene molecule as derived by ArgusLab.

face state of Au(111) in a spectrum of the bare metal (see Figure 7.4a) while imaging of the molecule gave a strong intramolecular resolution. In particular, if a heptacene molecule was probed at constant-current with a bias close to the LUMO and HOMO resonances, the respective topography images showed a corrugation corresponding to the symmetry of the gas-phase frontier orbital densities as proven in Figure 7.4b. After Laplace-filtering (see Figure 7.4c), this became even more clear and showed the high-quality of the obtained images. These observations match the experimental finding for the bias-dependent topography of pentacene on Au(111) [50]; however, with much more pronounced internal structure due to the employed functionalized tip. All nine lobes could be resolved in the LUMO topography while the differential conductance maps of pentacene [50] and hexacene measured with a metal-terminated tip showed less sub-molecular contrast. Notably, if heptacene was imaged at a small and off-resonant bias, the recorded topography appeared almost featureless despite the used functionalized tip. This observation is in stark contrast to the reported measurements of single pentacene on Cu(111) [45]. Due to the stronger coupling to the substrate, the topography of pentacene measured with a pentacene-terminated tip at a small bias of $V = -0.1\,\mathrm{V}$ appeared with a LUMO-like structure and indicated the stronger charge transfer and stronger shift of the molecular energy levels on this surface.

It is worth noting that the obtained constant-current topography at the bias corresponding to the HOMO-1 resonance shows the same sub-molecular structure as the image at the HOMO resonance. This observation can be explained by the fact that the topography is obtained by probing at a constant tunneling current. Following Equation 2.8 in Chapter 2.1, the current is connected to the *integral* of tip and sample states from zero to the desired bias value. Therefore, information of the resonant states of both HOMO and HOMO-1 are included in the topography; however, the former dominates the recorded image at this bias. In contrast, the differential conductance at a desired bias (see Figure 7.4a) is *directly proportional* to the sample DOS at this voltage as introduced by Equation 2.13. If the $\mathrm{d}I/\mathrm{d}V$ signal is recorded at the HOMO-1 bias, the lobe structure of this molecule orbital resonance should be recovered in the image. This will be demonstrated in the next Section.

### 7.2.2 Differential conductance measurements

Starting from the differential conductance spectra shown with the functionalized tip, the measurements of single heptacene molecules were repeated with a purely metal-terminated tip. The first two empty state resonances were obtained by performing tunneling spectroscopy on the end position of the molecule and showed the LUMO and LUMO+1 resonance at 1.0 V and 2.25 V, respectively. Mapping of these two resonances led to the images shown in Figure 7.5a. Notably, the maps are again dominated by two high-intensity peaks at the molecular end positions while only a faint lobe-corrugation is visible at the center. This structure is very similar to the data for hexacene. By measuring tunneling spectra with a comparable large molecule-tip separation, a third peak at 3.2 V could be resolved as shown in Figure 7.5b. However, this resonance is already at a bias range where the tunneling electrons can trigger a dehydrogenation of the molecule, hence there is a finite chance that the molecule is drastically manipulated during imaging. This is why the obtained map (see Figure A.9 in the Appendix) of this high-order resonance of heptacene does not show the same high quality as the other maps, and the structure is not discussed in greater detail.

In the case of the occupied states, the obtained $\mathrm{d}I/\mathrm{d}V$ images of the first two resonances at −0.55 V and −1.4 V, respectively are depicted in 7.5c. Subsequently, the zigzag edge of the molecule was probed with particular care via bias-dependent differential conductance measurements. The STM tip was scanned at constant height along the molecular long axis but off the center as defined by the white dashed lines in Figure 7.5c. Starting from the smallest bias of −1.75 V, the applied bias was increased after each line with a step size of 25 mV until the final voltage of −0.25 V was reached. The tip was stabilized between two spectra with switching the feedback loop on and using always the same tunneling parameters to make sure that all the line spectra were carried out at the same height above the molecule. The resulting differential conductance data was normalized and the metallic background contribution subtracted. The two-dimensional color plot in Figure 7.5d is a convenient way to depict the data with the horizontal axis showing the spatial dimension along the zigzag edge and the vertical axis equal to the applied bias. It becomes immediately clear that the two molecular resonances of HOMO and HOMO-1 are visible in the map. In particular, the broadening with respect to the applied bias is apparent.

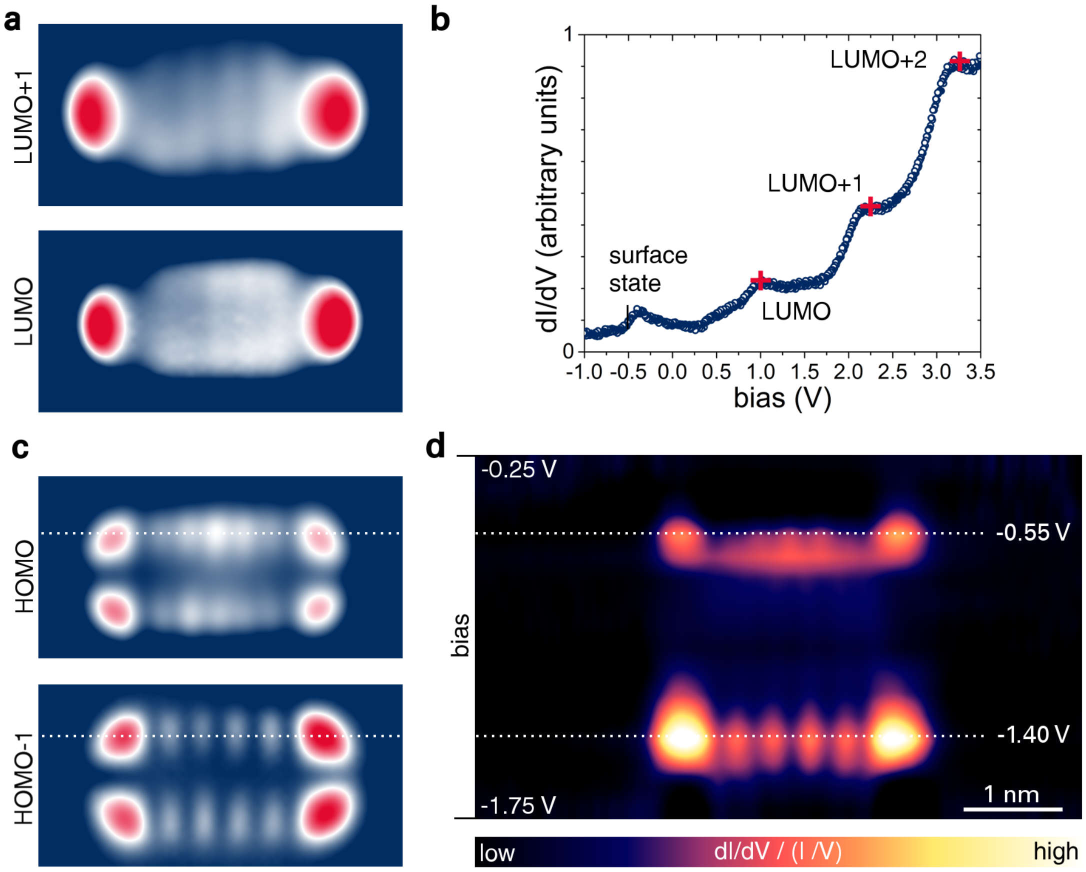

**Figure 7.5 – Molecular orbital resonances of heptacene. (a):** Constant-current ($I$ = 0.3 nA, metal-terminated tip) maps of the differential conductance acquired at 2.25 V (upper image) and 1.0 V, respectively. Image size: 1.8 nm x 3.6 nm. **(b):** Differential conductance spectra on a single heptacene molecule. **(c):** Constant-current ($I$ = 0.3 nA) maps of the differential conductance acquired at −0.55 V (upper image) and −1.4 V, respectively. Image size: 1.8 nm x 3.6 nm. **(d):** Bias-dependent normalized conductance measurements along the zigzag edge of heptacene.

Not surprisingly, the heptacene showed also a HOMO-2 resonance as presented in Section A.5 of the Appendix. The observed symmetry is again entirely different compared to the HOMO and HOMO-1 resonances. Consequently, the obtained differential conductance data on the orbital resonances are very similar to the results on hexacene

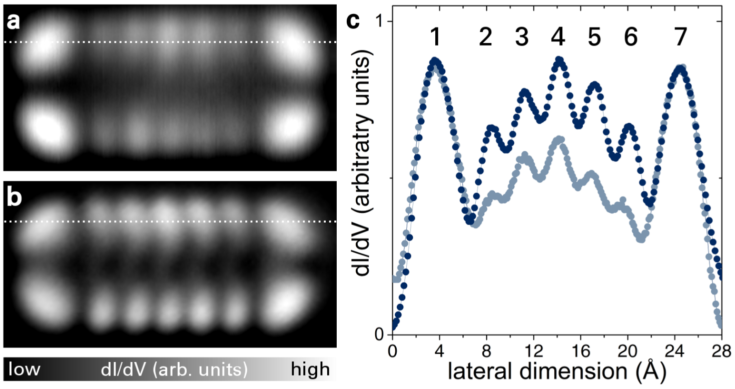

**Figure 7.6 – HOMO resonance of heptacene mapped with two different tips. (a,b):** Constant-current ($I$ = 0.3 nA) maps of the differential conductance acquired at a bias of −0.55 V with a metal-terminated tip (a) and functionalized tip (b), respectively. Image size: 1.4 nm x 2.8 nm. **(c):** Extracted line scans along the differential conductance maps as indicated by white dashed line. The dark blue curve corresponds to image (b).

but with the expected difference for a seven-ring molecule. In particular, Figure 7.6 proves that the d$I$/d$V$ map at HOMO-resonance can be imaged with a metal-terminated and CO-terminated tip to resolve 14 lobes. Interestingly, the inner lobes follow a particular intensity distribution with the central fourth lobe showing the highest differential conductance for both used tips. Finally, the resonant bias values are shifted closer to the Fermi level as shown in the Table 7.1 and the HOMO-LUMO gap is further reduced to 1.55 eV.

| molecule | HOMO-2 | HOMO-1 | HOMO | LUMO | LUMO+1 |
|---|---|---|---|---|---|
| hexacene | −2.25 V | −1.65 V | −0.65 V | 1.2 V | 2.55 V |
| heptacene | −2.15 V | −1.4 V | −0.55 V | 1.0 V | 2.25 V |

**Table 7.1 – Bias values of molecular resonances for adsorbed hexacene and heptacene.** Summary of the obtained resonant bias values for the first four orbital resonances. The differential conductance spectra were acquired at equivalent positions and with metal-terminated tips.

## 7.3 Discussion

In this Chapter, the experimental results on the Br-substituted heptacene precursors showed that the proposed idea of the fabrication of heptacene-based polymers could not be obtained on Au(111). Since STM images with high-resolution indicated the stabilization of genuine heptacene with hydrogen termination on the surface, Br-dissociation is likely to take place in gas-phase before any surface-assisted coupling reaction could occur. In fact, a previous field-effect device study of the Z. Bao group [179] supports this fact since they found that a similar but smaller molecule with a pentacene core and four Br-atoms at the same peripheral positions in the terminal rings could not be heated beyond 420 K without starting to degrade the material via gradual Br-loss. While the comparison of sublimation temperatures of sub-monolayer preparations and thin-film fabrications in two different setups are not always without a doubt; it is another strong hint in this case that the investigated precursor is not vacuum-processable with standard sublimation methods. In contrast, the on-surface deoxygenation proved again to be a capable approach to prepare an extended ring system. In fact, the shown single-molecule topography and differential conductance images, as well as the energy value between HOMO and LUMO levels, are all very much in line with the results on hexacene.

# 8 Summary and outlook

*This final Chapter is devoted to giving an overview of the most relevant experimental results and a brief discussion of their importance. Secondly, the challenges and chances for future acene-based investigations and applications are addressed.*

## 8.1 On-surface synthesis

In summary, this work shows a novel and surface-assisted route for the stabilization of acenes on Cu(111) and Au(111) from air-stable precursors. The AFM images with atomic resolution in Chapter 4 introduces this reduction conclusively for diepoxytetracenes. While the fabrication of non-reactive tetracene is undoubtedly more of scholastic importance, the observed stabilization of the highly elusive hexacene and heptacene in Chapter 6 and 7, respectively is remarkable. Without a doubt, the used UHV system is highly beneficial for this kind of study and allows the investigation of a large acene with utmost precision and stability while the same molecule would degrade or react within a split-second if treated in any other environment.

The results display the scalability of this on-surface approach as a synthetic tool to access extended acene systems at the single molecule level. By designing the suitable precursor, this method should have the potential to generate oligoacenes beyond the size limit of what has been experimentally observed so far, i.e. larger than nine rings[1] While the photoinduced decarbonylation (CO as leaving group) reaction as used for matrix isolation of nonacene [18] may also be extended, it becomes increasingly difficult to confirm the acene generation from a collective absorption spectra alone. Here, SPM investigations with high spatial resolution are beneficial since one can distinguish and select between final reaction products and intermediate molecules in-situ as demonstrated in Chapter 6. Moreover, the surface fabrication is highly favorable for planar and molecular-scale applications. Here, it would be useful to also explore surface mechanisms to generate large acenes on less-reactive substrates, possibly also through the activation with light, or the in-situ transfer to semi-conducting or insulating substrates after the synthesis.

---

[1] After the submission and before the defense of this thesis, the on-surface stabilization of nonacene [180] and decacene [181] was indeed reported.

Obviously, the role of the supporting metal surface is crucial in the presented experiments and can be paraphrased by three terms: adsorption, deoxyenation, and planarization. First, imaging of the short epoxy-precursors showed that they preferably adsorb with the oxygen atoms facing the surface as confirmed by experiments and DFT-based modeling. Second, different behavior of diastereomeric diepoxytetracenes during single-molecule experiment indicated that a high interaction with the metal is favorable for deoxygenation. One can argue that the substrate substantially lowers the activation barrier which is needed for reduction. Thus, the catalytic effect of coinage metals allow deoxygenation to occur at rather low temperatures, similar to what has been observed before for dehalogenation barriers [29]. Third, while one cannot rule out the possibility that larger epoxyprecursors are partially deoxygenated during sublimation due to the supplied thermal energy, the interaction with the surface is still key for planarization. One should emphasize the fact that isolated precursor and intermediates are highly non-planar in gas-phase and the stabilization of transient states after deoxygenation to form a planar structure is favored by the presence of a surface. With increasing precursor complexity and number of epoxy groups, there is growing competition between the optimum gas-phase structure and favorable elongated adsorption geometry. In vacuum, the $sp^3$-hybridization of the oxygen-bridged carbon atoms favors a non-planar structure while aromatic benzene rings preferably adopt a planar adsorption on a metallic surface. The results on the stabilization of hexacene and heptacene suggest that the elongated adsorption geometry holds the upper hand and is perhaps even causing oxygen separation during deposition already.

The large-scale investigation of Chapter 5 made it clear that the pattern formation of in-situ generated acenes differ from what one would expect for such a high-symmetry molecules. The fact that the observed self-assembly before and after reduction can be described in a similar way makes the implications of an on-surface synthesis for the ordering at the metal-organic interface vivid.

## 8.2 Electronic properties

The stabilization of highly reactive hexacene and heptacene on Au(111) allowed STM and STS measurements of their electronic properties. Since the acenes are physisorbed on the surfaces, their frontier resonance levels, even if broadened and energetically shifted due to interaction with the continuous states of the metal [83, 87], still correspond

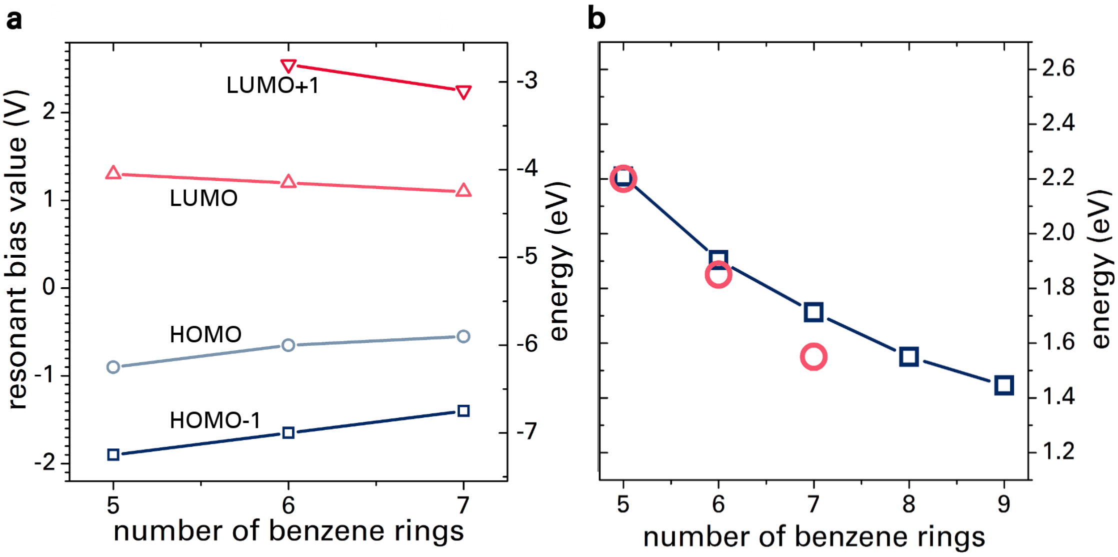

**Figure 8.1 – Electronic resonances of adsorbed pent-, hex-, and heptacene on Au(111). (a):** Resonant bias values as confirmed by STS measurements of single acenes. The experimental values for pentacene are taken from [50]. The respective errors are smaller than the shown symbols. The corresponding energy values (scale on the right) are calculated via the work function of Au(111). **(b):** The HOMO-LUMO gaps as derived from (a) (red dots, error value as large as symbol) in comparison to the optical $S_0 - S_1$ transitions (blue curve) obtained by absorption measurements at 30 K and in a solid argon matrix [17, 18].

to the gas phase ionization and affinity levels. Therefore, the frontier orbital resonances, as well as HOMO-1/LUMO+1 levels of both large acenes, could be quantified and visualized in the experiment. As it turned out, the planar structure and extended molecular resonances of these hydrocarbons are particularly suited to obtain high-resolution images.

First, the bias values of molecular resonances should be discussed. As illustrated in Figure 8.1a, the energy spacing between the accessible molecular levels in STS measurement is clearly reduced as one makes the transition from pentacene [50] to heptacene. This trend is in line with a simple *particle-in-a-box* model of a smaller level spacing for a weaker spatial confinement of the frontier orbitals. In a similar way, the calculated energy gap between the HOMO and LUMO resonances in STS experiments can be plotted versus the number of linearly fused rings as shown in Figure 8.1b and indicated the drastically reduced HOMO-LUMO gap. Interestingly, the experimental values match the optical gap values as determined by H. Bettinger et al. [17, 18] well, even though the underlying fundamental principle to obtain the respective values are different, and STS values depended critically on surface polarization effect. This observation is illustrated by the fact that pentacene which was electronically decoupled from Au(110) using a NaCl monolayer showed a HOMO-LUMO gap as large as 4.0 eV in single-molecule STS experiments [47]. Second, studying the electronic resonances of acenes directly on the metal has the advantage that several molecular orbital resonances become accessible in the usable bias range. While pentacene showed only four conductance maxima in tunneling spectra [50], hex- and heptacene featured five and six resonances, respectively. This class of molecules is an ideal system to study the image formation in differential conductance maps. In fact, measurements of all three acenes showed that the sophisticated ESQC method is needed to simulate the obtained maps correctly. Images acquired at the frontier orbital resonances are well reproduced while higher order maps tend to be more difficult to be calculated as already pointed out in the work on pentacene. This is a clear proof that the one-electron picture of orbitals is only a limited and simplifying description of the electronic structure of molecular resonances in STS experiments where the interaction of tip, molecule, and substrate needs to be considered.

In a nutshell, the obtained spectroscopy measurements of hexacene and heptacene are very much in line with the pentacene and with one would expect for a larger fully $\pi$-conjugated system. Despite the theoretically predicted open-shell ground state for oligoacenes larger than pentacene [59] or hexacene [2], the interaction with the underlying metal makes it difficult to access a possible radical character in the electronic ground state of adsorbed hexacene and heptacene. In the case of extended atomically precise graphene nanoribbons, the transfer to a thin insulating NaCl film was needed to detect the intrinsic properties of electronic states localized at zigzag edges [32, 56]. Similarly, the radical character in the $\pi$-electron system of triangulene could not be detected on the bare metal but on a ultrathin film of xenon only [7]. In accordance, while the metal substrate is favorable for the on-surface synthesis of large acenes, a decoupling from the metal would be favorable to provide access to the anticipated unique ground state. In combination with spin-sensitive measuring methods, e.g. spin-polarized STM, this approach will pave the way for the unraveling of the electronic structure of large acenes.

# A Appendix

## A.1 Designed LabView program

Controllable and reproducible deposition of the molecular precursors is of paramount importance for their on-surface investigations. Therefore, I have designed a LabView-based program which allows one to monitor and to record the pressure values in all three parts of the UHV system while also giving access to an Eurotherm-based temperature controller of the evaporator pocket. Due to the vacuum conditions, a temperature stability better than 0.1 K can easily be achieved and maintained for a long time. Thus, the molecular materials can be thoroughly gassed out at a below-deposition temperature. During deposition, it is convenient to monitor the pressure inside the preparation chamber (blue curve in Figure A.1) as well as the temperature increase (orange curve) of the crucible inside the evaporator. Correlating both curves can give an important hint for the optimum deposition parameters.

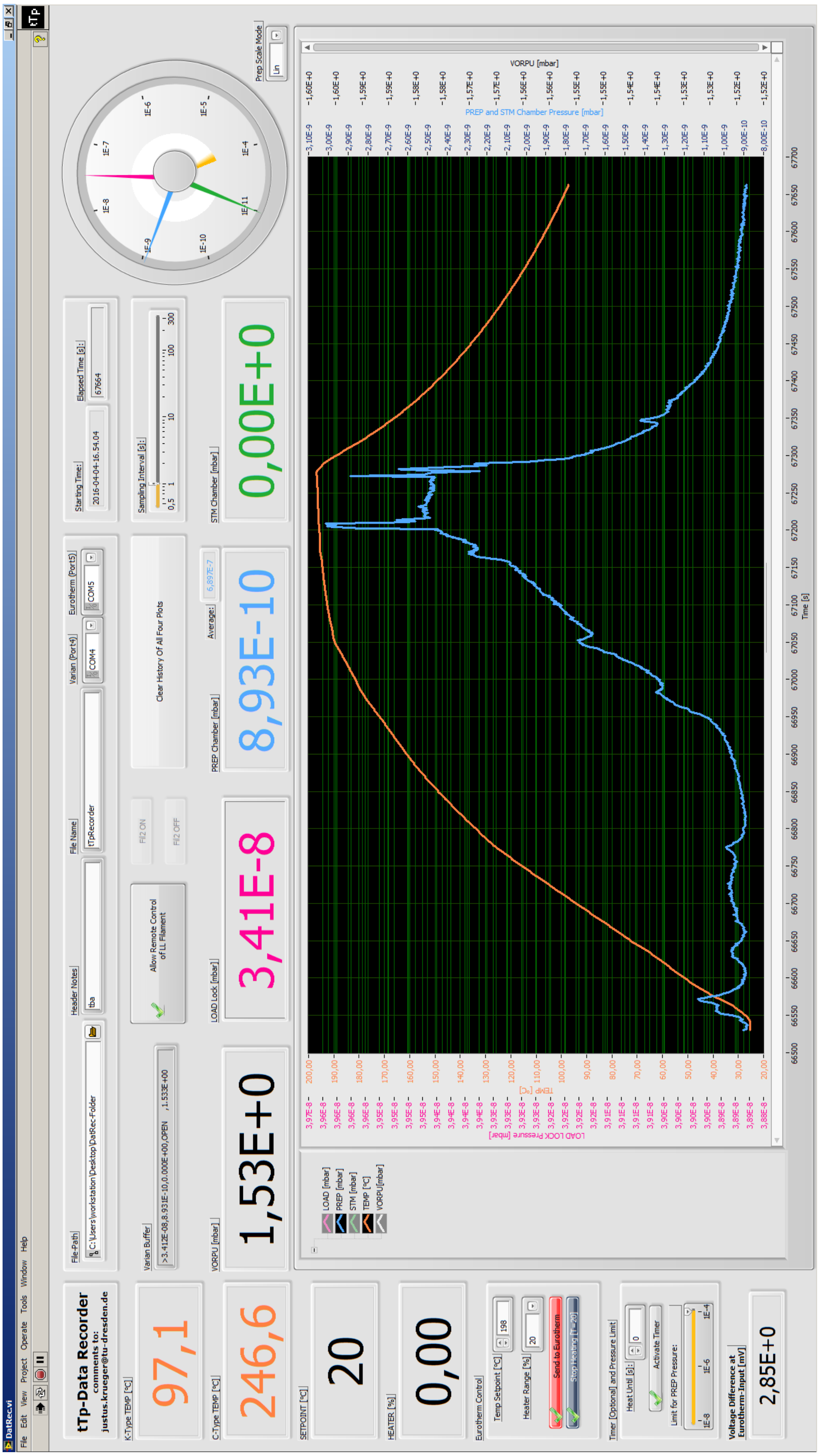
DatRec.vi
File Edit View Project Operate Tools Window Help
tTp
LOAD [mbar]
PREP [mbar]
STM [mbar]
TEMP [°C]
VORPU [mbar]
Prep Scale Mode
Lin
1E-11
1E-10
1E-9
1E-8
1E-7
1E-6
1E-5
1E-4
Allow Remote Control of LL Filament
Fil2 ON
Fil2 OFF
Clear History Of All Four Plots
VORPU [mbar]
PREP and STM Chamber Pressure [mbar]
LOAD LOCK Pressure [mbar]
TEMP [°C]
Time [s]
66500
66550
66600
66650
66700
66750
66800
66850
66900
66950
67000
67050
67100
67150
67200
67250
67300
67350
67400
67450
67500
67550
67600
67650
67700
200,00
190,00
180,00
170,00
160,00
150,00
140,00
130,00
120,00
110,00
100,00
90,00
80,00
70,00
60,00
50,00
40,00
30,00
20,00

**tTp-Data Recorder**
comments to:
justus.krueger@tu-dresden.de

K-Type TEMP [°C]: 97,1

C-Type TEMP [°C]: 246,6

SETPOINT [°C]: 20

HEATER [%]: 0,00

Eurotherm Control
Temp Setpoint [°C]: 198
Heater Range [%]: 20
Send to Eurotherm

Timer (Optional) and Pressure Limit
Heat Until [s]: 0
Activate Timer
Limit for PREP Pressure:

Voltage Difference at Eurotherm-Input [mV]: 2,85E+0

File-Path: C:\Users\workstation\Desktop\DatRec-Folder

Header Notes: tba

File Name: tTpRecorder

Varian (Port4): COM4

Eurotherm (Port5): COM5

Starting Time: 2016-04-04-16.54.04

Elapsed Time [s]: 67664

Sampling Interval [s]: 0,5 1 10 100 300

Varian Buffer: >3,412E-08,8,931E-10,0,000E+00,OPEN ,1,533E+00

VORPU [mbar]: 1,53E+0

LOAD Lock [mbar]: 3,41E-8

PREP Chamber [mbar]: 8,93E-10

Average: 6,897E-7

STM Chamber [mbar]: 0,00E+0

A. 1 – Graphical user interface of the tTp recorder.

## A.2 Additional AFM data of the tetracene precursors

Figure A.2 shows unfiltered AFM measurements with a CO-terminated tip for the two precursors on both possible adsorption sites. Due to the strong non-planar adsorption geometry, it is difficult to identify atomic features in the raw data.

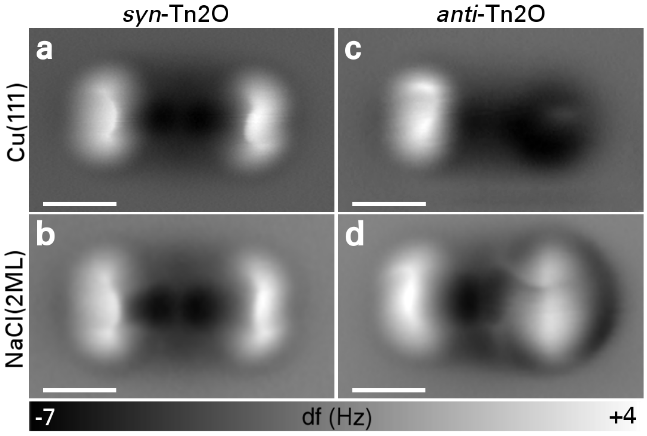

**A. 2 – Raw AFM frequency shift data of *syn/anti*-Tn2O on Cu(111) and NaCl(2ML), respectively.** All scale bars refer to 5 Å. Measurements were acquired in constant-height modus at $V$ = 0 V with a positive offset $\Delta z$ corresponding to a distance decrease with respect to an STM set-point current of $I$ = 2 pA at $V$ = 0.1 V above the clean Cu(111) and NaCl(2ML) surfaces, respectively. **(a)**: *syn*-Tn2O on Cu(111) with $\Delta z$ = +0.4 Å **(b)**: *syn*-Tn2O on NaCl(2ML) with $\Delta z$ = -2.4 Å **(c)**: *anti*-Tn2O on Cu(111) with $\Delta z$ = -0.3 Å **(d)**: *anti*-Tn2O on NaCl(2ML) with $\Delta z$ = -1.6 Å.

## A.3 Control experiment with genuine tetracene

### A.3.1 As-prepared on Au(111)

As a control experiment, genuine tetracene was deposited on the Au(111) surface kept at room temperature. Due to the fact that it belongs to the short acenes, tetracene is stable enough to be directly deposited from a crucible via heating it to 390 K. Figure A.3 shows that the self-assembly for genuine tetracene does not favor any trimeric or dimeric patterns and tend to form densely-packed assemblies if the coverage is high enough. Thus, the surfae looks completely different than the patterns observed for the on-surface generated tetracene. This is a strong indicator that the process of on-surface deoxygenation is crucial for the observed networks.

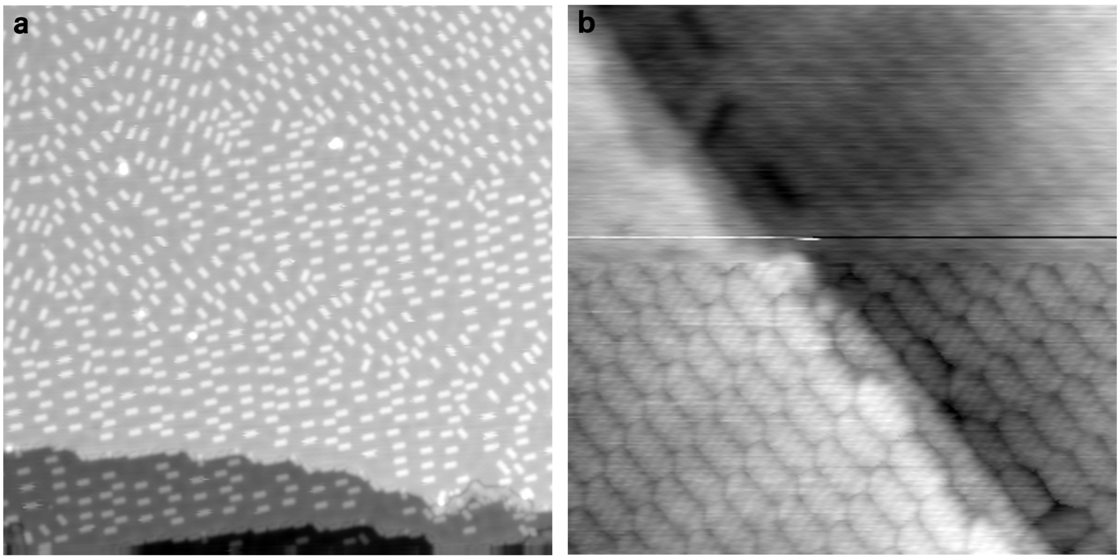

**A. 3 – STM images of genuine tetracene on Au(111). (a):** Preparation with sub-monolayer coverage. *V* = 0.1 V and *I* = 30 pA. Image size: 70 nm x 70 nm. **(b):** Preparation with monolayer coverage. *V* = 1.5 V and *I* = 70 pA. Image size: 12 nm x 12 nm. An accidentally functionalized tip allows one to resolve sub-molecular features in the densely-packed assembly.

### A.3.2 Annealing experiment

Figure A.4 shows the surface after annealing a tetracene-covered sample at 390 K. It is apparent that the ordering is similar to the one observed before annealing.

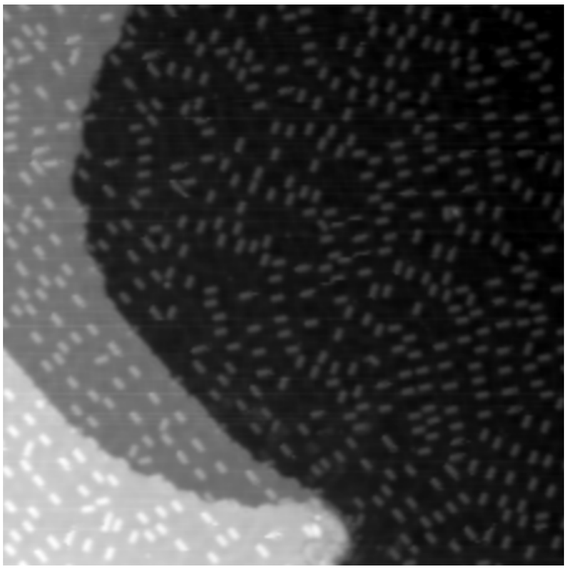

**A. 4 – STM images of genuine tetracene on Au(111) after annealing.** Preparation shown in Figure A.3a was annealed at 390 K. Image size: 70 nm x 70 nm.

## A.4 Additional data for the electronic structure of adsorbed hexacene

The obtained differential conductance images of hexacene at resonant bias values show clear features of the gas-phase orbital densities. This observation is particularly clear for the HOMO resonance; however, also the HOMO-1, LUMO, and LUMO+1 resonances show similarities qualitatively if compared with their respective gas-phase orbital densities. For instance, by comparing with DFT-based calculations shown in the supporting information of [20]. Nevertheless, if adsorbed hexacene is probed with the tip of the STM, affinity/ionization levels are accessed, and a two-dimensional image is mapped. Thus, the sophisticated ESQC-approach is needed to simulate the resonant maps.

By calculating the transmission function spectrum with the tip at one particular position over the molecule, the molecular eigenstates can be identified as sharp peaks in the spectrum as shown in Figure A.5. Subsequently, the differential conductance map of the molecule can be simulated at the identified resonant bias values. In the case of the HOMO-2 resonance, the ESQC-map (Figure A.5) did not match with the experimental image. Instead, a superposition of several molecule eigenstates were necessary to reproduce the experimental image.

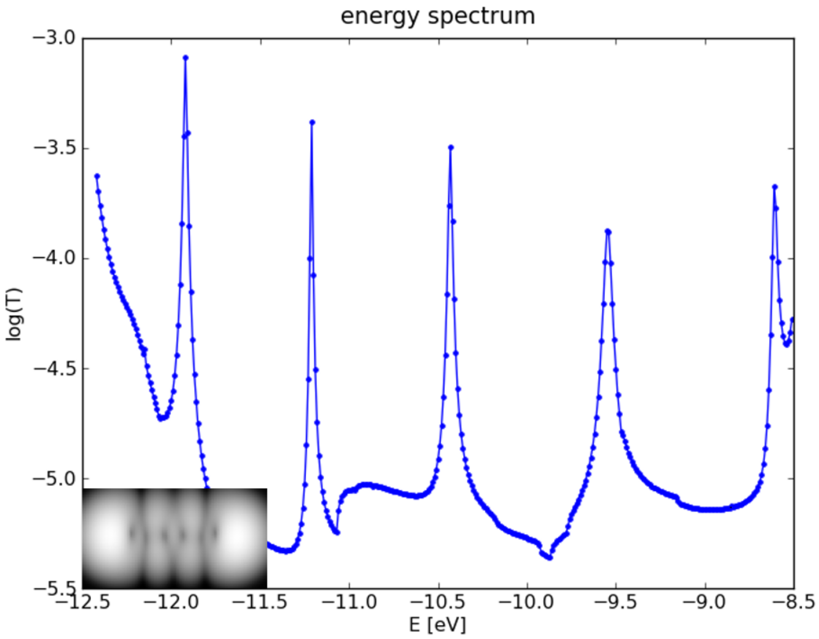

**A. 5 – Computed transmission function of hexacene adsorbed on Au(111) using ESQC.** Hexacene adsorbed on the surface bridges the vacuum gap between tip and sample. Several sharp peaks of the transmission function are visible in this range of the spectrum and indicate resonance with the molecular eigenstates. The inset shows the simulated pure HOMO-2 map. The calculation were performed by T. Lehmann.

## A.5 Additional STM data for Br-substituted precursors

Large-scale STM images (see Figure A.6) failed to show promising long-range and linear structures after thermally induced experiments. The features which are observed on the surface can mainly be attributed to self-assembled clusters of molecules. Due to the densely-packed ordering, it was difficult to disentangle their true nature. However, detailed imaging of isolated but larger adsorbates showed that some of the heptacene molecules are fused in a kinked way as shown in Figure A.7.

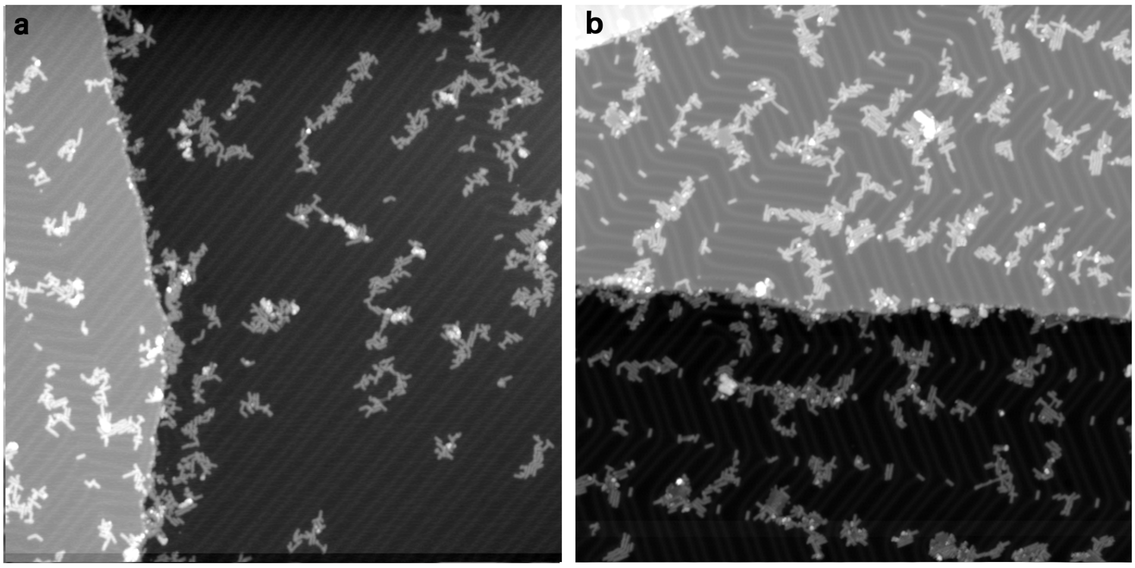

**A. 6 – Large-scale scans of two different Hp4Br3O preparations on Au(111).** **(a):** After annealing at 530 K. **(b):** After depositing on the clean surface kept at 470 K. Images acquired at $V = 0.5\,\text{V}$ and $I = 30\,\text{pA}$. Size: 150 nm x 150 nm.

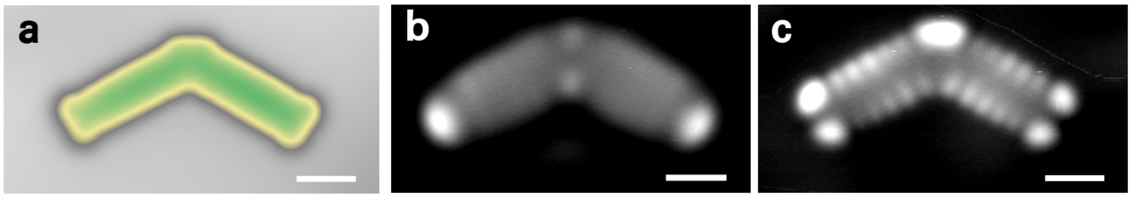

**A. 7 – Two heptacene molecules fused by a single carbon-carbon bond.** One example of a covalent structure found after deposition on the warm surface. **(a):** STM image acquired at $V = -1.4\,\text{V}$ and $I = 0.1\,\text{nA}$. **(b):** Differential conductance map of the LUMO resonances at $V = 1.1\,\text{V}$. **(c):** Differential conductance map of the HOMO resonances at $V = -0.55\,\text{V}$. All scale bars refer to 1 nm.

## A.6 Additional STS data for adsorbed heptacene

Similar to the case of hexacene, probing the higher-orders resonance of heptacene on Au(111) was difficult. First, the HOMO-2 resonance tends to be just a shoulder in differential conductance spectra as indicated by Figure 8. Second, the resonance value of the LUMO+2 is beyond 3 V. At this value, the non-destructive imaging is difficult. Nevertheless, Figure 9 shows the obtained higher-order resonances, as well as the HOMO resonance of the same molecule.

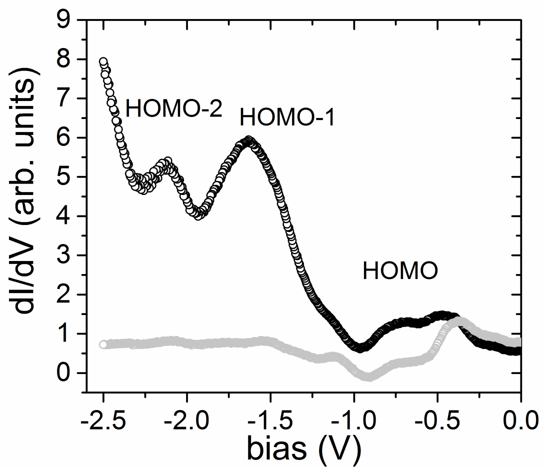

**A. 8 – Extended tunneling spectra of a single heptacene.** The black curve showing three resonances was acquired for a single heptacene molecule while the gray curve shows the metallic background. Due to the relatively large tip-sample separation, the HOMO was not resolved as individual peak but as broad resonance.

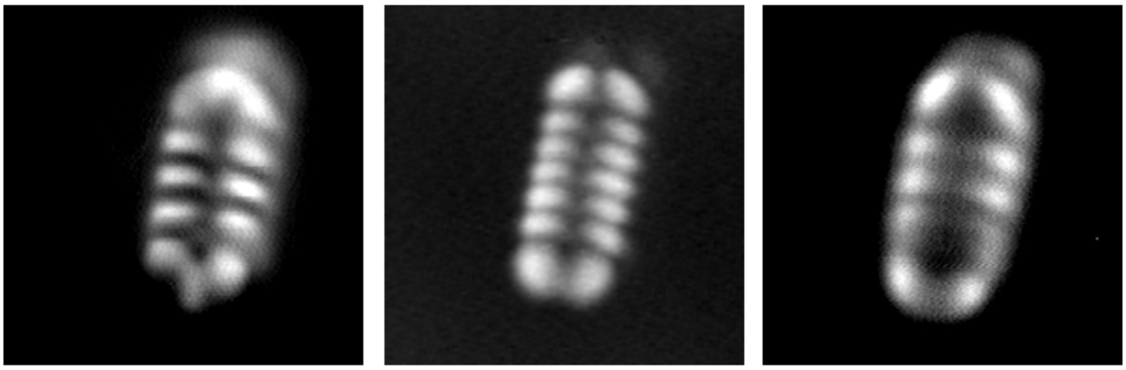

**A. 9 – Higher order resonances of heptacene.** Constant-current maps ($I$ = 0.1 nA) of the differential conductance for an isolated heptacene showing a HOMO-2 (left image, −2.15 V) and LUMO+2 (right, 3.1 V) resonance for spectroscopic measurements. The central image shows the map acquired at the HOMO resonance. Features from a slight double tip are apparent in all three images. Image sizes are 5 nm x 5 nm.

# Bibliography

[1] C. Wang, H. Dong, W. Hu, Y. Liu, D. Zhu, *Chem. Rev.* **2012**, *112*, 2208–2267.

[2] M. Bendikov, H. M. Duong, K. Starkey, K. N. Houk, E. A. Carter, F. Wudl, *J. Am. Chem. Soc.* **2004**, *126*, 7416–7417.

[3] J. E. Anthony, *Angew. Chem. Int. Ed.* **2008**, *47*, 452–483.

[4] S. S. Zade, M. Bendikov, *J. Phys. Org. Chem.* **2012**, *25*, 452–461.

[5] E. Clar, *Ber. dtsch. Chem. Ges. A/B* **1939**, *72*, 1817–1821.

[6] E. Clar, *Ber. dtsch. Chem. Ges. A/B* **1942**, *75*, 1330–1338.

[7] N. Pavliček, A. Mistry, Z. Majzik, N. Moll, G. Meyer, D. J. Fox, L. Gross, *Nat. Nanotechnol.* **2017**, *12*, 308–311.

[8] S. Kivelson, O. L. Chapman, *Phys. Rev. B* **1983**, *28*, 7236–7243.

[9] R. Korytár, D. Xenioti, P. Schmitteckert, M. Alouani, F. Evers, *Nat. Commun.* **2014**, *5*, 5000.

[10] M. Bendikov, F. Wudl, D. F. Perepichka, *Chem. Rev.* **2004**, *104*, 4891–4946.

[11] Q. Ye, C. Chi, *Chem. Mater.* **2014**, *26*, 4046–4056.

[12] N. Koch, *ChemPhysChem.* **2007**, *8*, 1438–1455.

[13] T. Hasegawa, J. Takeya, *Sci. Technol. Adv. Mater.* **2009**, *10*, 024314.

[14] Y. Yamashita, *Sci. Technol. Adv. Mater.* **2009**, *10*, 024313.

[15] A. Maliakal, K. Raghavachari, H. Katz, E. Chandross, T. Siegrist, *Chem. Mater.* **2004**, *16*, 4980–4986.

[16] M. Watanabe, Y. J. Chang, S.-W. Liu, T.-H. Chao, K. Goto, M. M. Islam, C.-H. Yuan, Y.-T. Tao, T. Shinmyozu, T. J. Chow, *Nat. Chem.* **2012**, *4*, 574–578.

[17] R. Mondal, C. Tönshoff, D. Khon, D. C. Neckers, H. F. Bettinger, *J. Am. Chem. Soc.* **2009**, *131*, 14281–14289.

[18] C. Tönshoff, H. F. Bettinger, *Angew. Chem. Int. Ed.* **2010**, *49*, 4125–4128.

[19] M. Hesse, H. Meier, B. Zeeh, *Spectroscopic methods in organic chemistry*, 2nd edition, Thieme, Stuttgart, **2007**.

[20] H. F. Bettinger, C. Tönshoff, M. Doerr, E. Sanchez-Garcia, *J. Chem. Theory. Comput.* **2016**, *12*, 305–312.

[21] G. Franc, A. Gourdon, *Phys. Chem. Chem. Phys.* **2011**, *13*, 14283–14292.

[22] J. Mendez, M. F. Lopez, J. A. Martin-Gago, *Chem. Soc. Rev.* **2011**, *40*, 4578–4590.

[23] R. Lindner, A. Kühnle, *ChemPhysChem.* **2015**, *16*, 1582–1592.

[24] L. Grill, M. Dyer, L. Lafferentz, M. Persson, M. V. Peters, S. Hecht, *Nat. Nanotechnol.* **2007**, *2*, 687–691.

[25] L. Lafferentz, V. Eberhardt, C. Dri, C. Africh, G. Comelli, F. Esch, S. Hecht, L. Grill, *Nat. Chem.* **2012**, *4*, 215–220.

[26] L. Lafferentz, F. Ample, H. Yu, S. Hecht, C. Joachim, L. Grill, *Science* **2009**, *323*, 1193–1197.

[27] H.-Y. Gao, H. Wagner, D. Zhong, J.-H. Franke, A. Studer, H. Fuchs, *Angew. Chem. Int. Ed.* **2013**, *52*, 4024–4028.

[28] C. Nacci, F. Ample, D. Bleger, S. Hecht, C. Joachim, L. Grill, *Nat. Commun.* **2015**, *6*, 7397.

[29] L. Talirz, P. Ruffieux, R. Fasel, *Adv. Mater.* **2016**, *28*, 6222–6231.

[30] J. Cai, P. Ruffieux, R. Jaafar, M. Bieri, T. Braun, S. Blankenburg, M. Muoth, A. P. Seitsonen, M. Saleh, X. Feng, K. Müllen, R. Fasel, *Nature* **2010**, *466*, 470–473.

[31] Y.-C. Chen, T. Cao, C. Chen, Z. Pedramrazi, D. Haberer, D. G. de Oteyza, F. R. Fischer, S. G. Louie, M. F. Crommie, *Nat. Nanotechnol.* **2015**, *10*, 156–160.

[32] P. Ruffieux, S. Wang, B. Yang, C. Sanchez-Sanchez, J. Liu, T. Dienel, L. Talirz, P. Shinde, C. A. Pignedoli, D. Passerone, T. Dumslaff, X. Feng, K. Müllen, R. Fasel, *Nature* **2016**, *531*, 489–492.

[33] M. Treier, C. A. Pignedoli, T. Laino, R. Rieger, K. Müllen, D. Passerone, R. Fasel, *Nat. Chem.* **2011**, *3*, 61–67.

[34] C. Rogers, C. Chen, Z. Pedramrazi, A. A. Omrani, H.-Z. Tsai, H. S. Jung, S. Lin, M. F. Crommie, F. R. Fischer, *Angew. Chem. Int. Ed.* **2015**, *54*, 15143–15146.

[35] L. Gross, F. Mohn, N. Moll, P. Liljeroth, G. Meyer, *Science* **2009**, *325*, 1110–1114.

[36] D. G. de Oteyza, P. Gorman, Y.-C. Chen, S. Wickenburg, A. Riss, D. J. Mowbray, G. Etkin, Z. Pedramrazi, H.-Z. Tsai, A. Rubio, M. F. Crommie, F. R. Fischer, *Science* **2013**, *340*, 1434–1437.

[37] A. Riss, S. Wickenburg, P. Gorman, L. Z. Tan, H.-Z. Tsai, D. G. de Oteyza, Y.-C. Chen, A. J. Bradley, M. M. Ugeda, G. Etkin, S. G. Louie, F. R. Fischer, M. F. Crommie, *Nano Lett.* **2014**, *14*, 2251–2255.

[38] F. Albrecht, N. Pavliček, C. Herranz-Lancho, M. Ruben, J. Repp, *J. Am. Chem. Soc.* **2015**, *137*, 7424–7428.

[39] F. Mohn, J. Repp, L. Gross, G. Meyer, M. S. Dyer, M. Persson, *Phys. Rev. Lett.* **2010**, *105*, 266102.

[40] N. Pavliček, B. Schuler, S. Collazos, N. Moll, D. Pérez, E. Guitián, G. Meyer, D. Peña, L. Gross, *Nat. Chem.* **2015**, *7*, 623–628.

[41] B. Schuler, S. Fatayer, F. Mohn, N. Moll, N. Pavliček, G. Meyer, D. Peña, L. Gross, *Nat. Chem.* **2016**, *8*, 220–224.

[42] L. Gross, F. Mohn, N. Moll, G. Meyer, R. Ebel, W. M. Abdel-Mageed, M. Jaspars, *Nat. Chem.* **2010**, *2*, 821–825.

[43] B. Schuler, G. Meyer, D. Peña, O. C. Mullins, L. Gross, *J. Am. Chem. Soc.* **2015**, *137*, 9870–9876.

[44] B. Schuler, S. Collazos, L. Gross, G. Meyer, D. Pérez, E. Guitián, D. Peña, *Angew. Chem. Int. Ed.* **2014**, *53*, 9004–9006.

[45] J. Lagoute, K. Kanisawa, S. Fölsch, *Phys. Rev. B* **2004**, *70*, 245415.

[46] J. Repp, G. Meyer, S. Paavilainen, F. E. Olsson, M. Persson, *Science* **2006**, *312*, 1196–1199.

[47] T. L. Cocker, D. Peller, P. Yu, J. Repp, R. Huber, *Nature* **2016**, *539*, 263–267.

[48] W. Steurer, S. Fatayer, L. Gross, G. Meyer, *Nat. Commun.* **2015**, *6*, 8353.

[49] J. Repp, G. Meyer, S. M. Stojkovic, A. Gourdon, C. Joachim, *Phys. Rev. Lett.* **2005**, *94*, 026803.

[50] W.-H. Soe, C. Manzano, A. de Sarkar, N. Chandrasekhar, C. Joachim, *Phys. Rev. Lett.* **2009**, *102*, 176102.

[51] L. Gross, N. Moll, F. Mohn, A. Curioni, G. Meyer, F. Hanke, M. Persson, *Phys. Rev. Lett.* **2011**, *107*, 086101.

[52] A. Konishi, T. Kubo in *Physics and Chemistry of Graphene*, (Eds.: T. Enoki, T. Ando), Pan Stanford Publishing, **2013**, pp. 289–351.

[53] A. Aviram, M. A. Ratner, *Chem. Phys. Lett.* **1974**, *29*, 277–283.

[54] C. Joachim, J. K. Gimzewski, A. Aviram, *Nature* **2000**, *408*, 541–548.

[55] W. Han, R. K. Kawakami, M. Gmitra, J. Fabian, *Nat. Nanotechnol.* **2014**, *9*, 794–807.

[56] S. Wang, L. Talirz, C. A. Pignedoli, X. Feng, K. Müllen, R. Fasel, P. Ruffieux, *Nat. Commun.* **2016**, *7*, 11507.

[57] Z. Sun, Q. Ye, C. Chi, J. Wu, *Chem. Soc. Rev.* **2012**, *41*, 7857–7889.

[58] E. Clar, *The Aromatic Sextet*, Wiley, New York, **1972**.

[59] J. Hachmann, J. J. Dorando, M. Aviles, G. K.-L. Chan, *J. Chem. Phys.* **2007**, *127*, 134309.

[60] D. Jiang, S. Dai, *J. Phys. Chem. A* **2008**, *112*, 332–335.

[61] G. Binnig, H. Rohrer, C. Gerber, E. Weibel, *Appl. Phys. Lett.* **1982**, *40*, 178–180.

[62] G. Binnig, H. Rohrer, C. Gerber, E. Weibel, *Phys. Rev. Lett.* **1982**, *49*, 57–61.

[63] G. Binnig, H. Rohrer, C. Gerber, E. Weibel, *Phys. Rev. Lett.* **1983**, *50*, 120–123.

[64] L. D. Landau, E. M. Lifšic, *Quantum mechanics: Non-relativistic theory*, 3rd edition, Butterworth-Heinemann, Oxford, **1981**.

[65] J. Bardeen, *Phys. Rev. Lett.* **1961**, *6*, 57–59.

[66] N. Pavliček, PhD Thesis, Universität Regensburg, **2013**.

[67] R. Wiesendanger, *Scanning probe microscopy and spectroscopy: Methods and applications*, Cambridge Univ. Press, Cambridge, **2001**.

[68] J. Tersoff, D. R. Hamann, *Phys. Rev. Lett.* **1983**, *50*, 1998–2001.

[69] J. Tersoff, D. R. Hamann, *Phys. Rev. B* **1985**, *31*, 805–813.

[70] R. J. Hamers, *Annu. Rev. Phys. Chem.* **1989**, *40*, 531–559.

[71] C. Wagner, R. Franke, T. Fritz, *Phys. Rev. B* **2007**, *75*, 235432.

[72] B. Voigtländer, *Scanning Probe Microscopy*, Springer, Berlin, **2015**.

[73] B. C. Stipe, M. A. Rezaei, W. Ho, *Science* **1998**, *280*, 1732–1735.

[74] B. C. Stipe, M. A. Rezaei, W. Ho, *Phys. Rev. Lett.* **1998**, *81*, 1263–1266.

[75] M. Ternes, PhD Thesis, École polytechnique fédérale de Lausanne, **2006**.

[76] W. Krenner, D. Kühne, F. Klappenberger, J. V. Barth, *Sci. Rep.* **2013**, *3*, 1454.

[77] J.-P. Launay, M. Verdaguer, *Electrons in molecules: From basic principles to molecular electronics*, Oxford University Press, Oxford, **2014**.

[78] A. Köhler, H. Bässler, *Electronic processes in organic semiconductors: An introduction*, Wiley-VCH, Weinheim, **2015**.

[79] M. Portais, M. Hliwa, C. Joachim, *Nanotechnology* **2016**, *27*, 034002.

[80] J.-L. Bredas, *Mater. Horiz.* **2014**, *1*, 17–19.

[81] J. Autschbach, *J. Chem. Educ.* **2012**, *89*, 1032–1040.

[82] E. J. Baerends, O. V. Gritsenko, R. van Meer, *Phys. Chem. Chem. Phys.* **2013**, *15*, 16408–16425.

[83] S. Braun, W. R. Salaneck, M. Fahlman, *Adv. Mater.* **2009**, *21*, 1450–1472.

[84] S. Duhm, A. Gerlach, I. Salzmann, B. Bröker, R. L. Johnson, F. Schreiber, N. Koch, *Org. Electron.* **2008**, *9*, 111–118.

[85] G. Heimel, J.-L. Bredas, *Nat. Nanotechnol.* **2013**, *8*, 230–231.

[86] M. M. Ervasti, F. Schulz, P. Liljeroth, A. Harju, *J. Electron. Spectrosc. Relat. Phenom.* **2017**, 63–71.

[87] J. B. Neaton, M. S. Hybertsen, S. G. Louie, *Phys. Rev. Lett.* **2006**, *97*, 216405.

[88] G. Heimel, S. Duhm, I. Salzmann, A. Gerlach, A. Strozecka, J. Niederhausen, C. Bürker, T. Hosokai, I. Fernandez-Torrente, G. Schulze, S. Winkler, A. Wilke, R. Schlesinger, J. Frisch, B. Bröker, A. Vollmer, B. Detlefs, J. Pflaum, S. Kera, K. J. Franke, N. Ueno, J. I. Pascual, F. Schreiber, N. Koch, *Nat. Chem.* **2013**, *5*, 187–194.

[89] J. D. Jackson, *Classical electrodynamics*, 3rd edition, Wiley, Hoboken, NY, **1998**.

[90] G. Witte, S. Lukas, P. S. Bagus, C. Wöll, *Appl. Phys. Lett.* **2005**, *87*, 263502.

[91] G. Vasseur, Y. Fagot-Revurat, M. Sicot, B. Kierren, L. Moreau, D. Malterre, L. Cardenas, G. Galeotti, J. Lipton-Duffin, F. Rosei, M. Di Giovannantonio, G. Contini, P. Le Fèvre, F. Bertran, L. Liang, V. Meunier, D. F. Perepichka, *Nat. Commun.* **2016**, *7*, 10235.

[92] M. Hollerer, D. Lüftner, P. Hurdax, T. Ules, S. Soubatch, F. S. Tautz, G. Koller, P. Puschnig, M. Sterrer, M. G. Ramsey, *ACS Nano* **2017**, *11*, 6252–6260.

[93] G. Binnig, C. Quate, C. Gerber, *Phys. Rev. Lett.* **1986**, *56*, 930–933.

[94] T. R. Albrecht, P. Grütter, D. Horne, D. Rugar, *J. Appl. Phys.* **1991**, *69*, 668–673.

[95] N. Pavliček, L. Gross, *Nat. Rev. Chem.* **2017**, *1*, 0005.

[96] F. J. Giessibl, *Appl. Phys. Lett.* **2000**, *76*, 1470.

[97] C. J. Chen, *Introduction to Scanning Tunneling Microscopy*, Oxford University Press, **2007**.

[98] L. Gross, F. Mohn, N. Moll, B. Schuler, A. Criado, E. Guitián, D. Peña, A. Gourdon, G. Meyer, *Science* **2012**, *337*, 1326–1329.

[99] F. Schulz, S. Hämäläinen, P. Liljeroth in *Noncontact Atomic Force Microscopy*, (Eds.: S. Morita, F. J. Giessibl, E. Meyer, R. Wiesendanger), NanoScience and technology, Springer International Publishing, Cham, **2015**, pp. 173–194.

[100] D. M. Eigler, C. P. Lutz, W. E. Rudge, *Nature* **1991**, *352*, 600–603.

[101] L. Bartels, G. Meyer, K.-H. Rieder, *Appl. Phys. Lett.* **1997**, *71*, 213–215.

[102] L. Gross, *Nat. Chem.* **2011**, *3*, 273–278.

[103] P. Hapala, G. Kichin, C. Wagner, F. S. Tautz, R. Temirov, P. Jelínek, *Phys. Rev. B* **2014**, *90*, 085421.

[104] C. J. Chen, *Phys. Rev. B* **1990**, *42*, 8841–8857.

[105] R. Temirov, S. Soubatch, O. Neucheva, A. C. Lassise, F. S. Tautz, *New J. Phys.* **2008**, *10*, 053012.

[106] G. Kichin, C. Weiss, C. Wagner, F. S. Tautz, R. Temirov, *J. Am. Chem. Soc.* **2011**, *133*, 16847–16851.

[107] O. Krejčí, P. Hapala, M. Ondráček, P. Jelínek, *Phys. Rev. B* **2017**, *95*, 045407.

[108] R. Temirov, F. S. Tautz in *Noncontact Atomic Force Microscopy*, (Eds.: S. Morita, F. J. Giessibl, E. Meyer, R. Wiesendanger), NanoScience and technology, Springer International Publishing, Cham, **2015**, pp. 275–301.

[109] G. Meyer, *Rev. Sci. Instrum.* **1996**, *67*, 2960.

[110] S. Zöphel, PhD Thesis, Freie Universität Berlin, **2000**.

[111] F. Mohn, PhD Thesis, Universität Regensburg, **2012**.

[112] B. Schuler, PhD Thesis, Universität Regensburg, **2015**.

[113] K. Besocke, *Surf. Sci.* **1987**, *181*, 145–153.

[114] W. Chen, V. Madhavan, T. Jamneala, M. F. Crommie, *Phys. Rev. Lett.* **1998**, *80*, 1469–1472.

[115] J. Sólyom, *Fundamentals of the Physics of Solids (Volume 1): Structure and Dynamics*, Springer, Berlin, **2007**.

[116] F. Hanke, J. Björk, *Phys. Rev. B* **2013**, *87*, 235422.

[117] W. Shockley, *Phys. Rev.* **1939**, *56*, 317–323.

[118] J. Sólyom, *Fundamentals of the Physics of Solids (Volume 2): Electronic Properties*, Springer, Berlin, **2009**.

[119] J. Krüger, N. Pavliček, J. M. Alonso, D. Pérez, E. Guitián, T. Lehmann, G. Cuniberti, A. Gourdon, G. Meyer, L. Gross, F. Moresco, D. Peña, *ACS Nano* **2016**, *10*, 4538–4542.

[120] J. Krüger, F. Eisenhut, J. M. Alonso, T. Lehmann, E. Guitián, D. Pérez, D. Skidin, F. Gamaleja, D. A. Ryndyk, C. Joachim, D. Peña, F. Moresco, G. Cuniberti, *Chem. Commun.* **2017**, *53*, 1583–1586.

[121] T. Hasegawa in *Organic Electronics Materials and Devices*, (Ed.: S. Ogawa), Springer Japan, Tokyo, **2015**, pp. 1–41.

[122] T. Yelin, R. Korytar, N. Sukenik, R. Vardimon, B. Kumar, C. Nuckolls, F. Evers, O. Tal, *Nat. Mater.* **2016**, *15*, 444–449.

[123] Y. Yang, E. R. Davidson, W. Yang, *Proc. Natl. Acad. Sci. USA* **2016**, *113*, E5098–107.

[124] M. Sola, *Front. Chem.* **2013**, *1*, 22.

[125] R. O. Jones, O. Gunnarsson, *Rev. Mod. Phys.* **1989**, *61*, 689–746.

[126] P. Hohenberg, W. Kohn, *Phys. Rev.* **1964**, *136*, B864–B871.

[127] L. Kronik, J. B. Neaton, *Annu. Rev. Phys. Chem.* **2016**, *67*, 587–616.

[128] W. Kohn, L. J. Sham, *Phys. Rev.* **1965**, *140*, A1133–A1138.

[129] J. VandeVondele, M. Krack, F. Mohamed, M. Parrinello, T. Chassaing, J. Hutter, *Comput. Phys. Commun.* **2005**, *167*, 103–128.

[130] J. P. Perdew, K. Burke, M. Ernzerhof, *Phys. Rev. Lett.* **1996**, *77*, 3865–3868.

[131] P. Sautet, C. Joachim, *Phys. Rev. B* **1988**, *38*, 12238–12247.

[132] P. Sautet, C. Joachim, *Chem. Phys. Lett.* **1988**, *153*, 511–516.

[133] P. Sautet, C. Joachim, *Chem. Phys. Lett.* **1991**, *185*, 23–30.

[134] R. Dahlke, PhD Thesis, Ludwig-Maximilians-Universität München, **2004**.

[135] D. Chun, Y. Cheng, F. Wudl, *Angew. Chem. Int. Ed.* **2008**, *47*, 8380–8385.

[136] S. Eda, F. Eguchi, H. Haneda, T. Hamura, *Chem. Commun.* **2015**, *51*, 5963–5966.

[137] M. F. Enamorado, P. W. Ondachi, D. L. Comins, *Org. Lett.* **2010**, *12*, 4513–4515.

[138] D. H. Blank, G. W. Gribble, *Tetrahedron Lett.* **1997**, *38*, 4761–4764.

[139] B. Schuler, M. Persson, S. Paavilainen, N. Pavliček, L. Gross, G. Meyer, J. Repp, *Phys. Rev. B* **2015**, *91*, 235443.

[140] D. M. Eigler, E. K. Schweizer, *Nature* **1990**, *344*, 524–526.

[141] M. F. Crommie, C. P. Lutz, D. M. Eigler, *Science* **1993**, *262*, 218–220.

[142] M. Alemani, M. V. Peters, S. Hecht, K.-H. Rieder, F. Moresco, L. Grill, *J. Am. Chem. Soc.* **2006**, *128*, 14446–14447.

[143] A. Zhao, S. Tan, B. Li, B. Wang, J. Yang, J. G. Hou, *Phys. Chem. Chem. Phys.* **2013**, *15*, 12428–12441.

[144] H. J. Lee, W. Ho, *Science* **1999**, *286*, 1719–1722.

[145] S.-W. Hla, L. Bartels, G. Meyer, K.-H. Rieder, *Phys. Rev. Lett.* **2000**, *85*, 2777–2780.

[146] T. Kumagai, F. Hanke, S. Gawinkowski, J. Sharp, K. Kotsis, J. Waluk, M. Persson, L. Grill, *Nat. Chem.* **2014**, *6*, 41–46.

[147] I. Swart, T. Sonnleitner, J. Niedenführ, J. Repp, *Nano Lett.* **2012**, *12*, 1070–1074.

[148] B. Schuler, W. Liu, A. Tkatchenko, N. Moll, G. Meyer, A. Mistry, D. Fox, L. Gross, *Phys. Rev. Lett.* **2013**, *111*, 106103.

[149] M. Watanabe, K.-Y. Chen, Y. J. Chang, T. J. Chow, *Acc. Chem. Res.* **2013**, *46*, 1606–1615.

[150] R. Dorel, A. M. Echavarren, *Eur. J. Org. Chem.* **2017**, *2017*, 14–24.

[151] J. Krüger, F. Eisenhut, T. Lehmann, J. M. Alonso, J. Meyer, D. Skidin, R. Ohmann, D. A. Ryndyk, D. Pérez, E. Guitián, D. Peña, F. Moresco, G. Cuniberti, *J. Phys. Chem. C* **2017**, *121*, 20353–20358.

[152] A. Gourdon, *On-Surface Synthesis*, Springer International Publishing, Cham, **2016**.

[153] J. V. Barth, *Annu. Rev. Phys. Chem.* **2007**, *58*, 375–407.

[154] L. Gross, F. Moresco, P. Ruffieux, A. Gourdon, C. Joachim, K.-H. Rieder, *Phys. Rev. B* **2005**, *71*, 165428.

[155] S. Klyatskaya, F. Klappenberger, U. Schlickum, D. Kühne, M. Marschall, J. Reichert, R. Decker, W. Krenner, G. Zoppellaro, H. Brune, J. V. Barth, M. Ruben, *Adv. Funct. Mater.* **2011**, *21*, 1230–1240.

[156] L. Bartels, *Nat. Chem.* **2010**, *2*, 87–95.

[157] G. Pawin, K. L. Wong, K.-Y. Kwon, L. Bartels, *Science* **2006**, *313*, 961–962.

[158] W. Chen, H. Li, H. Huang, Y. Fu, H. L. Zhang, J. Ma, A. T. S. Wee, *J. Am. Chem. Soc.* **2008**, *130*, 12285–12289.

[159] C. Weiss, C. Wagner, R. Temirov, F. S. Tautz, *J. Am. Chem. Soc.* **2010**, *132*, 11864–11865.

[160] A. M. Sweetman, S. P. Jarvis, H. Sang, I. Lekkas, P. Rahe, Y. Wang, J. Wang, N. R. Champness, L. Kantorovich, P. Moriarty, *Nat. Commun.* **2014**, *5*, 3931.

[161] S. Soubatch, I. Kröger, C. Kumpf, F. S. Tautz, *Phys. Rev. B* **2011**, *84*, 195440.

[162] U. Schlickum, R. Decker, F. Klappenberger, G. Zoppellaro, S. Klyatskaya, W. Auwärter, S. Neppl, K. Kern, H. Brune, M. Ruben, J. V. Barth, *J. Am. Chem. Soc.* **2008**, *130*, 11778–11782.

[163] F. Klappenberger, D. Kühne, W. Krenner, I. Silanes, A. Arnau, Garcia de Abajo, F Javier, S. Klyatskaya, M. Ruben, J. V. Barth, *Nano Lett.* **2009**, *9*, 3509–3514.

[164] X. Deng, B. K. Min, A. Guloy, C. M. Friend, *J. Am. Chem. Soc.* **2005**, *127*, 9267–9270.

[165] A. E. Baber, D. Torres, K. Müller, M. Nazzarro, P. Liu, D. E. Starr, D. J. Stacchiola, *J. Phys. Chem. C* **2012**, *116*, 18292–18299.

[166] M. Böhringer, W.-D. Schneider, R. Berndt, *Surf. Sci.* **1998**, *408*, 72–85.

[167] C. B. France, P. G. Schroeder, J. C. Forsythe, B. A. Parkinson, *Langmuir* **2003**, *19*, 1274–1281.

[168] J. A. Smerdon, M. Bode, N. P. Guisinger, J. R. Guest, *Phys. Rev. B* **2011**, *84*, 165436.

[169] W. J. Bailey, C.-W. Liao, *J. Am. Chem. Soc.* **1955**, *77*, 992–993.

[170] R. B. Campbell, J. M. Robertson, J. Trotter, *Acta Cryst.* **1962**, *15*, 289–290.

[171] H. Angliker, E. Rommel, J. Wirz, *Chem. Phys. Lett.* **1982**, *87*, 208–212.

[172] R. Mondal, R. M. Adhikari, B. K. Shah, D. C. Neckers, *Org. Lett.* **2007**, *9*, 2505–2508.

[173] H. Söde, L. Talirz, O. Gröning, C. A. Pignedoli, R. Berger, X. Feng, K. Müllen, R. Fasel, P. Ruffieux, *Phys. Rev. B* **2015**, *91*, 045429.

[174] J. van der Lit, M. P. Boneschanscher, D. Vanmaekelbergh, M. Ijas, A. Uppstu, M. Ervasti, A. Harju, P. Liljeroth, I. Swart, *Nat. Commun.* **2013**, *4*, 2023.

[175] S. J. Blanksby, G. B. Ellison, *Acc. Chem. Res.* **2003**, *36*, 255–263.

[176] M. Koch, F. Ample, C. Joachim, L. Grill, *Nat. Nanotechnol.* **2012**, *7*, 713–717.

[177] R. Mondal, B. K. Shah, D. C. Neckers, *J. Am. Chem. Soc.* **2006**, *128*, 9612–9613.

[178] R. Einholz, T. Fang, R. Berger, P. Gruninger, A. Früh, T. Chasse, R. F. Fink, H. F. Bettinger, *J. Am. Chem. Soc.* **2017**, *139*, 4435–4442.

[179] T. Okamoto, M. L. Senatore, M.-M. Ling, A. B. Mallik, M. L. Tang, Z. Bao, *Adv. Mater.* **2007**, *19*, 3381–3384.

[180] R. Zuzak, R. Dorel, M. Krawiec, B. Such, M. Kolmer, M. Szymonski, A. M. Echavarren, S. Godlewski, *ACS Nano* **2017**, *11*, 9321–9329.

[181] J. Krüger, F. García, F. Eisenhut, D. Skidin, J. M. Alonso, E. Guitián, D. Pérez, G. Cuniberti, F. Moresco, D. Peña, *Angew. Chem. Int. Ed.* **2017**, *56*, 11945–11948.

# Scientific contributions

## Articles

[A1] J. Krüger, N. Pavliček, J. M. Alonso, D. Pérez, E. Guitián, T. Lehmann, G. Cuniberti, A. Gourdon, G. Meyer, L. Gross, F. Moresco, D. Peña, *ACS Nano* **2016**, *10*, 4538-4542.

[A2] J. Krüger, F. Eisenhut, J. M. Alonso, T. Lehmann, E. Guitián, D. Pérez, D. Skidin, F. Gamaleja, D. A. Ryndyk, C. Joachim, D. Peña, F. Moresco, G. Cuniberti, *Chem. Commun.* **2017**, *53*, 1583-1586.

[A3] J. Krüger, F. Eisenhut, T. Lehmann, J. M. Alonso, J. Meyer, D. Skidin, R. Ohmann, D. A. Ryndyk, D. Pérez, E. Guitián, D. Peña, F. Moresco, G. Cuniberti, *J. Phys. Chem. C* **2017**, *121*, 20353-20358.

[A4] J. Krüger, F. García, F. Eisenhut, D. Skidin, J. M. Alonso, E. Guitián, D. Pérez, G. Cuniberti, F. Moresco, D. Peña, *Angew. Chem. Int. Ed.* **2017**, *129*, 11945-11948.

## Talks

[T1] *STM study of molecular n-dopants for organic electronics*,
given at the DPG Frühjahrstagung,
Berlin, Germany (March 2015).

[T2] *Exploring the Diels-Alder reaction on Au(111)*,
given at the fourth consortium meeting of the European project PAMS,
Zurich, Switzerland (April 2015).

[T3] *Tetracene formation by on-surface reduction*,
given at the DPG Frühjahrstagung,
Regensburg, Germany (March 2016).

[T4] *Imaging the electronic structure of on-surface generated hexacene*,
given at the sixth consortium meeting of the European project PAMS,
Mainz, Germany (May 2016).

[T5] *Acene formation by on-surface reduction*,
given at the international workshop "On-surface synthesis",
San Sebastián, Spain (June 2016).

[T6] *Electronic resonances of large acenes generated on-surface*,
given at the seventh consortium meeting of the European project PAMS,
Brussels, Belgium (Nov. 2016).

[T7] *Imaging the electronic structure of long acenes generated on-surface*,
given at the European Conference on Molecular Electronics,
Dresden, Germany (Aug. 2017).

## Posters

[P1] *On-surface fabrication of acenes*,
presented at the 598. Wilhelm und Else Heraeus-Seminar
on “Frontiers in Scanning Probe Microscopy”,
Bad Honnef, Germany (Nov. 2015).

[P2] *Imaging the electronic structure of long acenes generated on-surface*,
presented at the international conference "Trends in nanotechnology",
Dresden, Germany (June 2017).

# Acknowledgment

Many people played a vital part in my work of the last three and a half years, and I would like to acknowledge all their support I received during that time. First of all, I would like to thank Prof. Gianaurelio Cuniberti for giving me the opportunity to be part of the Chair of Materials Science and Nanotechnology and providing a highly stimulating and fruitful research environment. Second, I am grateful that Prof. Lukas Eng showed so much interest in my work and was willing to be the second referee of this thesis.

I thank my supervisor Dr. Francesca Moresco for imparting all her knowledge and passion about surface science, and for being incredibly supportive and encouraging throughout the whole time. A significant debt of gratitude goes to the CiQUS team in Santiago de Compostela who provided the idea and exceptional expertise for the synthesis of the acene precursors. Moreover, I would like to thank Prof. Diego Peña for his endless enthusiasm for new experimental results and his helpful comments on surprising observations. In this regard, Dr. André Gourdon should also be mentioned who gave constantly valuable input on this work and coordinated the PAMS project.

It was my pleasure to work with and learn from Jörg Meyer, Anja Nickel and Dr. Robin Ohmann during the first part of my doctoral studies. All three of them introduced me to different aspects of the lab work and made my transition into this field so much easier. Furthermore, I would like to thank Frank Eisenhut and Dmitry Skidin for making the shared time in the lab enjoyable. It was always a pleasure to tackle the different leak, noise, and transfer challenges together. This team was boosted by Florian Gamaleja for some time, and I enjoyed the scientific and non-scientific discussion with all three of you. Also, it was always a joy to be around the other members of our chair and to get insights into completely unfamiliar areas of research during lunch breaks.

I am very grateful for the fruitful collaboration with Thomas Lehmann and Dr. Dmitry A. Ryndyk which allowed a much deeper insight into the obtained experimental results based on their modeling. Here, I would also like to mention Dr. Christian Joachim who shared his thorough understanding of atomic-scale physics with us and his fas-

cinating visions were a true source of inspiration to me. My research stay at IBM Research—Zurich was a unique experience, and I would like to thank Dr. Gerhard Meyer and Dr. Leo Gross for inviting me into their group and showing great trust to let me work at one of their microscopes. I am grateful for the excellent supervision of Dr. Niko Pavliček who introduced me to the subtleties of high-resolution imaging. Getting to play basketball together in the afternoons with Shadi Fatayer was the icing on the cake of my Rüschlikon experience.

Finally, I would like to thank all the people close to my heart for their endless support and encouragement and motivation.

# Statement of authorship

Folgende Erklärung gebe ich hiermit ab:

(1) Ich versichere, dass ich die vorliegende Arbeit ohne unzulässige Hilfe Dritter und ohne Benutzung anderer als der angegebenen Hilfsmittel angefertigt habe; die aus fremden Quellen direkt oder indirekt übernommenen Gedanken sind als solche kenntlich gemacht.

(2) Bei der Auswahl und Auswertung des Materials sowie bei der Herstellung des Manuskripts habe ich Unterstützung von folgenden Personen erhalten:

   a) Prof. G. Cuniberti
   b) Dr. F. Moresco
   c) Prof. D. Peña
   d) Dr. N. Pavliček (Kapitel 4)
   e) Dr. L. Gross (Kapitel 4)
   f) T. Lehmann

   Weitere Personen waren an der geistigen Herstellung der vorliegenden Arbeit nicht beteiligt. Insbesondere habe ich nicht die Hilfe eines kommerziellen Promotionsberaters in Anspruch genommen. Dritte haben von mir keine geldwerten Leistungen für Arbeiten erhalten, die in Zusammenhang mit dem Inhalt der vorgelegten Dissertation stehen.

(3) Die Arbeit wurde bisher weder im Inland noch im Ausland in gleicher oder ähnlicher Form einer anderen Prüfungsbehörde vorgelegt und ist auch noch nicht veröffentlicht worden.

(4) Die Promotionsordnung der Fakultät Maschinenwesen an der TU Dresden vom 01.07.2001 wird anerkannt.